Simulation of the Powder Forging Process for Titanium Components using a Porous Metal Plasticity Model

A thesis

submitted in fulfilment

of the requirements for the degree

of

Doctor of Philosophy

at

The University of Waikato

by

NAVANEETH VELLUVAKKANDI

THE UNIVERSITY OF
WAIKATO
Te Whare Wānanga o Waikato

2014

ABSTRACT

Powder forging is a technique that has been used to produce fully dense near-net parts from metal powders. Due to a “low cost titanium” product manufacturing initiative, targeting a reduction in the cost of titanium components, a titanium powder forging technique has gained significant interest. In titanium powder forging, powder consolidation is a key factor that influences successful component manufacture. Consolidation during titanium powder forging is dependent on the densification and deformation mechanisms involved.

In this study, a finite element method is used to model the densification and deformation behaviour of titanium powder compacts during powder forging. The research focuses on developing a simulation capability and identifying a suitable constitutive model to simulate the powder forging process that can predict the relative density distribution. The simulation is carried out in Abaqus software and the results are compared with experimental results. A gamma particle radiography technique is used to compare the experimental density results with the simulated results.

The Gurson and Gurson-Tvergaard models are used to predict the relative density of porous titanium powder compacts during upset-powder forging and are used to include the effect of hydrostatic stresses and the extent of densification. Three different modes of densification, related to powder forging were studied i.e. upset forging, hot-repressing and closed die forging.

The simulation results indicate that both models can be used to determine the relative density during powder forging. By comparing the simulated results with the experimental results, it is found that the density prediction given by the Gurson-Tvergaard model showed closer agreement with the calculated parameters.

ACKNOWLEDGEMENT

This thesis would not be complete without acknowledging the individuals involved at the University of Waikato and our proud titanium research group (WaiCam). Firstly, I would like to thank chief supervisor Professor Brian Gabbitas for providing me the encouragement, guidance and valuable resources towards completion of this thesis. I know things have been tough towards the end with your busy schedule towards the ongoing titanium research and development, so thank you for the time away from your work to supervise me on this thesis.

I would also like to take this opportunity to thank my former supervisor Prof. Deliang Zhang for his early contributions and direction towards this research. I am extremely grateful to Stella Raynova, Dr. Fei Yang and Kenneth Sichone for their invaluable advice and guidance throughout my journey from an engineering student to an academic. I have always enjoyed the tea room conversations we had that had enhanced my understanding of powder metallurgy and greatly influenced my way of thinking towards the work presented this thesis. I would also, like to convey my gratitude to all the faculties involved and the students in our research group for their encouragement and support.

Completing this thesis would not have been possible without the understanding and support of my friend Xueyan Wei, who have provided constant encouragement throughout this work. I am eternally obligated to thank you for your patience, humour, and sacrifices you made during of my doctoral study.

Finally, to my parents, Mr. V Vasavan and Mrs. A.B Presanna; the years I have spent away from home are a testament to the sacrifices made by you in the pursuit of my goals. Thank you for your patience and your grace.

TABLE OF CONTENTS

TABLE OF FIGURES

List of Tables

1 Introduction and literature review

The powder forging method was introduced as a manufacturing method in the automotive industry nearly 35 years ago, and ever since it has been a competitive technology for producing light weight parts. Recently, due to the "*low cost titanium*" product manufacturing initiative targeting a reduction in the cost of titanium components, the powder forging technique has gained interest [1]. In powder forging the titanium powders are uniaxially pressed in a closed die to achieve a desired near net shape. After pressing a billet (from here on referred to as the powder compact), it is ejected from the die and later sintered (induction or vacuum furnace) at high temperature to attain diffusion bonding among the compressed particles. The final densification and shape of the powder compact is achieved through powder forging in an open or closed die and this eliminates any residual porosity.

The mechanical properties in forged titanium parts made using a powder route are superior to those found in wrought products. Also, near net shapes requiring minimum machining can be achieved. Through the powder metallurgical routes of blending and alloying, a wide range of titanium metal products can be manufactured through powder forging. Powder forging technology has been successfully proven in the automotive industry [2, 3], and has shown to be desirable for both high and medium volume titanium component production requirements.

In powder forging, the key factors influencing successful component manufacture include a knowledge of materials used, powder consolidation characteristics in both initial powder compaction, sintering and during forging and tooling design. Understanding the powder characteristics and deformation mechanisms in each of the processing steps of die filling, compaction, ejection, sintering and powder forging, influences the overall quality and productivity of titanium parts via powder forging. Achieving high strength and ductility is desirable for powder forged titanium components used in general engineering and in those applications where enhanced performance is required.

The relative density distribution achieved after powder forging is identified as an important factor in determining the overall strength, ductility and fatigue behaviour in

components. An understanding of densification behaviour is therefore crucial. A uniform density distribution promotes uniform mechanical properties throughout the final component making its properties more predictable and reliable. Obtaining uniform density during compaction is also necessary to prevent undesirable distortion during the sintering phase or post compaction treatments such as machining and heat treatments. Achieving full density in powder metallurgical products has often proven to be challenging due to the nature of the starting material, friction and temperature distributions associated with the die and compact. However, uniform densification can be attained by appropriate manipulation of die geometry and temperature control resulting in predictable mechanical properties in a forged component.

In recent decades, there have been significant advances in scientific research to simulate various aspects of powder metallurgical processing. Studies [4-6] to numerically model the powder behaviour during the various stages in PM processing have increased our understanding of the behaviour of the powder during each phase of PM manufacturing. Among the different methods used the finite element analysis method has become a predominant tool for predicting the density distribution during PM processing.

For modelling a powder forging process in order to simulate the response of powder compacts during the powder forging process, a constitutive relationship and a numerical method are required. An ideal constitutive model should be able to predict the stress states, strain rates, displacements and density distribution within a powder compact subjected to external forces. Gurson's model [7] has proven to be suitable for finite element modelling of the densification behaviour of porous materials undergoing large deformation.

The Gurson model predicts the densification, stress states, displacement and frictional effects during a powder forging process. For implementing the Gurson model different material parameters and simulation procedures are required for different powders, die configurations and loading types. Several of these parameters and conditions require numerous and costly experimentation. By successfully implementing a constitutive model, such as the Gurson model, in the early tooling

design phase, industry would be able to take advantage of precise information about the internal structure of a component, material failure characteristics during service life etc. This would help improve the quality of a final product.

1.1 Problem statement

Simulating densification accurately during powder compact forging using finite element method is difficult due to the complexities associated with the implementation of the constitutive models. In 1970, Gurson [8] proposed a continuum theory for ductile failure by void nucleation and void growth using a yielding criterion and flow rule for ductile porous material. Gurson developed an approximate yield criteria and flow rules for porous ductile materials by demonstrating the role of hydrostatic stress in plastic yield and void growth. Gurson' s model has been successfully applied for various powder metal forming processes such as compaction, hot pressing sintering and hot isostatic pressing (HIP).

More recently, researchers [9-11] have suggested several variations to the original Gurson model; however the basic Gurson yield function remains unchanged. Among the different models available for simulating the densification behaviour of porous ductile materials, the Gurson model is accurate, simple and relatively easier to implement. Several researchers have successfully applied the Gurson model to an analysis of consolidation behaviour during powder metallurgical processes [12, 13]. However, there is little available literature which focuses on the fundamentals of the model when applied to the forging of titanium powder compacts with a low initial relative density as involved in powder compact forging.

The Gurson model can be implemented for (both powder compaction and forging); however it must be calibrated for each material and the process under investigation. For this reason, much of the literature focusing on the implementation of this model in powder forging relies on empirical data for the material parameters. Also, to the best of the author's knowledge there are no data available on the material parameters for titanium powder compacts forged at low initial relative density.

1.2 Motivation and benefits

Titanium metal is attractive for aerospace, industrial, marine, automotive, medical and sports applications due to its excellent mechanical properties and corrosion resistance. Despite titanium's favourable properties, its application has been limited compared with steel and aluminium due to its high cost. The high cost of titanium derives from the difficulty in extracting it from its ore and further electrolytic refinement prior to making ingots. The cost gap further widens when fabricating useful components or structures.

The powder compact forging technique provides a favourable alternative for producing near net shapes at reduced cost because of low material wastage. Several researchers [12, 13] have carried out a theoretical analysis backed up by experimental data of the deformation and densification mechanism during powder forging. But very little work has focused on the powder compact forging of titanium alloys with an initially low compact density.

Further, recent research at the University of Waikato has successfully demonstrated the fabrication of titanium components, with acceptable microstructure and mechanical properties, using a powder compact forging technique [14]. For an industrial scaling-up of this technology it would be useful if the manufacturing route could be modelled based on an understanding of the deformation and densification mechanisms during powder compact forging. The aim of this research is to make use of the benefits of FEA techniques in the design of powder compact forging processes, coupled with some advanced material modelling techniques. The focus of this study is to analyse the powder compact forging process using the Gurson and Gurson-Tvergaard models using finite element analysis and experimental studies. Although these two models have been previously used to simulate various powder metallurgical processes, the implications of the Gurson-Tvergaard parameters in titanium powder compact forging have never been precisely studied.

1.3 Titanium and titanium alloys

During the last few decades, titanium has been the metal of choice for many aerospace, marine, medical and other more general industrial applications. Titanium metal is attractive because of its unique features such as lightweight, high strength and good corrosion resistance. In weight titanium is 40 % lighter than steel. The only other materials that are lighter than titanium are aluminium, magnesium and beryllium; however none of these metals have the same mechanical performance as that of titanium. Titanium and titanium alloys operate in highly demanding situations in aerospace and gas turbine applications for both rotating and stationary parts [15]. Despite the increasing applications of titanium in the aerospace industry, more recently there have been several non-aerospace applications such as in chemical processing, nuclear power plants, oil refineries, heat exchangers, medical devices, consumer products etc. [16, 17]. A major drive for titanium in non-aerospace applications is its excellent properties such as, low density, high specific strength, good corrosion resistance, and good bio-compatibility [18, 19].

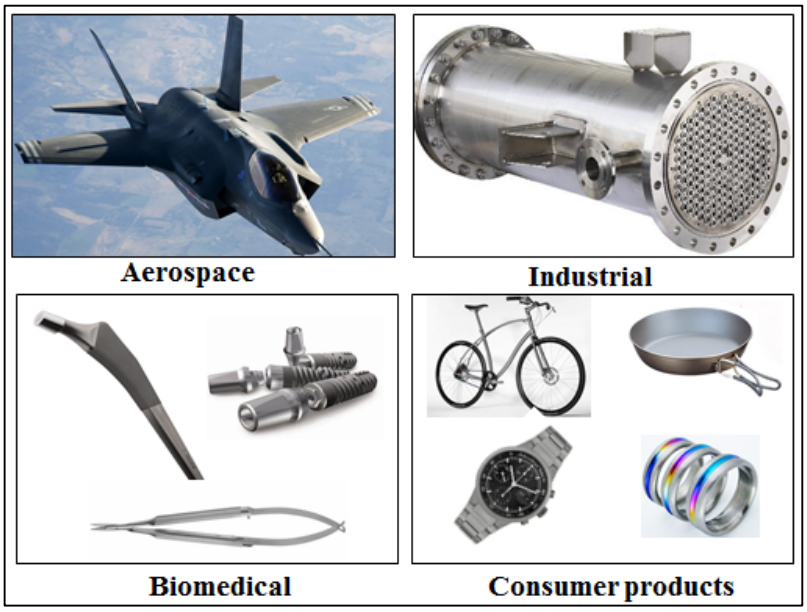

Figure 1.1: Applications of titanium and its alloys

Regardless of its favourable physical and mechanical properties, titanium alloys have yet to make significant advances into mainstream engineering applications, where metals such as steel and aluminium are predominant. The primary reason that limits the more widespread use of titanium is its high cost [20-22]. The high cost is because

titanium production involves elaborate reduction processes, multiple melting steps and secondary processing operations for ingot breakdown and the production of semi-finished products by forging rolling and extrusion. In addition if a part production requires machining the material wastage results in a further increase in production costs. In addition to high processing costs, other technical challenges that are restrictive are titanium's susceptibility to absorb oxygen, nitrogen and hydrogen [22] and machining difficulties. Machining difficulties could be overcome by novel cutting tool coatings and improved machining practices such as laser assisted machining [23]. Secondary manufacturing costs can also be significantly reduced by near-net shape manufacturing. Additionally, titanium's high affinity, at elevated temperatures, to interstitial elements such as oxygen and nitrogen necessitates production being carried out in a controlled environment, which adds cost.

Based on their influence on the beta-transus temperature, the alloying elements of titanium are classified as neutral (Sn, Zr), alpha-stabilisers (Al, Ga, O, N, C) and beta-stabilisers (V, Mo, Nb, Fe, Cr, and Ni). Figure 1.2 shows the influence of alloying elements on the phase diagrams of titanium alloy.

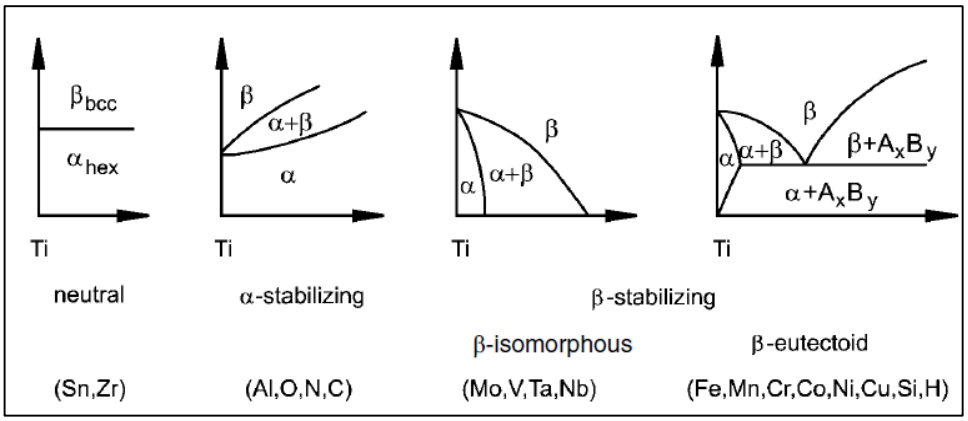

Figure 1.2: Influence of alloying elements on the titanium phase diagrams [24]

The addition of alpha-stabilising elements extends the alpha phase field to higher temperature, whereas beta-stabilising elements shift the beta fields to lower temperatures. The neutral elements have minor influence on the beta-transus temperature. Among the alpha-stabilising elements, aluminium is an important alloying element. It is important to mention that most commercially available titanium alloys belong to this category. Interstitial impurities such as oxygen, nitrogen and

carbon are also considered as alpha-stabilising elements. In addition to extending the alpha phase field to higher temperatures, the alpha-stabilisers develop into a two-phase alpha field as shown in figure 1.2 [24]. The alpha-stabilising elements are further subdivided into two categories; i.e. beta-isomorphous and beta-eutectic elements. Among beta-isomorphous alloying elements, Mo, V, and Ta, are considered important because of their higher solubility in titanium. Furthermore, even very low volume fractions of beta-eutectic such as Fe, Mn, Cr, Co, Ni, Cu, Si, and H can lead to formation of intermetallic compounds. The neutral elements Sn and Zr have no influence on the alpha or beta field boundaries.

Depending on the phase present in the microstructure and alloy addition titanium alloys are classified as;

1.3.1 (Alpha) α-Alloys

α-Alloys are single phase alloys that are solid solution strengthened by addition of α stabilisers. α-Alloys are typically stable and exhibit good high temperature properties, but the properties cannot be improved by heat treatment at microscopic level [16]. Oxygen as an alloying element in α-titanium is an alpha stabilizer, and oxygen is an effective strengthening element in titanium alloys at low temperatures. In commercially pure titanium oxygen is present in a weight percentage of 0.12 to 0.16 %. If the content of oxygen is too low, the strength can be low and the beta transformation temperature will be low. On the other side, if the oxygen content is too high, durability and damage tolerance properties can be reduced. Depending on the level of impurities, titanium alloys can be classified as extra low interstitial (ELI) titanium and ultrapure titanium. Ti-8Al-1Mo-1V and Ti-2.5Cu are other common examples of α-titanium alloys.

1.3.2 Near α-Alloys

The strength and workability of these alloys have been enhanced by small additions of β stabilising elements (Mo and V). Near α-titanium alloys have found many applications with their favourable integrated properties [16]. Near α–alloys are an excellent choice for applications that demand high strength and creep resistance. The

most widely used titanium alloys in high temperature aero-engine applications belong to this class. Ti-6Al-2Zr-1Mo-1V and Ti-6Al-2Sn-4Zr-2Mo are the best examples for this class of alloy.

1.3.3 α +β Alloys

These alloys contain both alpha and beta stabilisers. The presence of alpha stabilisers improves the strength while beta stabilisers allow the beta phase to be retained after quenching. The α +β alloys can be heat treated to develop a variety of microstructures and mechanical property combinations. A primary example of this type of alloy is Ti-6Al-4V which makes up more than half the sales of titanium alloys.

1.3.4 Metastable β alloys

Metastable β alloys contain a higher percentage (10 to 15 %) of beta stabilising elements compared to both α and α +β alloys. In these alloys the β phase is maintained at room temperature in a metastable condition, enabling it to be forged at a wide range of temperatures. These alloys have high strength, toughness, excellent hardenability and workability. These alloys along with β alloys are an excellent alternative where high strength and fracture toughness is required. These alloys are increasingly finding applications in aircraft structures and cutting edge surgical instruments due to their ability to be hardened and cold worked at relatively low temperatures. An example of class of alloy is the Ti-15V-3Sn-3Cr-3Al alloy [24].

1.3.5 Thermo-mechanical processing (TMP) of titanium and its alloys

Like many prominent engineering alloys, titanium alloys can also be forged into any desired shape based on the design criteria for the final product. However, titanium and its alloys are among the most difficult materials to forge and are ranked behind that of high performance nickel alloys and some refractory metals. For α+β titanium alloys the microstructure, when forging within the α+β two phase region, is influenced by the amount of plastic strain occurring during deformation [25]. When forging titanium alloys, over-exposure to high temperature should be avoided as it could result in excessive scale formation and surface phase changes due to reaction with interstitial elements such as oxygen and nitrogen. The forging pressure required to deform

titanium depends on alloy composition, temperature, die geometry and strain rate. The average value of flow stress required to forge titanium alloys is far higher than that for steel and aluminium [26].

Most titanium alloys are usually hot worked in the α +β phase range. Both alpha and beta phases exist in the microstructure at all times. The amount of alpha and beta depends on the processing temperature relative to the alpha/beta transus temperature. Figure 1.3 shows the variation in % alpha in the alpha/beta phase field with forging temperature. From figure 1.3 it can be seen that at higher processing temperatures in the α+β region, more β will be available to transform on cooling.

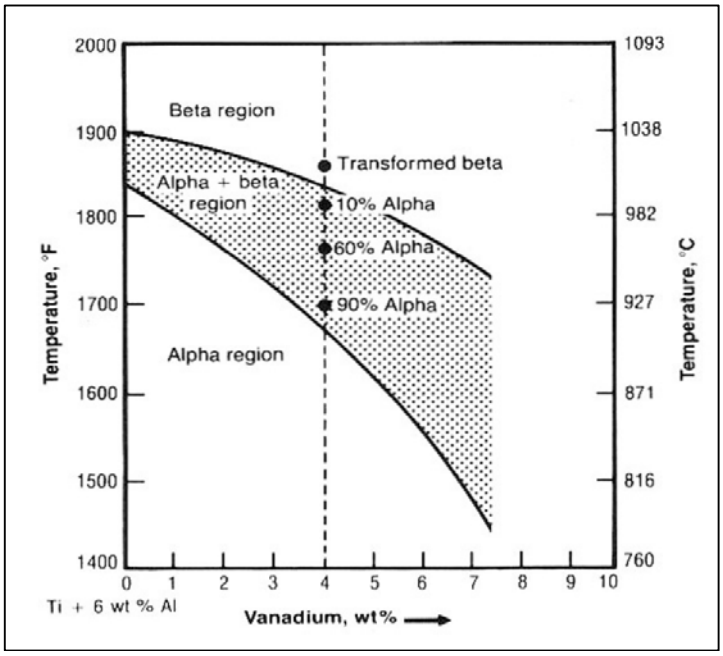

Figure 1.3: Phase diagram to predict results of titanium forging practice [27]

Because of its lower density and heat capacity, during forging, titanium has a tendency to instantly lose heat to the colder dies and the surrounding environment compared with other materials such as steel. It is recommended that for forging titanium alloys the dies are heated to a high temperature so that forging can be carried out isothermally as far as possible. Isothermal forging can be expensive but can improve the overall quality of the final titanium forgings.

1.3.6 Effect of temperature on titanium alloy forging

During forging the deformation characteristics of nearly all titanium alloys are sensitive to temperature [28]. Figure 1.4 shows typical forging pressure requirements for different titanium alloys. It can be seen from the figure that for these selected titanium alloys, the forging pressure increases significantly with decreasing forging temperature. Interestingly, the forging pressure for α alloy Ti-8Al-1Mo-1V increases nearly three times as the forging temperature decreases by 90 °C. Such temperature variations could restrict the material flow in the forging die, thus it is important to minimise the heat losses when transferring the work-piece from the furnace to the forging die and during contact of the work-piece with the cooler forging die.

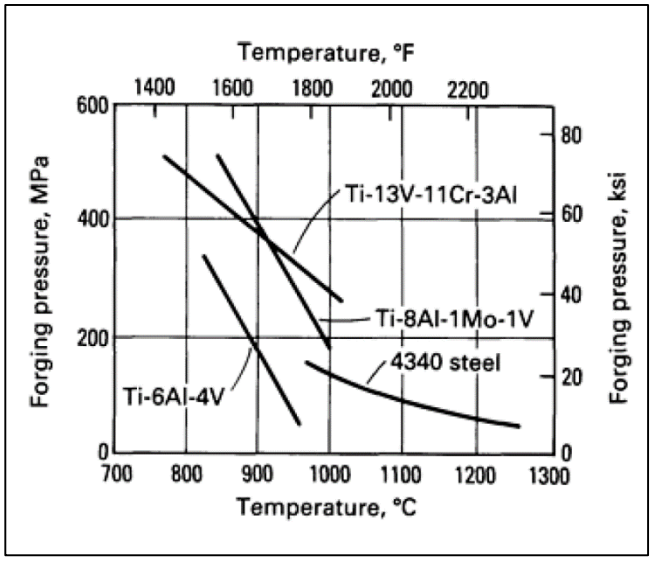

Figure 1.4: Forging pressure vs. temperature comparison for different classes of titanium alloys [28]

1.3.7 Effect of flow stress during the forging of titanium alloys

The effect of temperature on flow stress in titanium alloys differs with alloy type. Figure 1.5 shows typical flow stress curves for α, α + β and β titanium alloys. From figure 1.5 (a), it can be seen that a more difficult to forge α titanium alloy (Ti-8Al-1Mo-1V) shows a greater sensitivity to temperature. For instance, the flow stress at 900° C is two to three times higher than that of the alloy at 1010° C. The α + β alloy (Ti-6Al-4V), shown in figure 1.5 (b) also shows a higher sensitivity to temperature but to a lesser extent to that of α titanium alloys, especially at higher levels of total strain [24].

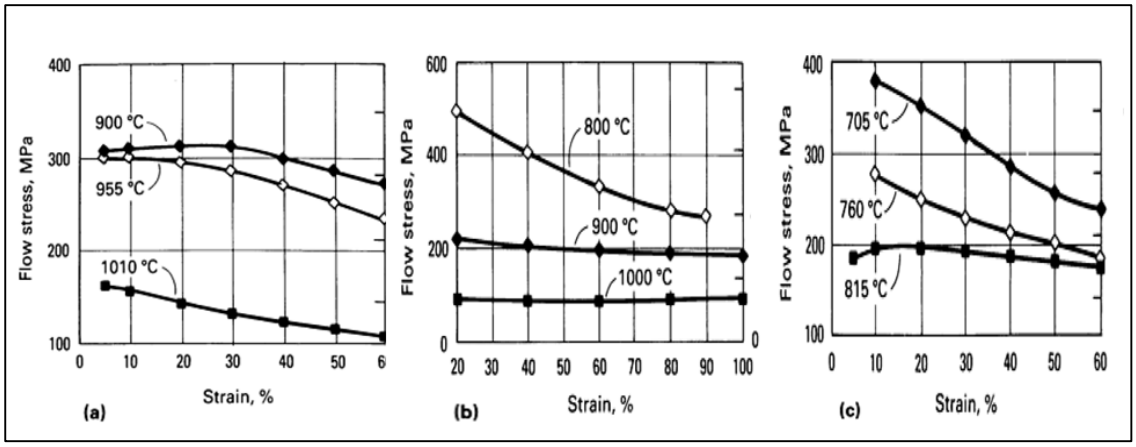

Figure 1.5: flow stress curves for (a) CP-titanium, (b) Ti6Al4V and (c) Ti-8Al-8V-2Fe-3Al at different temperatures [28]

At 1000 ° C, an α + β titanium alloy, shown in figure 1.5 (b), is above the nominal beta-transus temperature (950° C to 995° C) for the alloy, and the structure, being entirely body centre cubic (BCC), is relatively easy to deform. From figure 1.5 (c) it can be seen that the β titanium alloy (Ti-10V-2Fe-3Al), shows a lesser sensitivity to temperature at higher levels of total strain. Also it is worth mentioning that the beta-transus temperatures for these classes of alloy are lower than the beta-transus temperatures of α and α + β titanium alloys. This is significant, as a β titanium alloy when forged below the beta-transus temperature, will flow more easily. However, at higher strain rate above the beta-transus temperature, the flow stress reduction achieved by deforming β alloys is less than that for α and α + β titanium alloys. Table 1 shows recommended forging temperature ranges for common titanium alloys.

Alloy type	**Beta-transus temperature,(℃)**	**Forging temperature range (℃)**
α or near α alloys		
Ti-CP	915	815-900
Ti-5Al-2.5Sn	1050	900-1010
α + β alloys		

Ti-6Al-4V	995	900-980
Ti-6Al-6V-2Sn	945	845-915
β, near β and metastable β alloys		
Ti-8Al-8V-2Fe-3Al	775	705-925
Beta C (Ti-3Al-8V-6Cr-4Mo-4Zr)	795	705-980

Table 1: Recommended forging temperatures for common titanium alloys [28]

1.3.8 Effect of deformation rate on forging titanium alloys

Titanium alloys are highly strain rate sensitive during high temperature forging. Figure 1.6 shows typical flow stress curves for three classes of titanium alloys (i.e α α+β, and β alloys) forged at three different strain rates at three temperatures (α alloy Ti-8Al-1Mo-1V at 955 °C, α-β alloy Ti-6Al-4V at 900 °C and β alloy Ti-10V-2Fe-3Al at 815 °C). It can be seen that for each of these alloys, as the deformation rate is reduced from 10/s to 0.001/s, the flow stress can be reduced by a significant amount (nearly ten times).

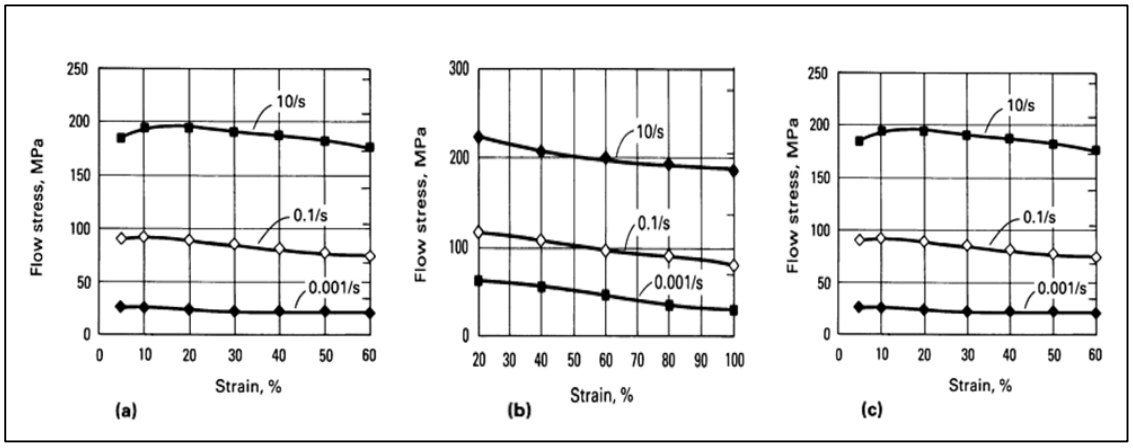

Figure 1.6: Flow stress curves for (a) CP-Titanium, (b) Ti6Al4V and (c) Ti-8Al-8V-2Fe-3Al titanium alloys at different strain rates [28]

From figure 1.6 it can be seen that the flow stress of an α+β titanium alloy at a temperature 900°C, at 50% strain and with a strain rate of 10/s is 205 MPa, which is nearly four times higher when compared to the flow stress at a strain rate of 0.001/s.

Due to the strain rate sensitivity of most titanium alloys, it is generally advantageous to deform these alloys at relatively lower strain rates in order reduce the resistance to deformation during the process [22]. However, when forging under non-isothermal conditions where the temperature of the dies is relatively cold, the benefit of low strain rate forging is outweighed by substantial heat loss to the die and surroundings.

1.4 Introduction to powder forging (P/F)

The early efforts [2, 3, 29] by powder metallurgy (P/M) industries to obtain high density parts led to the development of the powder forging process. Powder forging (P/F) involves the production of high strength P/M components by powder compaction/ sintering followed by consolidation of the powder by hot forging to attain the final density. The final density obtained by powder forging is closer to full density. Powder forging first appeared during the late 1960s due to the market drive towards higher density, higher performance with a potential for lower cost through material savings.

During the 1970s, the first production PF connecting rod was introduced by GKN for the Porsche 928 engine [3]. Powder forging gave Toyota an edge over its competitors on cost reduction by utilising a Fe-Cu-C powder mixture. Embracing Toyota's success in Japan with PF, the Ford motor company implemented and took a lead in PF in the mid-1980s, which was then followed by GM (General motors) and Chrysler in the US. In Europe, the acceptance of the technology occurred during early 1990s with BMW and Jaguar introducing PF in their production lines [3]. The powder forging process has been widely used in the manufacture of parts for many critical structural and high performance applications such as connecting rods, gears and transmission shafts as shown in figure 1.7. Powder forging enhances the geometric precision with improved load bearing capability. It overcomes the mechanical property limitations imposed by the residual porosity in conventional P/M processes.

Figure 1.7: Powder forged automotive parts [30]

1.5 Powder forging process

The powder forging process, involves axial compression of a powder preform to develop a full density finished part. The process has three different stages i.e. compaction, sintering and forging as discussed below;

1.5.1 Compaction stage

During the compaction stage the metal powder is gravity-fed into a cylindrical die, the powder is then axially pressurised into a dense mass known as “powder compact”. After the compaction the powder compact is ejected out of the die. Compaction is commonly performed at room temperature and under controlled pressure depending on the density requirements. For powder forging, the powder compacts usually have a shape closely resembling the finished part. The relative density of these powder compacts varies from 60 to 75 per cent of the full theoretical density, which means that that there is sufficient strength for handling and transporting to the furnace or die.

1.5.2 Sintering stage

In the sintering stage, the powder compact is placed inside a controlled atmosphere furnace, where it is heated below the melting point of the base metal and held at the sintering temperature and cooled. At the sintering stage, diffusion of atoms occurs at a high temperature which is driven by a reduction in the free surface energies of small

particles. Smaller particles usually sinter faster because of the high specific area and energy [31]. The bonding between particles during sintering is evident on the microstructural scale as seen by neck growth, where small neck grows at the sinter bonds between particles [1, 26]. The particle bonding is associated with elimination of pores, an increase in density, sinter bonding neck size and the shrinkage of the powder compact. During sintering it is common for a powder compact to undergo significant shrinkage or dimensional change as it densifies. The relative density obtained after sintering depends on the sintering time, temperature and the material and is often characterised by "sintering densification curves".

1.5.3 Powder compact forging

In powder compact forging, a semi-consolidated powder preform is heated to a temperature in a controlled atmosphere induction furnace and held at a high temperature for certain duration depending on the material. After induction sintering stage, the powder compacts are transferred to the die and forged to the final required shape.

1.6 Advantages of powder forging

- A primary advantage of powder forging is its ability to attain near net shape parts with maximum material utilisation. This is crucial for expensive materials like titanium where enormous savings can be achieved from reduced machining costs.
- There is a potential for manufacture of high performance components with improved mechanical properties resulting from full densification.
- The production of a wide range of alloys using mechanical blending and a blended elemental approach.
- It is suitable for high volume production of components.

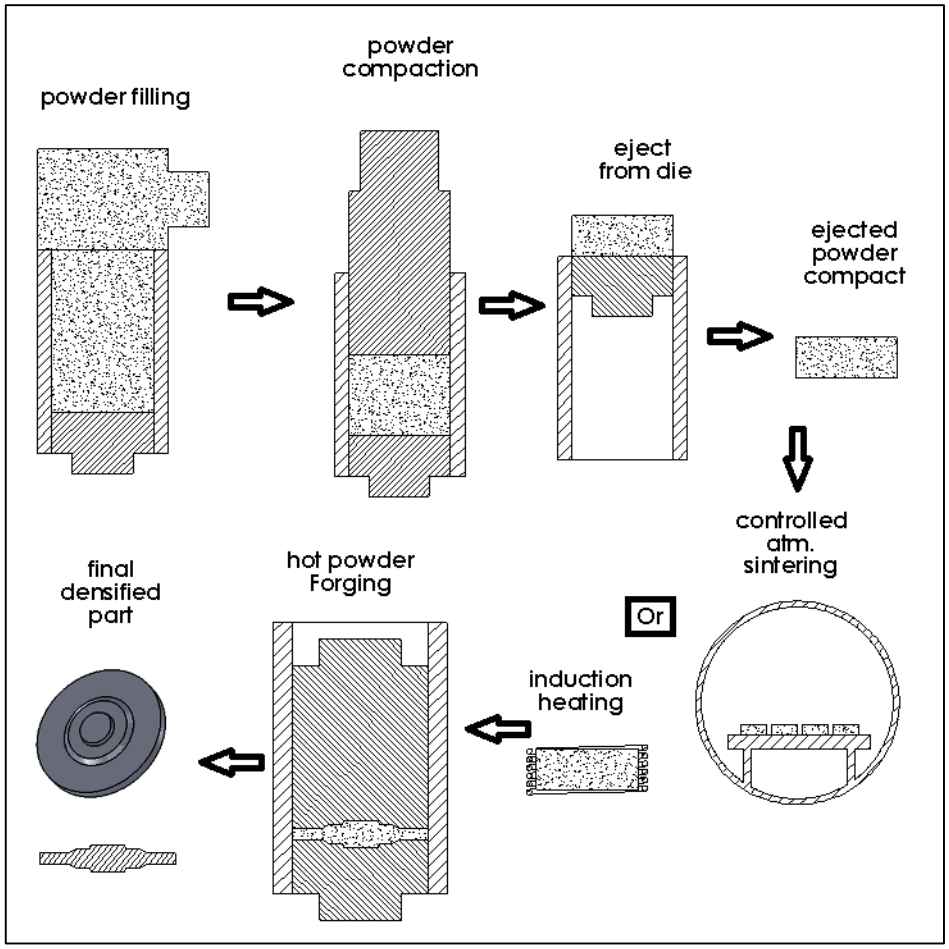

Figure 1.8: Schematics of powder forging.

1.7 Powder forging classifications

The powder forging process can be classified in two different ways, the first is based on the type of forging-sintering sequence opted used e.g. cold forging, forged sintering, sinter-forging and direct powder forging as illustrated in figure 1.9. Secondly, based on the type of material flow during deformation; such as in hot upsetting and hot repressing.

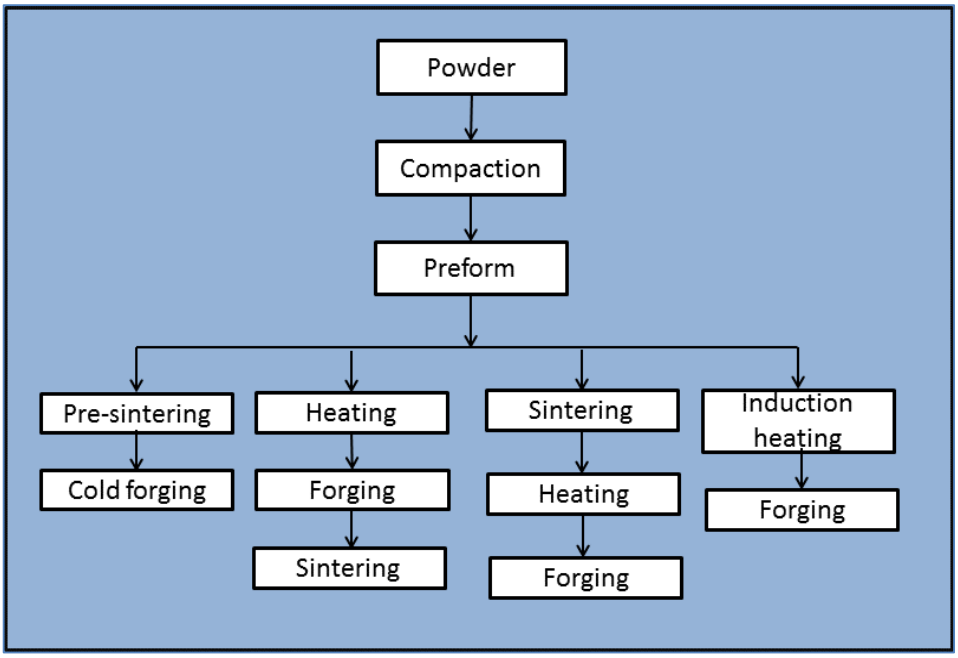

Figure 1.9: Powder forging classifications [32]

In cold forging, the powder compact is pre-sintered and cold pressed to achieve the density requirement. Cold forging is commonly adapted for ferrous products such as P/M gears and bearings. In forge sintering, the powder compact is first forged to a given minimum density and then fully sintered in a furnace to the required final densification. This method is prevalent when selective densification is necessary. In sinter-forging, which is a widely accepted powder forging technique, a powder compact is sintered and immediately transferred to the forging press and forged. The key advantage of this process is that an additional heating stage can be avoided by carefully controlling the process cycle. Sinter-forging is widely used in the automobile industries in the production of connecting rods. Lastly, direct powder forging, or powder compact forging, which is a relatively new process where, a compact is induction heated in a controlled atmosphere and the final density is achieved by forging. The key benefit of this process, especially in the case of titanium alloys, is that the cost is kept low by avoiding a separate sintering cycle.

1.7.1 Hot upsetting

In hot upsetting the material undergoes a significant amount of material flow in a direction lateral to the applied force. In upset powder forging the material flow in the unconstrained lateral direction causes a stress state across the pores which is a

combination of normal and shear stresses [2]. The circular pores under the normal load become flattened and elongated in the direction of material flow. The shear stress induced by a sliding motion breaks down any residual inter-particle oxide films and promotes strong metallurgical bonding across collapsed pore interfaces.

1.7.2 Hot re-pressing

In hot re-pressing, the material flow during densification is in the direction of application of the applied force. The hot re-pressing powder forging process leads to a small difference between the vertical and horizontal stresses which causes lower material flow in the lateral direction. During densification the stress state approaches pure hydrostatic with no material movement in the horizontal direction. While lateral material flow occurs, the circular pores within the material flatten and the opposite sides of the pore are brought together under pressure. Reduced inter-particle movement compared to those found during up-set powder forging may result in low ductility and fracture toughness.

In powder forging, the role of porosity as a factor which limits the level of mechanical properties is well understood from previous studies [29, 33]. The voids between particles act as a site for fracture initiation and a path for crack propagation, hence elimination of pores by deformation processing is required for achieving static mechanical properties (i.e. tensile strength and ductility) that are directly related to residual porosity [2]. However, dynamic mechanical properties (i.e. fatigue and impact resistance) are not only affected by porosity but also by the material flow during plastic deformation. It has been documented that obtaining full density by lateral material flow results in parts with superior mechanical properties than those developed by repressing deformation [34].

1.7.3 P/M of titanium and titanium alloys

There is general an interest in using PM titanium technology as an alternative to manufacture titanium parts to lower the cost [20, 25]. In addition, the production of parts with full density and with good strength and ductility, or parts with controlled

levels of porosity, can be made using a P/M route for customised applications. The mechanical properties vary with levels of porosity.

A few years ago, titanium powder was considered to be very expensive, however novel methods of producing homogenous titanium powder alloys have been developed [26]. As a result of this low cost titanium powders are becoming more commercially available and near net shape parts can be produced with significantly reduced costs. Manufacturing of complex titanium components that are considered to be challenging and expensive by conventional methods can be easily achieved by P/M techniques provided there is readily available low cost powder. A combination of low cost titanium powder with near net shaping technology has a potential to initiate a paradigm shift in the applications of titanium metal [25].

1.8 Powder forging of titanium and its alloys

As highlighted in section 1.7.3, the production of titanium components using a P/M route appears to be an effective way to reduce costs. Several researchers have investigated the consolidation of titanium alloys using a powder forging technique. Weiss et.al [35] investigated powder forging of titanium alloy Ti-6Al-4V and its effect on microstructure, pore closure, tensile and fatigue properties. The samples obtained after forging revealed equiaxed α grain structures that enhanced fatigue properties. Zhao et al [36] studied the effect of isothermal forging of powder compacts produced via a HIP route. Their results indicated an improvement in properties and microstructure of titanium alloy components produced by powder forging. A study was carried out by Qiu et. al. [37] to optimize the processing parameters for a titanium alloy connecting rod produced by a powder forging technique. They investigated the deformation energy required for powder forging a titanium alloy connecting rod and the role of deformation temperature. Recently, near net shaping techniques were reported by Oak Ridge National Laboratory involving titanium parts fabricated using a single step process using titanium powder produced by the Armstrong process ™ [38]. The processing technique described in this work is equivalent to hot consolidation of the titanium powder in an encapsulated steel tube and sintering at high temperature followed by forging and extruding to the final shape.

1.9 Factors affecting the quality of titanium powder forged parts

Several factors affect the quality of powder forged products. These include material flow stress, forging temperature, pressure, tooling setup and density distribution. Processing titanium metal requires additional precautions due to its affinity to interstitial impurities such as oxygen, nitrogen and hydrogen. Often high temperature processing of titanium alloys requires a vacuum or controlled atmosphere to avoid contamination from these impurities.

1.9.1 Forging pressure

It is well documented that forging pressure has a direct influence on the consolidated density. This is due to the fact that at higher pressure the pores tend to close more effectively irrespective of the forging temperature. However, the amount of forging pressure that can be applied during both compaction and forging depends on the capability of the press equipment. Also, higher pressure can lead to premature failure of the tooling involved; thus it is necessary to determine the optimum pressure that is required for the process.

1.9.2 Forging temperature

As illustrated in section 1.3.5, forging titanium alloys requires high temperature. Generally titanium alloys are hot worked near the beta phase temperature region because at this region the titanium metal has a (body centred cubic) BCC structure which is easier to deform. It is important to mention that since titanium powder compacts have a porous structure and low thermal conductivity, they are often difficult to heat and maintain at a specific temperature during forging. Though the flow stress required for powder forging is lower at higher temperature, there are limits to which a powder compact can be heated and held at high temperature due to incipient melting. However, too high a forging temperature could negatively impact on the tooling life.

1.9.3 Titanium powder

The ability of titanium powder to be effectively compacted and the resulting properties of a compact before and after powder forging depend on the characteristics of the starting powder. Powder characteristics such as particle shape and size, apparent

density, internal microstructure, chemical composition, flowability, compressibility and the surface condition of individual powder particles plays a crucial role in the dynamic behaviour of the powder during compaction and material flow during powder forging. Titanium powders that are used for powder forging applications can be classified based on the powder shape into blended elemental powder and pre-alloyed powder.

Commercially available titanium powders are commonly produced by the Kroll process which involves chlorination of titanium oxide rich ore in the presence of carbon and the resulting product reacted with magnesium to produce titanium sponge. The sponge is ground to a particle size ranging from 45 to 185 μm. These fine particles are then alloyed with other metals to produce a blended powder. These powders when compacted and sintered under a high temperature can achieve up to 99.9% densification. A blended elemental approach has been successfully used at Toyota to produce valves [39].

Pre-alloyed titanium powders can pre produced by several techniques, for example by using a hydride-dehydride process (HDH) where metal scraps or machine turnings are cleaned and hydrogenated to produce a brittle material which is then ground to fine a powder. The quality of pre-alloyed titanium powder is generally much higher than that of blended elemental powder, and is suitable for high value applications such as aerospace. HDH powders containing hydrogen on the other hand retains low oxygen level when sintered in hydrogen atmosphere under a controlled sintering cycle. This is achieved by heating the powder compact to a temperature range of 200℃ to 300℃ and holding it at up to 60 minutes before proceeding to the full sintering cycle [40]. At this condition it is found that hydrogen release from HDH powder plays an important role in titanium powder particles with respect to oxygen. The emitted hydrogen thus benefits sintering kinetics in HDH powder articles by reducing surface oxides and enhancing diffusion [41].

1.10 Tooling design considerations for titanium powder forging

Appropriately designed forging tools or dies are an important element in the successful production of powder forged parts, as they not only provide the desired shape, but should also be reliable and give repeatability. Since the tooling cost constitutes a major part of the overall process cost, every effort must be made to ensure that they do not fail during the powder forging operation. The final dimensions and tolerance of the part produced directly relates to the die geometry, hence careful attention must be paid to proper die dimensioning. Furthermore, special consideration needs to be made in the selection of a die material and heat treatment requirements for optimum performance during operation. In the next section some of the technical requirements while designing compaction and forging dies are discussed.

1.10.1 Powder compaction die design

As discussed in section 1.7, the material flow during powder forging improves the mechanical properties of the final part; however large deformation can also lead to fracture of the part during powder forging. The following factors need to be taken into consideration while designing the powder compaction tools:

- The die cavity must be easy to fill and be able to accommodate the exact quantity of powder required depending on the weight of the final part.
- The density distribution in the powder compact after compaction must be as uniform as possible
- Apposite tolerance between the punch and the die for smooth movement during compaction.
- The die material should have high strength and toughness to withstand compressive and hydrostatic stresses during compaction; also it should have high wear resistance on the inner surfaces.
- The powder compact should be easy to eject after compaction without damaging the die.

The most commonly used die materials are an H13 tool steel for warm compaction with a surface hardness up to 54-56 HRC; and a D2 cooled working tool steel for cold compaction.

Powder compaction dies can be classified depending on the pressing action, as giving single action compaction or double action compaction. Figure 1.10 illustrates the schematics of single action press compaction and dual action press compaction with respective relative density variations. In single action compaction, the powder compact is produced by a single action of the top punch, while the bottom base remains stationary. The overall relative density obtained by single action pressing is low compared to dual action pressing. The density variation is high with this type of compaction, with the highest relative density at the top right corner and lowest relative density at the bottom corners as shown in figure 1.10. Meanwhile in dual action compaction pressing the powder compact is produced by the dual action of the punch. Dual action powder compaction is quite popular in the P/M industry because it gives a more uniform density. It can be seen from the density plot in figure 1.10 that the relative density is lowest in the middle and highest at the top and bottom corners of a powder compact. The movement of the dual punch can be simultaneous or synchronous depending on the press machine and density requirements.

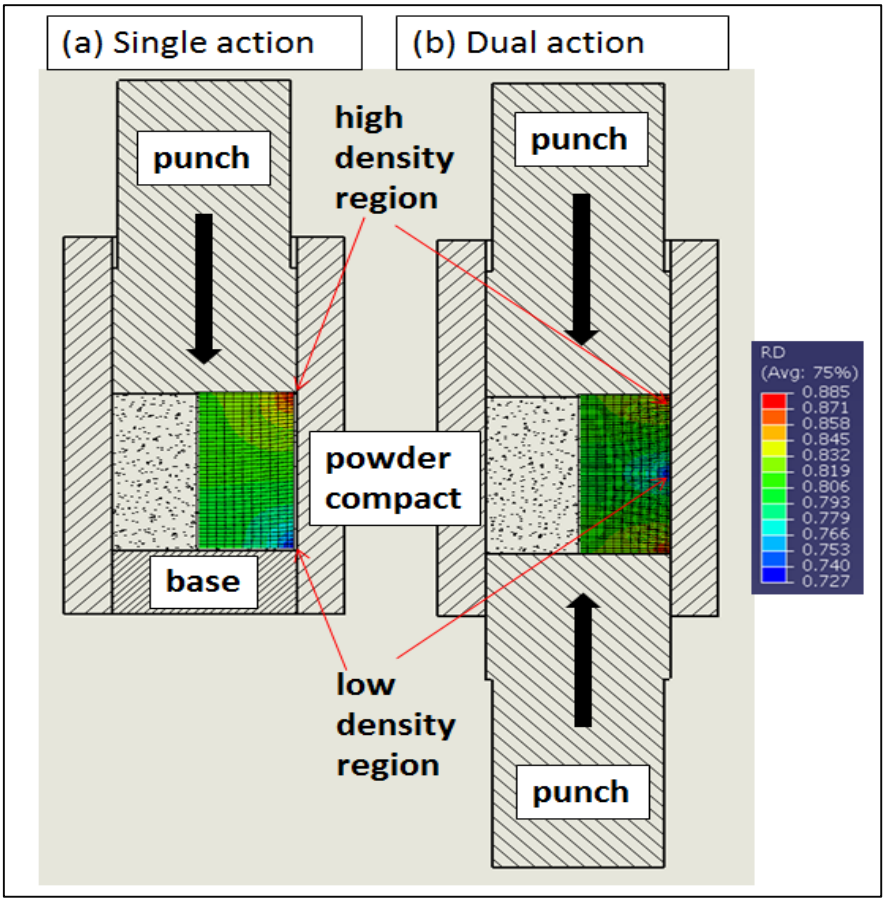

Figure 1.10: (a) Single action compaction; (b) dual action compaction

A high density, uniform powder compact is a necessity for producing a quality powder forged part. High variations in relative density can lead to distortion during sintering and a high temperature gradient during induction heating. This problem can be significantly reduced by using dual action pressing but it requires a press machine that is capable of applying biaxial pressure which leads to high initial cost. An alternative to dual action pressing is through using a floating-die tooling principle as shown in figure 1.11, where the die is mounted on springs which balance the weight while the upper punch exerts the necessary compaction pressure. After compaction, pressure is applied to the die which forces the bottom support to move the powder compact upwards to eject the part.

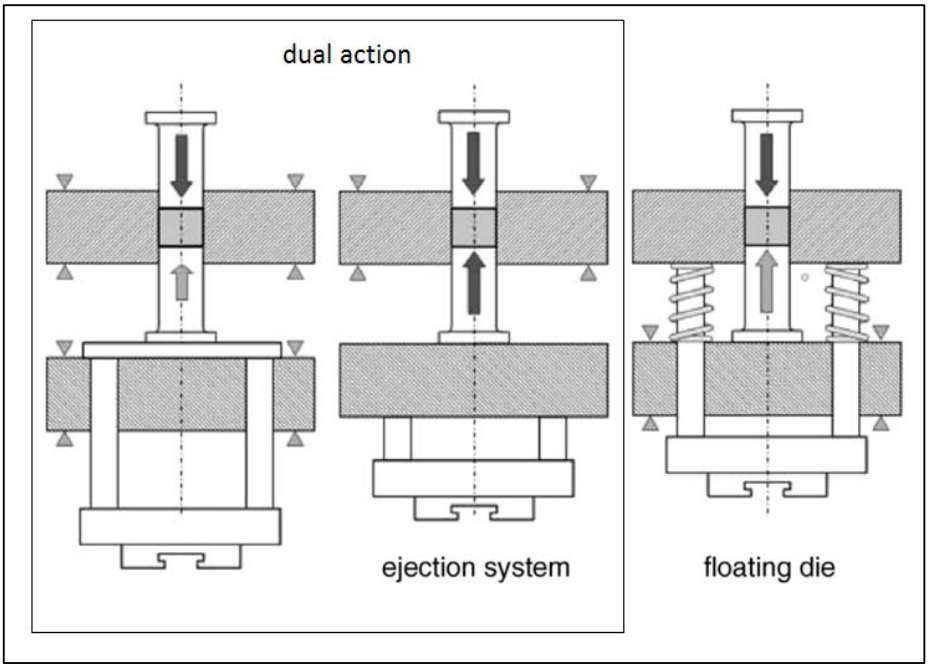

Figure 1.11: Tooling principle using a floating die [42]

The only drawback of a floating die arrangement is that the design tends to be sophisticated for parts that require multi stage compaction [42].

1.10.2 Powder forging die design

The dies for powder forging are similar to those used for ingot metal forging, except that in many cases the material is completely deformed in the die cavity (i.e. no flash formation). The tooling often contains the profile of the final part to be forged. Die corners are provided with a large radius for easy flow of material under deformation. Closed die forging has emerged as a trend in powder forging compared to traditional impression die forging for two reasons;

- Near-net precision, with minimum machining required after forging; therefore maximum material utilisation.
- Low stresses on the die during deformation, hence increased tooling life.

A major drawback of closed die forging is a reduction in material flow and grain deformation which might affect the mechanical properties of the final part. In closed die forging there is no allowance for excess material, a preform which is relatively large in size could overload the tooling and subsequently the press itself.

Isothermal forging principles are commonly adopted for forging titanium alloys. In isothermal forging, the forging dies and the raw titanium billet is heated to a high temperature called an 'iso-thermal condition'. When under iso-thermal conditions, as the load is applied through the die on to the billet, the heat transfer between the billet and the die interface is significantly reduced, and thus the material flow characteristics are improved. Since most titanium alloys have high flow strength, the load requirements for forging could be reduced to a great extent by iso-thermal forging.

1.11 Powder compact or preform design

Designing an optimised powder compact starting shape for powder forging is important as it directly influences die filling and the occurrence of defects such as laps, seams, and 'flow-through' (a shear related defect caused by excess metal flow at already filled regions in the die). The initial powder compact geometry can also influence the final grain size, density distribution and plastic deformation after powder forging. Also, it is important to mention that; the ease of making a powder compact can significantly influence the overall economics of the powder forging process. Thus, the cost of producing a powder compact must be kept as low as possible for powder forging to be competitive.

1.12 Density distribution of initial powder compacts

The relative density distribution in a powder compact often varies for different materials. A density-pressure curve relationship is a widely used method in P/M industries to study the compaction behaviour of different types of powder [31]. Figure 1.12 shows a typical density-pressure curve obtained by cold compaction of Ti-6Al-4V alloy powder produced by Armstrong process™.

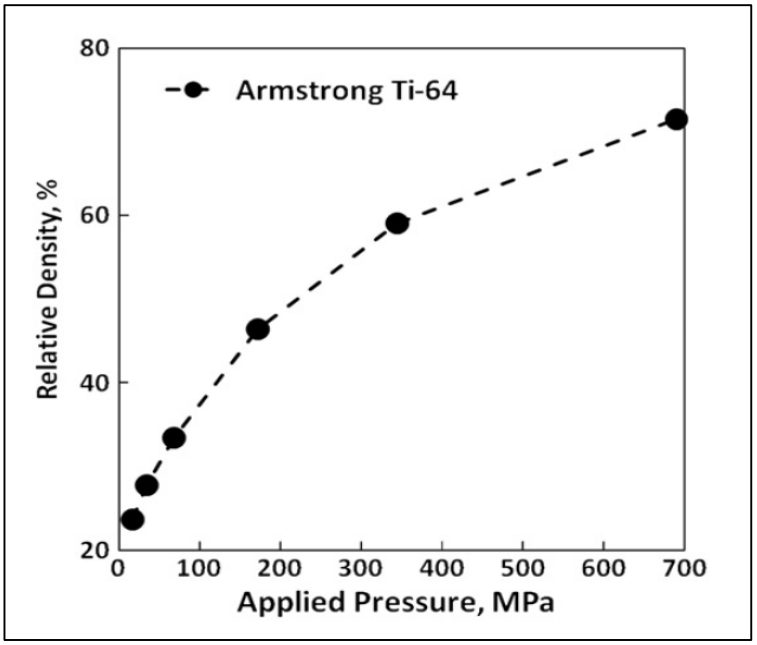

Figure 1.12: Relative density of Ti-6Al-4V powder as a function of applied pressure [43].

It can be seen from the above figure that the relative density increases monotonically with the applied pressure, however the slope of the curve decreases as a result of low compressibility at higher pressures. James [44] reviewed the mechanisms governing the powder consolidation process. In the first stage of powder compaction, the particles re-arrange themselves by flowing past one another and the new packing arrangement is referred to in some literature as 'transitional restacking'. In this stage the total void volume reduces due to sliding of particles on each other. This stage comes to an end by an interlocking of particles due to frictional forces when the pressure increases. In the second compaction stage the densification is attributed to both elastic and plastic deformation of particles. In this stage, individual particles deform plastically and become flattened so that they form additional contact with each other [43]. In the third stage of compaction, final densification occurs by cold working, with or without particle fragmentation.

In a powder forging simulation procedure, the initial density distribution in a powder compact is critical. The densification behaviour depends on powder characteristics such as plastic deformation, surface hardness, work hardening and the degree of adhesion of the particles [34]. It can be seen from figure 1.13 that the final relative density after compaction could be non-uniform.

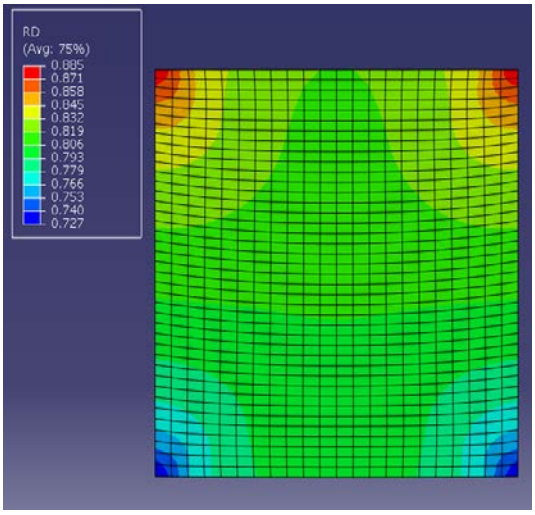

Figure 1.13: Typical relative density distribution after compaction [43]

The several processing parameters that influence the final density distribution of the powder compact are given below;

- applied force on the powder
- die filling and powder morphology
- geometrical constraints in tooling
- compaction temperature
- friction and lubrication conditions

Several researchers have demonstrated that titanium alloy powders can be compacted to high densities [34, 43, 45] and both cold compaction and warm compaction techniques have been investigated. The dynamics of compaction of titanium powder is similar to the compaction of traditional powder metallurgical materials; however the flow behaviour has been found to be different. As the flow stresses for various titanium alloys are different, the pressures required for consolidation are also different. For example, titanium powder Ti-6Al-4V requires a higher pressure compared with pure titanium.

2 Constitutive equations

2.1 Modelling powder forging by the finite element method

The Finite Element Method (FEM) is an analytical engineering tool developed in the 1960s to find solutions to complex problems experienced in structural mechanics and fluid dynamics [46]. Although originally developed to determine stresses in structural mechanics problems, today it has been extended and applied to analyse problems that are related to manufacturing processes. From a mathematical point of view, the finite element method involves finding the approximate solutions of partial differential equations [47]. The main characteristic of FEM is its ability to discretize a continuous domain into a set of sub domains that can be numerically solved iteratively.

The importance of FEM simulation has been well understood in the metal forming industry since the 1960s. Manufacturing a part by forging can in the first instance require a trial and error approach to optimise the tool and die cavity shape. The main purpose of simulation in metal forming is not to replace practice, but to support it by visualising the material flow and process variables even before the manufacture of the tool or dies begins [48]. Recently several commercial software packages have been developed to solve complex metal forming problems [49, 50]. Numerous FEM solvers have been developed to predict instantaneous flow velocities, strain rates, strains, stresses, relative densities and temperature distributions within the deforming material. A reliable FEM program for metal forming simulation should give the following [48];

- the material flow (i.e. viscoplastic or rigid plastic) behaviour at high temperature and the dependence of the material flow rate to the strain rate;
- a display of the grain flow pattern occurring within the material during the deformation process;
- the influence of the temperature distribution both inside the material and at the boundary with the contacting tools;
- the influence of mechanical strains on the thermal history of a work piece and the dies;

- the influence of tooling velocity or displacement on the deformation history of the work piece.

According to various constitutive models used for material deformation, FEM in metal forming can be classified as elastic-plastic, rigid-plastic, rigid-viscoplastic or elastic-viscoplastic [51]. Figure 2.1 shows the classification of different materials flow models with respect to stress-strain curves. From figure 2.1 it can be seen that in rigid-plastic and rigid-viscoplastic analysis the elastic portion has been neglected. The major difference between plastic and viscoplastic is that flow stress is strain rate dependent in visco-plastic material models, while in plastic models, the strain rate has no influence on stress [52]. For general metal forming simulation, where large deformation is expected, elastic-plastic FEM (Prandtl-Reuss constitutive relation) and rigid-plastic FEM (Levy-Mises constitutive relation) are adopted and have been proven to give similar results [51].

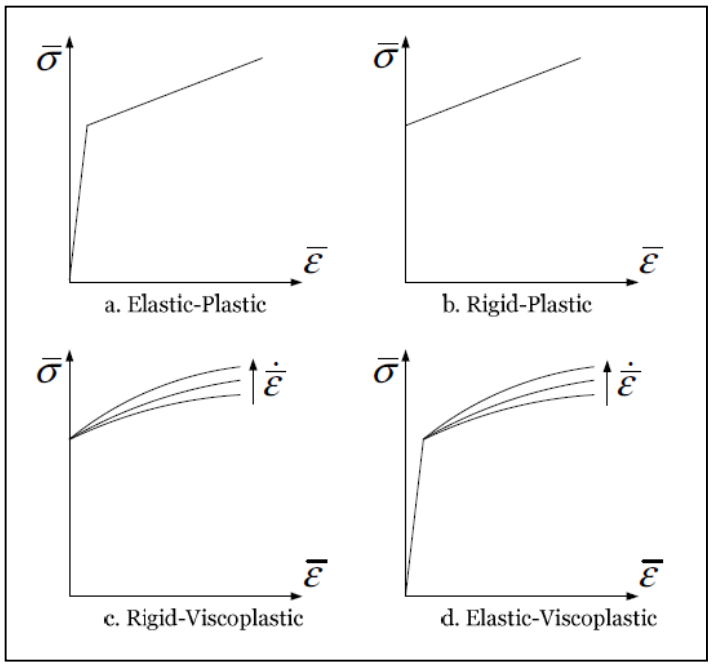

Figure 2.1: different types of material flow curves [51, 52]

During the past few decades, a number of finite element analysis procedures for modelling powder metal forming processes have been reported in the literature. These analyses are broadly grouped by the type of presumed material flow behaviour as elasto-plastic [53-55], rigid-plastic [56, 57] and elastic-viscoplastic types [58, 59]. From the literature, it can be said that the elasto-plastic and the rigid-plastic material

models are suitable for powder compaction and sinter-forge applications, whereas elastic-viscoplastic material models are acceptable for powder compact forging and powder compact extrusion processes. This is due to the fact that in powder compact forging the material is strain rate sensitive and exhibits viscous behaviour during high temperature deformation.

As a powder forging process generally involves both material and geometric nonlinearities, the step size required for an accurate integration is small. An elasto-plastic analysis may be necessary if the residual stresses need to be determined, whereas a rigid-plastic analysis is suitable if the load or pressure required for the deformation needs to be estimated.

2.2 Finite element formulations

While modelling the material flow behaviour in powder forging it is important to relate the stress and hydrostatic pressure to the strain rate and the density. In this section, we discuss the rigid-viscoplastic and thermo-elastic viscoplastic formulations as these two material flow behaviours are common in forging simulations.

2.2.1 Rigid-viscoplastic (RVP) FEM

Rigid-viscoplastic FEM is used to analyse problems related to optimisation of the process technology, for example tooling design, defect predications such as wrinkles or cracks and the evaluation of product formability. Traditionally rigid-viscoplastic FEM is based upon the rigid-viscoplastic variation principle and can be solved by numerical iterations such as the Newton–Raphson method. The variables and computational capacity required are relatively low, however difficulties such as convergence problems do exist. These convergence problems are due to difficulties with the contacts, rigid zones and frictional forces.

The variation principle can be described as: among admissible velocities that satisfy the conditions of compressibility and incompressibility, as well as the velocity boundary conditions, the actual solution gives the following function a stationary value,

$$\pi = \int_V E(\varepsilon_{ij})dV - \int_{Sf} F_i u_i dS \qquad 2.1$$

where, π is the variational function, $E(\varepsilon_{ij})$ is a work function, and is described as

$$E(\varepsilon_{ij}) = \int_0^{\varepsilon_{ij}} \sigma_{ij} \mathrm{d}\, \varepsilon_{ij} = \int_0^{\varepsilon} q \mathrm{d}\varepsilon \qquad 2.2$$

When the incompressibility condition is considered using a penalty function method, the incompressibility constrain on the admissible velocity in equation 2.2 is eliminated by introducing a penalty constant α and the above function can be written as;

$$\delta\pi = \int_V q \cdot \delta\varepsilon \cdot \mathrm{d}V + \alpha \cdot \int_V \varepsilon_V \cdot q \cdot \delta\varepsilon_V \cdot \mathrm{d}V - \int_{SF} F_i \delta u_i dS \qquad 2.3$$

where, q, ε, ε_V, F_i and α are the effective stress, effective strain rate, volume strain rate, surface traction and penalty constant. Several studies for example, Cocks [60], Sofronis and McMeeking [61], Michel and Suquet [62], have modelled porous material using a rigid-viscoplastic modelling approach.

2.2.2 Elasto-viscoplastic (EVP) FEM

An elasto-viscoplastic modelling approach is applied in metal forming simulations when materials are strain rate sensitive. The method is particularly suitable for modelling high temperature deformation of materials subjected to arbitrary loads and temperature histories as encountered in forging operations. The constitutive equations for elasto-viscoplastic behaviour, based on an additive decomposition of the strain rate for an isotropic material, can be written as;

$$\dot{\varepsilon} = \dot{\varepsilon}^{el} + \dot{\varepsilon}^{pl} \qquad 2.4$$

where, $\dot{\varepsilon}$ is the total strain rate, $\dot{\varepsilon}^{el}$ is the elastic strain rate and $\dot{\varepsilon}^{pl}$ is the plastic strain rate respectively. The relationship between the bulk modulus (K), shear modulus (G), Poisson's ratio (v) and the Young's modulus (E) is given by the following equations;

$$K = \frac{E}{3(1-2v)} \qquad 2.5$$

and,

$$G = \frac{E}{2(1+v)} \quad 2.6$$

The elasticity can be written in terms of the volumetric and deviatoric stress components as shown below;

Volumetric component (p),

$$p = -K \cdot \varepsilon_{vol} = -\frac{1}{3}\ (\sigma_{11} + \sigma_{22} + \sigma_{33}) \quad 2.7$$

where, p is the Von Mises stress, ε_{vol} is the volumetric strain, σ_{11}, σ_{22} and σ_{33} are the stress tensors.

Deviatoric component (S),

$$S = 2\,G \cdot \varepsilon^{el} = \sigma + pI \quad 2.8$$

The flow rule is given by;

$$\delta\varepsilon^{pl} = \delta\overline{\varepsilon}^{pl} \cdot \overline{n} \quad 2.9$$

where,

$$\overline{n} = \frac{3S}{2\,q} \quad 2.10$$

$\overline{\varepsilon}^{pl}$ is the equivalent plastic strain rate, and q is the Von Misses stress.

If the material is rate and temperature dependent, then the yield function is described as below;

$$q = \sigma_0\ (\overline{\varepsilon}^{pl}, \theta) \quad 2.11$$

where, σ_0 is the yield or flow stress, and is given as a function of temperature and equivalent plastic strain rate.

2.3 Modelling approaches in powder forming

In order to simulate the material flow during powder forming it is imperative to understand the different mechanics of powder behaviour while undergoing

deformation. The advanced numerical models for powder forming can be classified as micromechanical models and macro-mechanical models [63]. Micro-mechanical models consider the discrete nature of the powder particles such as particle sliding, crushing, rolling and segregation, while in macro-mechanical models the overall behaviours of the powder mass is treated as a solid continuum [64].

2.3.1 Micro-mechanical approach

Micro mechanical models focus on inter-particle behaviour such as orientation, distribution of porosity, volume fraction of particles etc. The application of this approach however is limited by the discrete nature of the powder and by the fact that a representative portion will be comprised of millions of individual powder particles making the model require a high computational capability. Several researchers [6, 65] that support a micro-mechanical approach assume that the powder is comprised of spherical single sized particles arranged in a regular manner. However, for simulating industrial problems this approach is impractical as it cannot represent the global behaviour [63, 64].

2.3.2 Macro-mechanical approach

A macro-mechanical approach is mostly used in many metals forming problems, and has been adopted in various powder forming simulation studies. Macro-mechanical material models are more reliable to simulate powder forming processes such as powder compaction, sinter-forging and direct powder rolling consolidation. This type of approach is capable of providing crucial information such as yielding behaviour of the powder assembly, density distribution, stress states and compact shape before and after deformation etc. The powder forging process involves thermo mechanical pressing, where the macroscopic behaviour of the material is highly significant as heterogeneous densification can cause failure or fracture in the final part [63].

Both micro-mechanical and macro-mechanical modelling approaches are important and have their advantages and disadvantages when applied to powder compaction and forging. But, from an industrial perspective a macro-mechanical approach has the edge over a micro-mechanical approach as it is able to model the gross behaviour of

the powder which is crucial for industrial scale problems. In this work, we apply Gurson's yield criteria for porous materials to powder forging, which is known to be a micro-macro modelling approach as it incorporates the micro-mechanics of void nucleation [66, 67].

2.4 Porous metal plasticity and advanced yield criterions for porous materials

During the plastic deformation of porous materials, the volume of the material shrinks, as the density of the material increases. This density increase is called densification and is considered to be essential as it improves the physical and mechanical properties of the final part. Following densification during plastic deformation, the plasticity theory of fully dense materials, based on a constant volume condition, cannot be used to analyse the deformation of porous materials. For modelling porous materials, a constant mass condition is often applied [63].

The constant mass condition is expressed as below;

$$d\varepsilon_v + d\varepsilon_p = 0 \qquad 2.12$$

$$\text{or } d\varepsilon_1 + d\varepsilon_2 + d\varepsilon_3 + \frac{d\rho}{\rho} = 0 \qquad 2.13$$

Where, $d\varepsilon_v$, $d\varepsilon_p$ are respectively the volumetric strain increment and density strain increment; $d\varepsilon_1,\ d\varepsilon_2,\ d\varepsilon_3$ are the principle strain increments and $d\rho\ and\ \rho$ are the relative density strain increment and relative density of the porous material. It is considered that, for porous material if the volumetric strain ε_v can be obtained, then it is possible to calculate its relative density from the equation below;

$$(RD), \rho = \rho_o \cdot \exp\cdot(-\varepsilon_v) \qquad 2.14$$

$$d = d_o \cdot \exp(-\varepsilon_v) \qquad 2.15$$

Where, $\rho_o\ \ and\ d_o$ are the initial relative and absolute density of the porous material, and ρ and d are the final relative and absolute densities after plastic deformation.

Generally, dense metallic materials are considered to be homogeneous and isotropic. Mathematically the yielding characteristics of such materials are expressed as;

$$f(\sigma, \sigma_0) = \bar{\sigma} - \sigma_0 = 0 \qquad 2.16$$

where, σ_0 is the yield stress of fully dense material, $\bar{\sigma}$ is the equivalent stress, σ_0 is the octahedral stress and q is the equivalent Von Mises stress and is defined as;

$$q = \sqrt{\frac{3}{2}\ \mathrm{S}:\mathrm{S}} = \sqrt{3J_2} \qquad 2.17$$

where the deviatoric stress tensor S associated with the Cauchy stress tensor σ can be expressed as;

$$\mathrm{S} = \sigma + p_m \mathrm{I} \qquad 2.18$$

where, p_m represents the mean stress or pressure and is defined as;

$$p_m = -\frac{1}{3}\ Trace\ (\sigma) \qquad 2.19$$

Numerous researchers have previously studied yield criteria which include the influence of the hydrostatic stress component and also satisfy the conditions required for the development of the plasticity theory of porous materials [27, 68-70]. Some of these yield criteria will be discussed in detail as they lay the foundation for the present model under investigation.

Kuhn and Downey [27] originally proposed a yield criterion and stress-strain relationship for porous materials by taking the effect of hydrostatic stress on yielding into consideration. They were interested in a description of the constitutive behaviour of sintered powder compacts during forging and re-pressing. They proposed a yield function of the form;

$$f = AJ_2 + B\mathrm{I}_1^2 - C_k^2 = 0 \qquad 2.20$$

Where, A, B and C are parameters that depend on the relative density, k represents the Von Mises yield strength of the base material; I_1 represents the first invariants of the stress tensor σ and J_2 represents second invariant of the deviatoric stress tensor S, which are expressed as follows;

$$\mathrm{I}_1 = \sigma_1 + \sigma_2 + \sigma_3 \qquad 2.21$$

$$J_2 = \frac{1}{2}\,\mathrm{S}:\mathrm{S} \qquad 2.22$$

$$\mathrm{S} = \sigma - \frac{1}{3}\,\mathrm{I}_1\mathrm{I} \qquad 2.23$$

Similarly, a yield criterion was independently proposed by Green [68] based on elastic-plastic analysis assuming material isotropy with distributed voids or cracks in a volume element. Kuhn and Downey alongside Green and co-workers simplified equation 2.20 and is expressed as below;

$$f = {J_2}^{1/2} + B\mathrm{I}_1 \qquad 2.24$$

Therefore,

$$\bar{\sigma}^{\,2} = AJ_2 + B\mathrm{I}_1^2 \qquad 2.25$$

The yield functions in the form expressed in equation 2.20 and equation 2.25 bring in the explicit influence of hydrostatic stress in addition to deviatoric stress components and is considered as an extension of von-Mises yielding concept of fully dense material to the non-dense porous materials. The yield criterion given in equation 2.25 includes I_1as a linear term, which is constant with the behaviour of porous granular materials having limited cohesive strength and large compressive strength. It is however expected that yielding of compacted or sintered metallic powder materials would have similar characteristics under hydrostatic tension and compression [2].

The deformation equation resulting from the above yield criterion gives the predicted Poisson ratio as below;

$$\upsilon = \frac{(1-2b)}{(2+2b)^2} \qquad 2.26$$

where,

$$b = \frac{0.75\left(1-\sqrt[3]{(1-\rho)}\right)\cdot\ln(1-\rho)}{(3-2(1-\rho)^{\frac{1}{4}}} \qquad 2.27$$

The above equations relate the density of the porous material with Poisson's ratio. However it is documented that it overestimates the experimental measurements of Poisson ratio at lower densities and has a low response at higher density [2, 68].

A similar plasticity theory for porous materials was put forward by Oyane [71] by extending the yield criterion to a general stress state. Later work by Shima and Oyane [69] proposed a plastic yield criterion for porous metallic structures fabricated by solid state sintering. Their model has been widely applied for powder compaction at both low and high temperatures [72] as is expressed as below [69];

$$f = \frac{3\,J_2}{\sigma_m^2} + \alpha\,(1-\rho)^{\gamma} \cdot \frac{I_1^2}{9\sigma_m^2} - \rho^m \qquad 2.28$$

where, f is the yield function, I_1 and J_2 are the first and second stress invariants, σ_m and ρ are the flow stress and relative density of the sintered porous material respectively. α, γ and m are material specific constants. In the above equation the flow stress σ_m is given as below;

$$\sigma_m = a + b\bar{\varepsilon}_m^{\,n} \qquad 2.29$$

where, a, b, and n are material dependent constants $\bar{\varepsilon}_m$ is the effective plastic strain of the material. Despite the fact that the Shima and Oyane yield criterion was developed for sintered porous materials, the accuracy was limited due to its underestimation of experimental data for inhomogeneous materials especially in low density regions. Also, the model was found to be not suitable for porous material undergoing deformation at high temperature [73].

Kuhn and Downey proposed a yield criterion based on empirical results (observations of the relationship between Poisson ratio and density). The criterion is given by

$$f = [3J_2 - (1-2v)J_2']^{1/2} \qquad 2.30$$

Where J_2' represents second invariant of stress and is defined as below;

$$J_2' = J_2 - \mathrm{I}_1^{2/3} \qquad 2.31$$

In equation 2.30 the hydrostatic stress is included as a quadratic term through J_2' and satisfies the requirement that the yield criterion be an even function of hydrostatic stress [2]. In a further study carried out by Honess [74], the yield criteria's proposed by Green [68], Oyane [71] and Kuhn [27] were compared on the basis of their ability to predict the densification response and deformation stress during compression, plane

strain compression, re-pressing (closed die forging) and hydrostatic compression. Honess [74] concluded that criteria based on an experimentally determined yield function through Poisson's ratio provided an improved result that is consistent with the experimental data.

Doraivelu et al [70] proposed a yield function taking into account the hydrostatic stress by experimentally performing simple compression tests on sintered powder compacts. Their yield criteria depend on the value of Poisson's ratio and the relative density evolution during compression tests. Their investigation demonstrated the existence of a relationship between Poisson's ratio and relative density and suggested that the flow stress equation can be re-written in terms of Poisson's ratio and relative density. The relationship is expressed below [70];

$$\frac{\sigma_m}{\sigma_0} = \frac{(2\,{\rho_o}^2-1)^{1/2}(1-2\upsilon)}{\sqrt{3}\cdot\sqrt{3+\upsilon}(1-\rho_o)^2} \qquad 2.32$$

where, σ_m is the flow stress and σ_0 is the yield stress of the dense material.

Fleck et al.[75] developed a constitutive model based on particle deformation for porous materials with low initial relative density (ρ_o < 0.9). Their micro-mechanical approach divides the material response to loading into three different stages; stage 1, in which particle rearrangement is dominant; stage 2; in which plastic deformation is restricted only to contact regions between particles and stage 3, in which the entire particle undergoes deformation. Fleck et. al. proposed a relationship to determine the yield function for multi-axial stress states, using the contact forces between the powder particles and the yield function as described below [75];

$$f(\sigma,\rho_o) = \left(\frac{\sqrt{5}\,p}{3p_y}\right)^2 + \left(\frac{5q}{18\cdot p_y}+\frac{2}{3}\right)^2 - 1 = 0 \qquad 2.33$$

where, p_y is the yield stress of the material under hydrostatic compression and is expressed as;

$$p_y = 2.97{\rho_o}^2\,\frac{(\rho-\rho_o)}{(1-\rho_o)}\sigma_m = 0 \qquad 2.34$$

p is the hydrostatic stress, q is the effective stress and ρ is the density of the fully dense material.

Abouaf et al [76] proposed a constitutive model based on power law creep and heat conduction for powder compact densification under high temperature. Abouaf et al. found an application for their model in high temperature iso-static densification and hot pressing of porous materials. They modelled the powder compact using constitutive elasto-viscoplastic equations. They also demonstrated that the density variation in the final part is primarily due to non-homogeneous temperature fields. The power law creep model proposed by Abouaf can be written as;

$$\ddot{\varepsilon} = \ddot{\varepsilon}_r \left(\frac{\sigma}{\sigma_r}\right)^n = \mathrm{A} \cdot \sigma^n \qquad 2.35$$

where, $\ddot{\varepsilon}$ is the plastic strain, $\ddot{\varepsilon}_r$ and σ_r are the reference strain rate and reference stress, respectively. A and n are the Dron's constants and creep exponent respectively. Therefore the equivalent Mises stress for a porous material can be written as;

$$\bar{\sigma}^2 = f\, I_1^2 + 3\, c\, J_2 \qquad 2.36$$

where, c and f are experimentally determined parameters as a function of relative density and are written in terms of external pressure as [34];

$$f\,(\rho_o) = \frac{1}{9}\left[\frac{\exp\left(\frac{\ddot{\rho_o}}{\rho_o}\right)}{A \cdot P}\right]^{2/(n+1)} \qquad 2.37$$

where, P represents the external pressure applied on the porous material and $\ddot{\rho_o}$ is the densification rate determined by uniaxial compression testing of porous materials under high temperature.

2.5 Gurson's yield criterion: background and modifications

In 1977, Gurson [8] proposed a model based on a micro-mechanical approach based on a fracture mechanics perspective for materials involving significant porosity. Gurson initially developed an approximate yield criterion and flow rule for porous

ductile materials demonstrating the role of hydrostatic and deviatoric stresses in the plastic yield and void growth. Gurson developed a yield criterion based on an upper bound approach idealising a material matrix as being rigid-perfectly plastic and obeying Von-Mises yield criterion. Gurson's yield criterion for a compressible ductile porous material can be written in terms of a hydrostatic stress (p) and an internal variable for porosity (f_0) as shown below[8];

$$\Phi = f\ (p, q) = \left(\frac{q}{\sigma_0}\right)^2 + 2.f_0 \cdot\ cosh\left(\frac{3}{2}\frac{p}{\sigma_0}\right) - \left(1 + {f_0}^2\right) \qquad 2.38$$

where, q is the equivalent Von Mises stress, p the hydrostatic stress and σ_0 the flow stress of the material. These are described as follows:

$$q = \sqrt{\frac{3}{2}\ \mathrm{S{:}S}} \qquad 2.39$$

$$p == \frac{1}{3}\ Trace\ (\sigma) \qquad 2.40$$

$$\sigma_0 =\ \sigma_y + K(\bar{\varepsilon}^p)^n \qquad 2.41$$

where, n is the strain hardening exponent and k is a material parameter.

The internal variable for porosity or void volume fraction is given by

$$f_0 = \frac{V_{void}}{V_{total}} \qquad 2.42$$

where, V_{void} is the volume of the material with voids and V_{total} is the volume of the fully dense material. Figure 2.2 shows the yield surface diagram for various values of porosity with relation to hydrostatic pressure and the equivalent Von Mises stress in Gurson's equation. It can be seen that in the original Gurson's equation, when f_0=0 the yield function reduces to the Von Mises yield function. When f_0=1 the material loses its load carry capacity and represent fully void material.

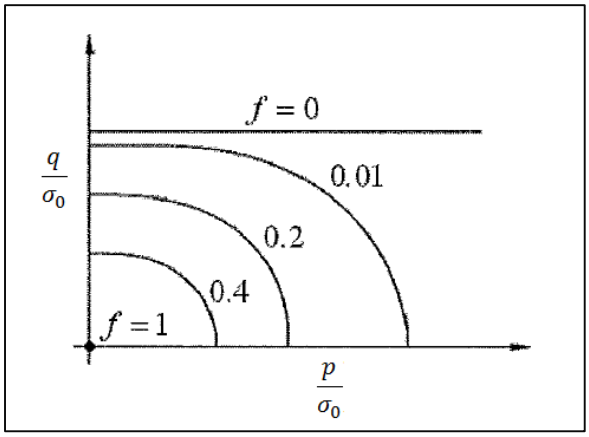

Figure 2.2: Yield surface dependence on hydrostatic tension for various values of porosity [63]

Tvergaard [77] proposed three parameters (q_1, q_2 and q_3) in the original Gurson approach which modify the approximate yield condition as follows;

$$\Phi = f\,(p,q) = \left(\frac{q}{\sigma_0}\right)^2 + 2\cdot\, q_1 \cdot f_0 \cdot\, cosh\left(\frac{q_2}{2}\frac{p}{\sigma_0}\right) - \left(1 + q_3 \cdot {f_0}^2\right) \quad 2.43$$

It may be noted that when q_1= q_2= q_3=0 the above equation reduces to the original Gurson's equation for a porous ductile material containing spherical voids. Tvergaard demonstrated that the value of these parameters depends on the material and the type of loading. Tvergaard compared the modified Gurson's equation with the original and showed that with parameters q_1=1.5, q_2=1 and q_3= ${q_1}^2$ (i.e. equation 2.43) provided results that agreed closely with those by the experimental results.

Several researchers have suggested different q_1, q_2 and q_3 parameters [78-80]. For example, Benson [80] suggested the following parameters for low carbon steel under tensile loading; $q_1 = 1.5,\ q_2 = 1.02$, and q_3= 2.5. Interestingly, Perrin and Leblond [79] showed that q_1 is a function of internal porosity (f_0) within the material. In the literature there are several values for the parameters q_1, q_2 and q_3 values for different materials and types of loading; however only parameters that are related to powder metal forming applications will be discussed in this thesis.

Equation 2.43 was further modified by Tvergaard and Needleman [10, 77] by introducing the concept of coalescence of voids;

$$\Phi = f\,(p,q) = \left(\frac{q}{\sigma_0}\right)^2 + 2\cdot q_1 \cdot f^*\cdot\, cosh\left(\frac{q_2}{2}\frac{p}{\sigma_0}\right) - \left(1 + q_3 \cdot {f^*}^2\right) \quad 2.44$$

where, f^* is the total effective void volume which is a function of void volume fraction given by;

$$f^* = \begin{cases} f^* = f & if \quad f = f_c \\ f_c + \frac{\bar{f}_F - f_c}{f_F - f_c}(f - f_c) & if \quad f_c < f < f_F \\ \bar{f}_F & if \quad f \geq f_F \end{cases} \qquad 2.45$$

where, f_c is the critical void volume fraction and f_F is final value of the void volume fraction where the material has completely lost its load carrying capacity. The function $\bar{f}_F$ is defined as;

$$\bar{f}_F = \frac{q_1 + \sqrt{{q_1}^2 - q_3}}{q_3} \qquad 2.46$$

The yield function shown in equation 2.44 is famously referred to as the GTN (Gurson-Tvergaard and Needleman) yield function.

2.5.1 Void evolution in Gurson's model

As previously indicated, Gurson's model was originally developed for fracture mechanics problems where the evolution of voids was considered critical. This has been extensively studied by various investigators [81-83]. From a fracture mechanics perspective, predicting material failure requires knowledge of void growth and the imposed stress and strain histories.

From the earlier work carried out by McClintock [83], Gurson characterised voids as having two shapes, long circular cylindrical or a spherical shape within a matrix of rigid-perfectly plastic material. This is illustrated in figure 2.3. McClintock [83] investigated the stress dependence of void growth rate and considered long cylindrical voids in a perfectly plastic solid material. A cylindrical void has an initial radius of b and the aim was to determine dependence of void growth rate Δb/b on the axial strain rate and the transverse stress state. McClintock's solution showed an exponential increase in void growth rate with equiaxial transverse stresses.

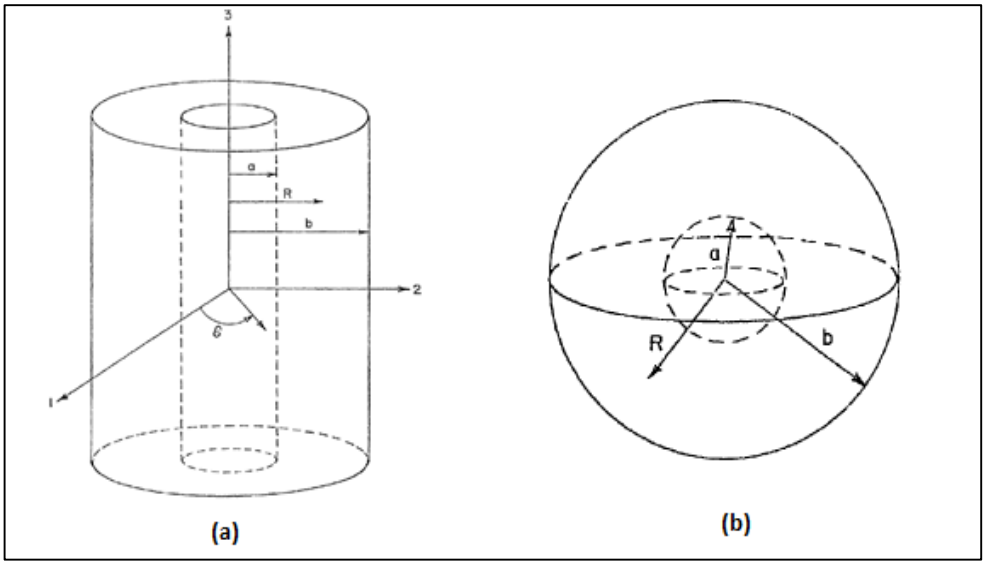

Figure 2.3: (a) Cylindrical void, and (b) spherical void within material matrix [8]

Rice and Tracey [82] obtained an approximate solution for the growth of isolated spherical voids located in an ideally plastic material matrix. They showed that at high triaxiality, which is a higher value of the ratio of hydrostatic mean stress to the material flow stress the numerical results are well approximated by the following equation;

$$\frac{R}{\ddot{\varepsilon}.R_o} \approx 0.283 \exp\left[\frac{3\,p}{2\,\sigma_0}\right] \qquad 2.47$$

where, R and R_o are the initial and final void radii before and after nucleation respectively. Additionally, Rice and Tracey found that equation 2.47 was a good approximation even at low tri-axialities.

2.5.2 Void nucleation under tension

When a porous solid material is subjected to a tensile load as shown in figure 2.4 the voids nucleate initially at imperfections in the material matrix, these voids grow due to increased tensile hydrostatic and plastic strains. Due to void nucleation and growth, the void volume fraction starts increasing as the plastic strain increases to point where the voids interact with each other. This point, when voids interact with each other, is known as the critical void volume fraction (f_c). If the plastic strain continues to increase beyond this point, the material reaches a state where local necking occurs and the voids begin to connect each other and failure of the material occurs. The connecting of voids at this state is often referred to as void coalescence. After void coalescence, a completely ductile failure of the material occurs.

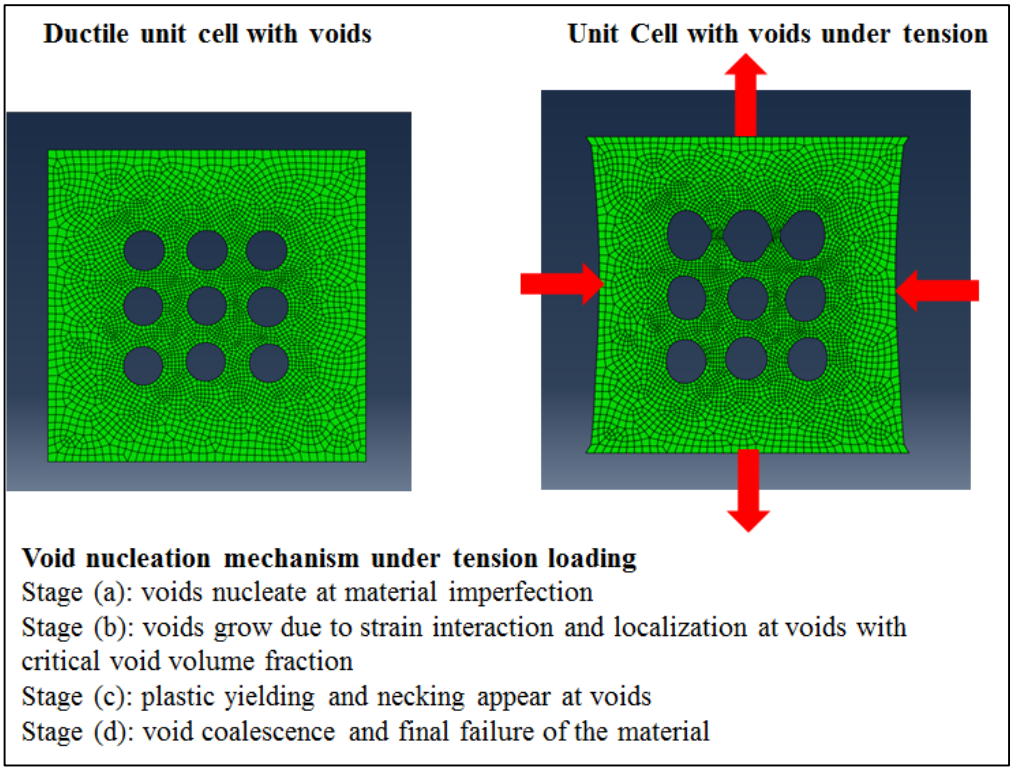

Figure 2.4: Void nucleation under tensile load

2.5.3 Void closure under compression

The mechanism of void nucleation is different when porous solid material is subjected to compressive loads as shown in figure 2.5. Under compressive loading the voids deform where imperfections in the material exists. Voids start to close due to softening of the material undergoing plastic deformation. Hydrostatic pressure or stress fields intensify and accelerate void closure. Finally the voids entirely collapse leading to volume change and densification of the material.

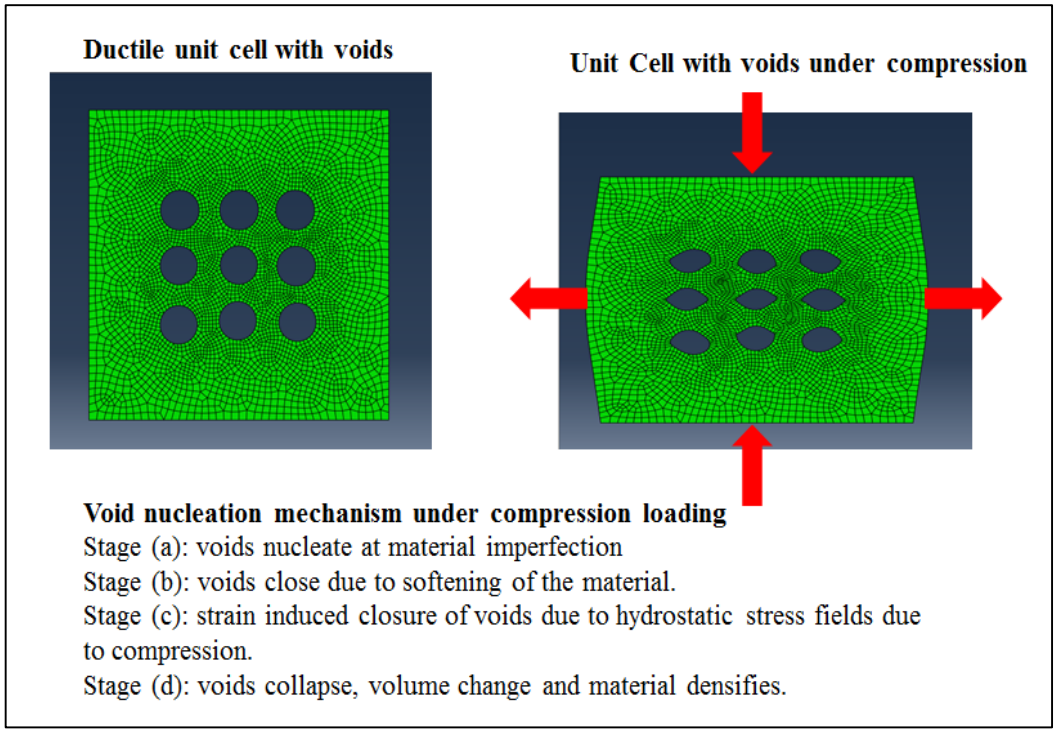

Figure 2.5: Void nucleation under compressive load

2.5.4 Plastic flow in the Gurson model

Plastic flow of porous solid material is assumed to be normal to the yield surface as shown in figure 2.2. The GTN yield function described in equation 2.44 is utilised to calculate the plastic strain void growth or closure from an initial void volume fraction and is given by;

$$\ddot{\varepsilon} = \lambda \frac{\partial f(p,q)}{\partial \sigma_{ij}} \qquad 2.48$$

where, $\ddot{\varepsilon}$ is the plastic strain in plastic porous material, σ_{ij} is the macroscopic Cauchy stress tensor and λ is a positive scalar.

If it is assumed that the material is perfectly incompressible, the rate of change in relative density can be written as;

$$\dot{\rho_0} = -\rho_0 \cdot \ddot{\varepsilon} \qquad 2.49$$

Assuming that plastic work done on porous material is equal to that of in the matrix material,

$$\rho_0 \cdot \sigma_0 \cdot \bar{\varepsilon}_m = \sigma_{ij}\ddot{\varepsilon} \qquad 2.50$$

where, $\bar{\varepsilon}_m$ is the effective plastic strain rate and σ_0 is the flow stress of the material.

2.6 Thermo-mechanical coupling

In metal forming operations such as powder forging, the effect of temperature is important, as a non-uniform temperature distribution can cause defects in the final forged product.

The billet can heat due to:

- Plastic deformation of the billet during forging,
- Frictional contact between the tool and the billet

The billet can cool due to:

- Contact between the forging tool and billet. Forging dies normally operate at a lower temperature than the billet being forged.
- Heat loss due to radiation and convection to the surroundings.

For a proper description of material behaviour during powder forging, a fully coupled thermo-mechanical analysis procedure is needed. In a fully coupled thermo-mechanical analysis, temperature is considered as an additional degree of freedom and is solved simultaneously for stress and displacement. In addition, the thermal energy balance equation is solved to calculate the temperature distribution during the analysis by considering the heat flux (amount of heat energy transferred through unit surface per unit time). Finally, the temperature dependency of the material is captured by correlating this with the material properties such as yield stress, which are defined with respect to temperature.

For a fully coupled temperature-displacement analysis, a thermal energy balance needs to be satisfied. In other words, a summation of the rate of heat entering the system and the rate of energy generated within the system needs to be equal to the rate of internal energy increase.

$$\rho\,\dot{U} = \frac{\partial}{\partial \underline{x}}\,\underline{q} + r \qquad 2.51$$

where, ρ is the density of the material. The internal energy rate per unit mass $\dot{U}$ is expressed in terms of heat capacity, c, and the temperature rate, $\dot{\theta}$, by;

$$\dot{U} = c \cdot \dot{\theta} \qquad 2.52$$

The heat flux, r, per unit volume generated within the material is assumed to drive plastic deformation only, hence;

$$r = \eta \cdot \underline{\sigma} \cdot \varepsilon^{pl} \qquad 2.53$$

where, η is known as an inelastic heat fraction, defined as the amount of overall energy dissipation which is converted into heat energy.

In coupled temperature-displacement analysis, heat transfer with the material is described by conduction and follows the Fourier law of heat conduction as illustrated below;

$$\underline{q} = -K \cdot \frac{\partial \theta}{\partial \underline{x}} \qquad 2.54$$

Where, K is thermal conductivity of the material, the negative sign implies that the heat always flows in direction of decreasing temperature. The value of thermal conductivity is usually defined as a function of temperature for better accuracy of computation.

Heat convection is generally defined as a boundary condition applied to a surface that is directly exposed to the surroundings. The convective heat transfer equation is shown below;

$$q_{cov} = -h \cdot (\theta - \theta_0) \qquad 2.55$$

where, h is the film transfer coefficient and its value depends on the exposed surroundings.

Surrounding medium	Transmission surface	Film coefficient (W/ m^2.k)
Water	Cast iron	7.9
Water	Low carbon steel	11.3
Air	Cast iron	5.7
Air	Low carbon steel	7.9
Air	Titanium	10

Table 2: Typical film coefficient values for various materials [84]

The heat flux due to radiation loss to the environment is governed by the following equation;

$$q_{rad} = -A \cdot [(\theta - \theta_z)^4 - (\theta_0 - \theta_z)^4] \quad 2.56$$

where, $\theta_0$and $\theta_z$are the ambient and absolute zero temperatures respectively. A is the known as the radiation constant and is defined as;

$$A = \varepsilon^s \cdot \sigma^{S-B} \quad 2.57$$

where, $\varepsilon^s$is the emissivity of the surface and σ^{S-B} is the Stefan-Boltzmann constant. It must be noted that loss of heat energy by conduction and convection is far greater than heat loss by radiation in forging; therefore heat loss by radiation is often neglected.

2.7 Frictional forces

In a powder forging process, the desired shape changes are obtained by pressing the material between the tools, which are much stiffer than the material being deformed. Since there is a large difference between the deformability of the tool and the powder compact, relative movement arises between them at the contact surface. The magnitude of this relative movement depends on the geometry, loading type and frictional conditions at the interface. It is important to include frictional conditions in the FEM of powder forging as it plays a crucial role in the estimation of relative density [63].

Though there are several models that are used to describe frictional condition [85, 86], two models are prominent in metal forming simulation, Coulomb's friction model and the shear friction model.

2.7.1 Coulomb friction model

Coulomb's frictional law is widely used in engineering to model frictional interactions. The governing equation for Coulomb friction;

$$\tau_f = \mu \cdot \sigma_n \qquad 2.58$$

where, τ_f is the tangential frictional stress, μ is the frictional coefficient which is independent of the apparent area of contact, and σ_n is the normal stress or interface pressure acting on the surface. Despite the popularity of using Coulomb's law of friction in metal forming analysis, its accuracy is limited depending on the circumstances during forging. For example, an increase in coefficient of friction is reported for lighter deformation loads [85], but contrary to this a decrease in friction coefficient is noted under high loading conditions [86], where the true area of contact is closer in magnitude to the apparent area of contact occurring during plastic deformation of a material.

The coefficient of friction μ depends on the type of lubricant being used in the metal forming process. Table 3 shows coefficients of friction for common lubricants used in hot metal forging.

Lubricant	μ
Dry or no lubricant	0.33, 0.35, 0.38
Furnace oil	0.10, 0.18, 0.12
Graphite in oil	0.065, 0.08, 0.09
Graphite in water	0.11, 0.10, 0.13

Table 3: Coefficient of friction for various die lubricants [87]

In powder forging, the interface pressure σ_n can be many times higher than the yield stress of the material, thus the linear relationship described in equation 2.58 may not be suitable at high contact pressure, where shear stress cannot exceed the shear yield

strength of the material. In such cases, the Coulomb friction law above does not apply, and a shear frictional model, proposed by Orowan [88] can be utilised.

2.7.2 Shear friction

In a shear friction model, the frictional stress at the tool and billet interface is in direct proportion to the interfacial shear stress in the deforming material. The governing equations for a shear frictional model are expressed as [88];

$$\tau_f = m \cdot k = m \cdot \frac{\sigma_s}{\sqrt{3}} \qquad 2.59$$

where, τ_f is the frictional stress, m is the frictional factor, k is the shear yield stress of the material (measured in torsion) being deformed and σ_s is the true stress.

In a shear frictional model, it must be noted that when the roughness of the powder compact-die surface interface and the lubrication conditions are known, the frictional stress does not depend on the current stress state.

2.8 Summary

In this chapter, material models developed by different researchers have been reviewed. The literature review shows that several mathematical approximations exist for modelling a powder forging process and these are summarised in the table below;

Model/ researchers	**Process/ application**	**Modelling aspects**
Kuhn and Downey [27]	P/M compaction	Proposed a yield criterion for porous materials by taking the effect of hydrostatic stress on yielding into consideration.
Green [68]	P/M compaction	Proposed a yield criterion based on elastic-plastic analysis assuming material isotropy with distributed voids or cracks in material matrix.
Doaraivelu et. al. [70]	P/M/sinter-forge	Proposed a new yield function taking into account the hydrostatic stress. Yield criteria depend on the value of Poisson's ratio and the relative density evolution during compression.
Shima and Oyane [69]	P/M compaction, Sintering, Soil mechanics	Developed a yield criterion for porous metallic structures fabricated by solid state sintering. This model has been widely applied for powder compaction at both low and high temperatures. However, it underestimates the relative density at low density regions during deformation.

Kuhn and McMeeking [89], Abouaf et. al. [76]	Hot isostatic pressing (HIP), hot pressing.	Developed a model for pressure assisted densification of metal powder compacts based on power-law creep near the inter-particle contacts. Abouaf et al. have found an application for their model in high temperature iso-static densification and hot pressing of porous materials.
Gurson [8]	Fracture mechanics, powder compaction, hot pressing, powder forging, hot coining, HIP, sinter-forge.	Proposed a yield criterion and flow rule for porous ductile materials demonstrating the role of hydrostatic and deviatoric stresses in during plastic yield and void growth.

Table 4: Summary of material models investigated by various researchers

Powder forging of porous materials and densification behaviour is complex and although it has been theoretically studied for over 40 years it is still a major research focus in the area of powder metallurgy. A literature review found several models that are available to predict the relative densities during powder compact forging. A few of these models have been used for powder forging applications, but none of them has been used either in compaction or forging of titanium powder. As one of the prerequisites of this study was to determine a model that is simple enough to be used in industrial simulations, many of them required several material parameters that required determination by physical testing and modifications to the implementation scheme, such as in the yield criterion, which could only be done through programming.

Gurson was one of the earliest researchers to study the deformation behaviour of ductile materials with significant porosity using a micro-mechanical approach; his work serves as the cornerstone in modelling powder metal forming. The Gurson and Gurson-Tvergaard models have been previously used in powder compaction, sinter forging and hot isostatic processing. The Gurson and Gurson-Tvergaard models were chosen in this study for their simplicity and recognition in the field of powder

metallurgy. In several studies the model has been found to be moderately successful in describing densification and deformation behaviour with good results. The original Gurson model is readily available in Abaqus software and provides an insight into general trends of densification with parameter adjustments for different powder materials. However, no literature was found on the use of the Gurson-Tvergaard model in the study of densification behaviour of titanium powder compacts at a low starting relative density. Also it is of interest to determine the material parameters that are more specific to titanium powder compacts used in the present process. Furthermore it is of interest to see whether the experimentally determined parameters had any significance in the improvement of simulated results when compared with the actual density measurements.

3 Modelling in Abaqus ™

3.1 Introduction

Abaqus is FEA software that offers a solution to both routine and sophisticated engineering problems covering a vast spectrum of engineering and industrial applications. Abaqus software is suitable for metal forming simulations where large deformation of the material needs to be analysed. The software also offers wide flexibility in modelling and implementation of new material models. The commercial versions of Abaqus software can be classified as;

- Abaqus/standard: an implicit integration for general problems
- Abaqus/explicit: an explicit integration based finite element program

The modelling process in Abaqus software mainly consists of six steps.

- Geometric modelling
- Material definition
- Boundary definition (Geometric and thermal conditions)
- Contact interactions (friction, heat transfer)
- Meshing
- Solver and results

3.1.1 Geometric modelling

In Abaqus, the geometry can be modelled by defining the co-ordinates or it can be directly imported as a model from any CAD software. Once the geometry is defined the models are assembled according to the requirements of the problem. For example, figure 3.1 shows an Abaqus model of a die and powder compact assembly for disc forging.

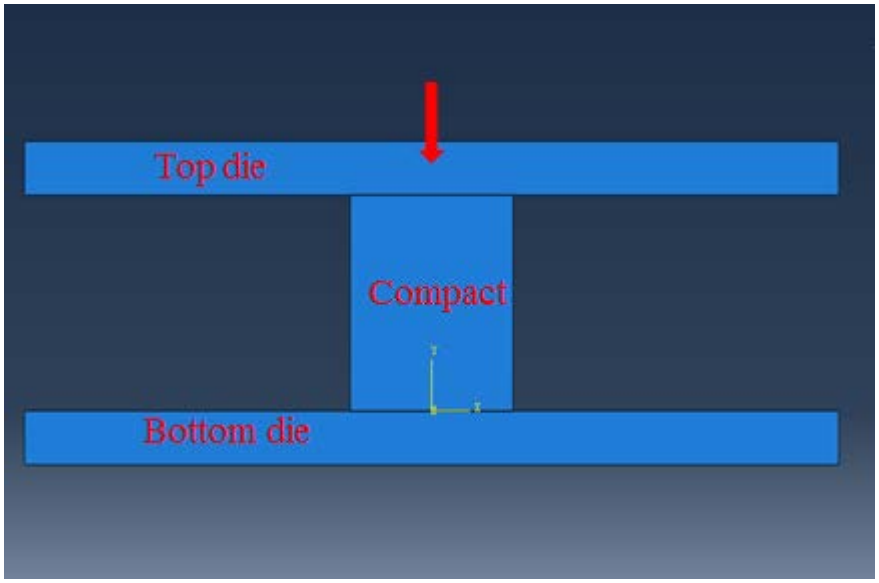

Figure 3.1: Compact-die assembly in Abaqus

It is worthwhile to mention that Abaqus does not follow any unit conventions; however it is important to follow one unit convention throughout the simulations. For example, if the geometry is defined in meters, then a boundary condition such as top die velocity, should also be specified in meters/sec.

3.1.2 Material definition

In Abaqus, material properties can be assigned to both tool and billet. The tool can be modelled as rigid or elastic depending on the analysis type. Typical material properties assigned to tooling include Young's modulus, Poisson's ratio, density and specific heat. In metal forming simulation, for reliable results it is important to define plastic properties such as the flow stress or yield stress of the material being deformed.

3.1.3 Boundary and initial conditions

Boundary conditions are used to define the values of the basic solution variables. The solution variables include displacement, rotation, temperature, velocity, acceleration etc. Boundary conditions are usually specified within the analysis step. Boundary conditions can also be used to define any constraints, such as for example, the prescribed distance moved by a top die to forge a billet. All the other degrees of freedom must be equated to zero.

Initial conditions are used to define prescribed conditions in the initial analysis step. Predefined conditions include temperature, field variables, an equivalent pressure state, mass flow rate etc. In metal forming simulation, predefined conditions are used to define the initial temperature of the billet and the dies. A value for the initial condition, such as temperature can be directly entered and defined on the geometry or can be imported from another step or analysis.

3.1.4 Contact interactions

A contact algorithm allows the interaction of geometrical objects with each other to be defined during the simulation. In Abaqus/standard sliding contact can be defined between two surfaces in contact with each other. A sliding contact algorithm can be used to model the interaction between a rigid and a deformable body.

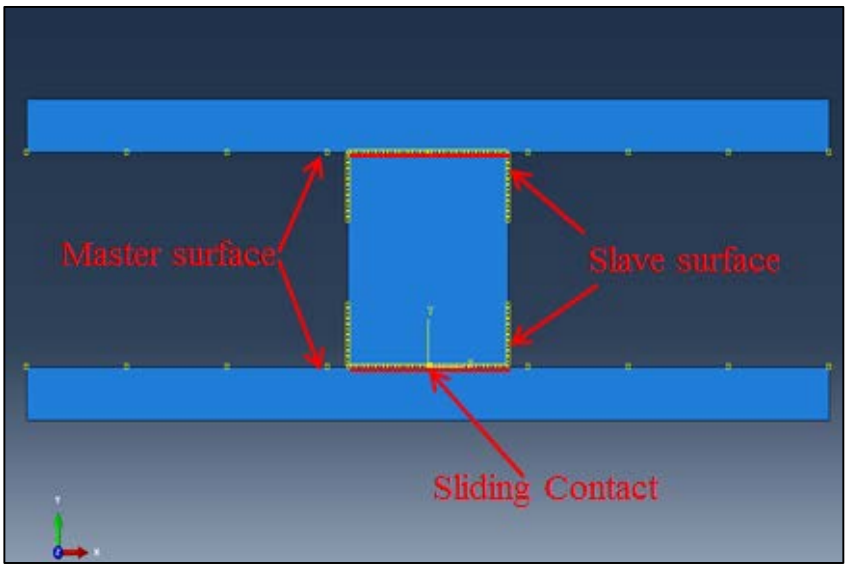

Figure 3.2: Contact interaction between the tool and the compact

In Abaqus, a contact algorithm is applied to model the frictional contact, non-penetration conditions and heat transfer interactions.

- Frictional contact: both normal and tangential friction can be defined between the surface pairs in contact. For example, for defining Coulomb friction, the frictional coefficient value is specified between the contact pairs.
- Non-penetration conditions: In multi-body dynamic simulations, when two bodies or objects are in contact, there exists a possibility that one object might

penetrate into the other. To avoid this, a master-slave surface approach is adopted, where the non-penetration condition is enforced by preventing the nodes of one contact surface (master surface) from penetrating the other (slave surface) [90]. In metal forming simulations, a rigid die is generally defined as a master surface and the deformable billet as a slave surface.

- Heat transfer: Heat transfer interactions or thermal contact properties between two geometries in contact can be defined by specifying the interfacial heat transfer coefficients. In Abaqus, this is defined by a function known as "*gap-conductance*". The gap conductance can be enforced in the model either as a function of clearance or as a function of contact pressure.

3.1.5 Step definition

In Abaqus, before selecting the boundary and loading conditions, an analysis step needs to be defined. An analysis step in Abaqus assigns the type of FEM analysis procedure. For example, coupled-temperature-displacement analysis, explicit dynamic temperature-displacement analysis etc. Once the step is selected, different boundary and contact conditions are defined in each step. Any number of steps can be defined simultaneously depending on the problem requirements. However, it is worth mentioning that certain elements can only be applied for certain types of analysis, thus elements and the analysis types should correlated. In the initial step, initial conditions such as temperature are assigned and the analysis calculates the heat transfer in the subsequent steps.

3.1.6 Finite element mesh

In the finite element method, a geometric model forms the basis for defining the finite element mesh. The main purpose of geometric modelling (discussed in section 3.1.1) is to display objects whose geometry has been defined. In Abaqus, any number of geometries or objects can be assembled and meshed. The type of mesh algorithm, the mesh density and quality of the mesh influences the accuracy of the results. The geometric model can be associated with the mesh via physical attributes such as element properties, material properties, loads and boundary conditions.

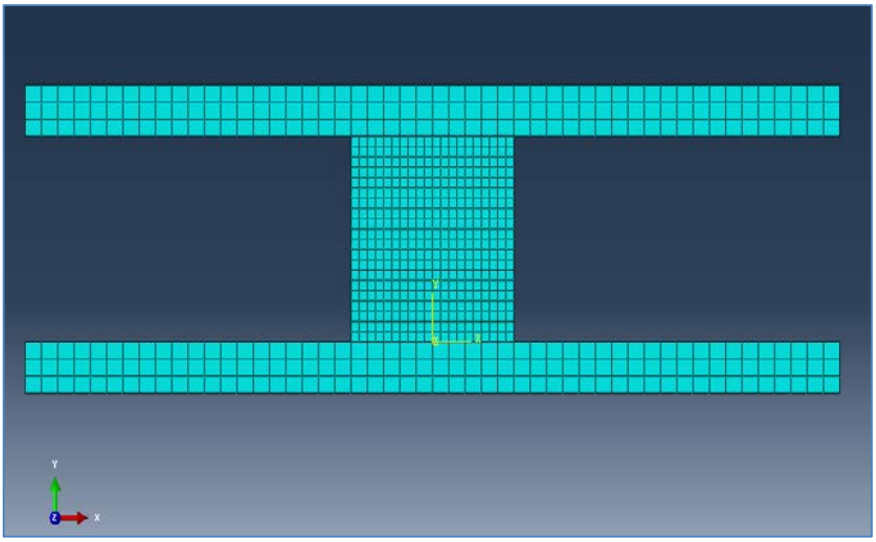

Figure 3.3: Finite element mesh associated with the geometric model

The boundary conditions, initial condition and loads can be applied on elements, nodes or a set of nodes and elements. For metal forming simulations, such as powder forging which involves large deformations, it is important to select appropriate meshing algorithms for worthwhile and realistic results. Abaqus includes numerous element types for different applications; however brick/quadrilateral and triangular/tetrahedral are the most commonly used solid elements for metal forming simulations. Figure 3.4 shows triangular and quadrilateral elements used in Abaqus.

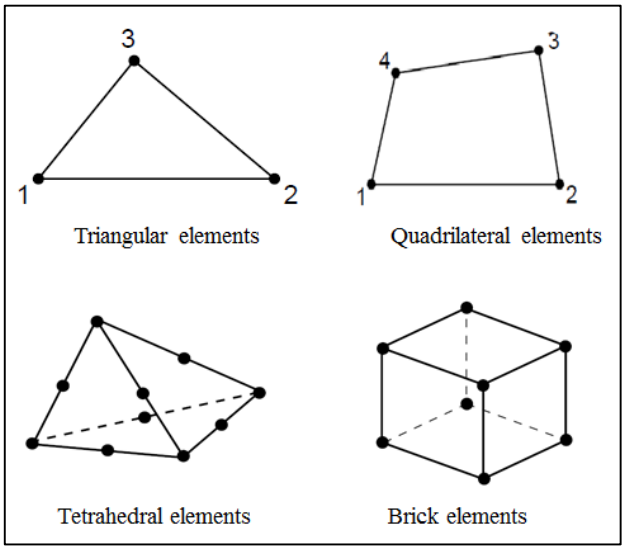

Figure 3.4: Solid element types [91]

Both quadrilateral and triangular elements are available both in two dimensions as well as in three dimensions as shown in figure 3.4.

Degrees of freedom such as displacement are calculated at the nodes of an element. The displacement at any point within the element is obtained by interpolating from two nodal displacements. In some cases, the interpolation is carried out depending on the number of nodes present in each element. Both first and second order elements are available depending on the accuracy requirements of an analysis [91]. First order elements are easy to converge and less solution time is needed for an analysis. Second order elements are highly accurate especially in Abaqus/standard and can be used for problems involving complex boundary and contact conditions. From experience, first order triangular elements are exceedingly stiff and display slow convergence with mesh refinements. However, in problems that involve complex geometry a fine triangular mesh can be favourable.

3.1.7 Solver and viewing results

In Abaqus, two types of analysis can be performed depending on the integration of the stiffness equations;

- Abaqus/Explicit: An explicit analysis performs the incremental procedure and at the end of each increment it updates the stiffness matrix based on geometric or material changes. The next incremental load is applied to the newly constructed stiffness matrix. The method is more desirable for metal forming analysis due to the fact that the stiffness matrix is updated with the deformation geometry [92].
- Abaqus/Standard: Abaqus standard analysis relies on the implicit method of integration and in many ways is similar to the explicit method with the addition that after the end of each increment the analysis does a Newton-Raphson iteration to enforce equilibrium of the internal structural forces with the externally applied loads [91, 92]. The only drawback of this type of analysis is that, during Newton-Raphson iterations the stiffness matrix must be updated and restructured at each iteration, which could be computationally costly.

3.2 Non-linear problems in Abaqus

The term non-linearity refers to a solution state in an FEM analysis, when the input data is no longer proportional to the output data. In metal forming problems non-linearity can arise from various sources such as non-linear material behaviour, geometric non-linearity or non-linearity due to initial or boundary conditions.

3.2.1 Non-linear material behaviour

Material non-linearity arises when the material exhibits non-linear stress-strain behaviour. In linear analysis, the stress-strain relationship is defined by the Young's modulus, but in non-linear analysis the Young's modulus only describes the initial elastic part of the overall material behaviour. Non-linear analysis is used, for example, for the post yielding plastic deformation of a material. Common types of non-linear material behaviour include nonlinear elastic, elasto-plastic, visco-plastic etc. Figure 3.5 shows typical non-linear elasto-plastic stress-strain characteristics under tensional load.

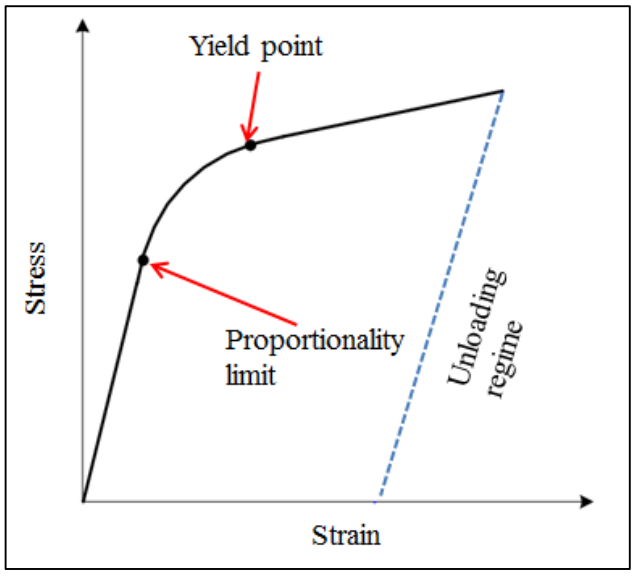

Figure 3.5: Stress-strain relationship curve

For an accurate description of a material in plastic deformation problems it is also common to include the work hardening behaviour of a material. Common hardening behaviour in Abaqus analysis includes isotropic, kinematic and Johnson-Cook depending on the nature of a problem. Also for coupled thermo-mechanical analysis, a temperature dependent thermal conductivity can induce non-linearity.

3.2.2 Geometric non-linearity

Geometric non-linearity in metal forming analyses is usually associated with large deformations. If a continuum in the analysis undergoes large finite deformation, the load-displacement relationship tends to be non-linear. Figure 3.6 illustrates a non-linear load displacement curve for a material undergoing large deformation. When the applied load is at a lower level, a linear relationship with displacement can be clearly seen, but after a certain point the stiffness will change with deformation, thus producing non-linearity.

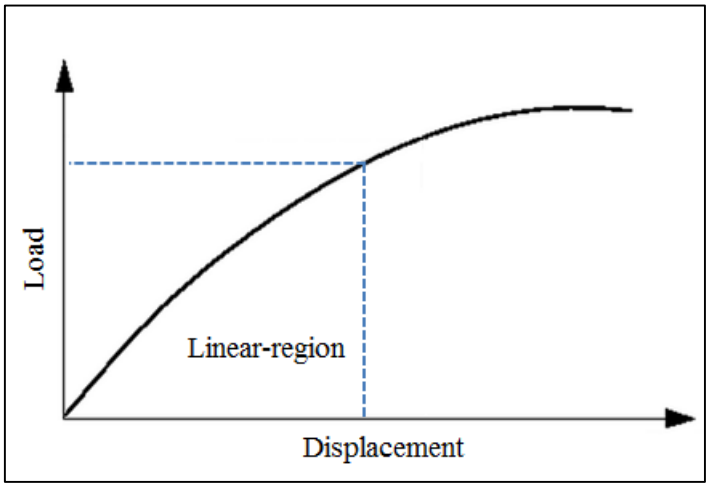

Figure 3.6: Non-linear load-displacement curve

In problems involving geometric non-linearity, the solution cannot be obtained by solving a single set of equations, as in the case of linear problems. In such scenarios, the final solution can be obtained by incremental load application using numerical methods.

3.2.3 Non-linearity due to initial or boundary conditions

Many problems in Abaqus involving contact mechanics include a boundary condition that changes during deformation, thus non-linearity is induced. In boundary condition induced non-linearity the stiffness of the object or assembly (set of assemblies) may change significantly when two or more parts are either in contact or are separated from the initial contact. For example, structures consisting of bolted joints or a deforming billet in a forging die.

In Abaqus/standard, the Newton-Raphson method is adopted to obtain solutions for non-linear problems. Abaqus/standard discretizes the simulation into a number of load increments and calculates the approximate equilibrium configuration at the end of each load increment. Several iterations are required in Abaqus/standard to find the exact or approximate solution for a non-linear problem. Hence, it can be said that Abaqus/standard combines incremental and iterative stages to solve a given non-linear problem.

3.3 Mesh distortion control

In many metal forming analyses, the material in the analysis undergoes very large deformation. These large deformations distort the finite element mesh to an extent that the mesh is unable to provide accurate results or the analysis fails to converge for numerical reasons. In such situations, an adaptive meshing technique is used to control the distortion of the mesh. Both Abaqus standard and explicit contain an adaptive meshing capability, however the re-meshing technique in Abaqus/explicit is more robust. Figure 3.7 shows a deformed mesh during an extrusion simulation with and without distortion control.

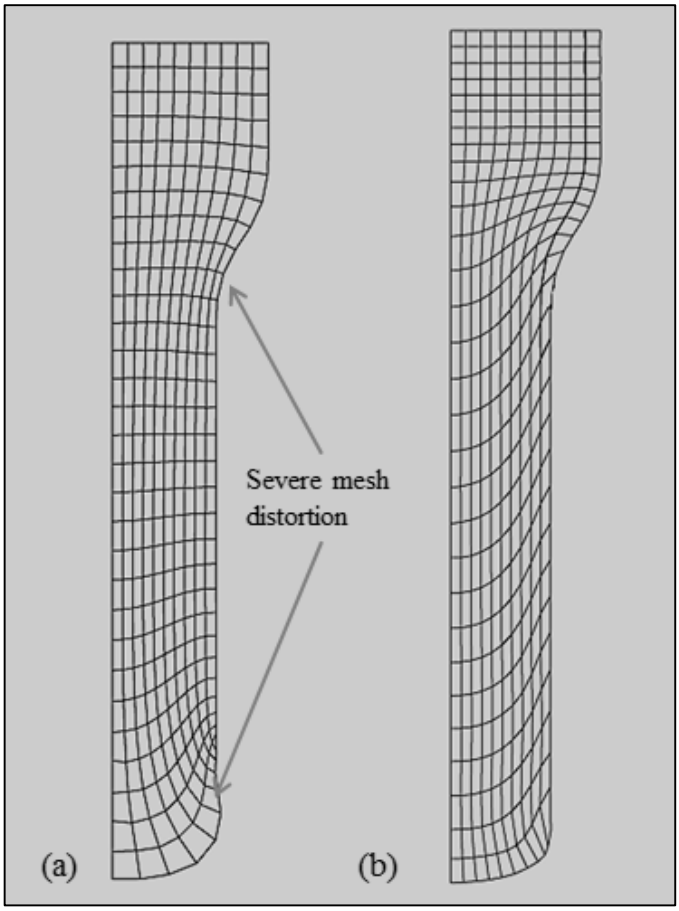

Figure 3.7: (a) mesh without distortion control; (b) mesh with distortion control [91]

In the finite element method there are different meshing schemes that are used to control the mesh distortion. These are Lagrangian mesh, Eulerian mesh and Arbitrary Lagrangian- Eulerian mesh. The major difference between the three meshing methods can be described by the motion of the mesh with respect to the deforming material.

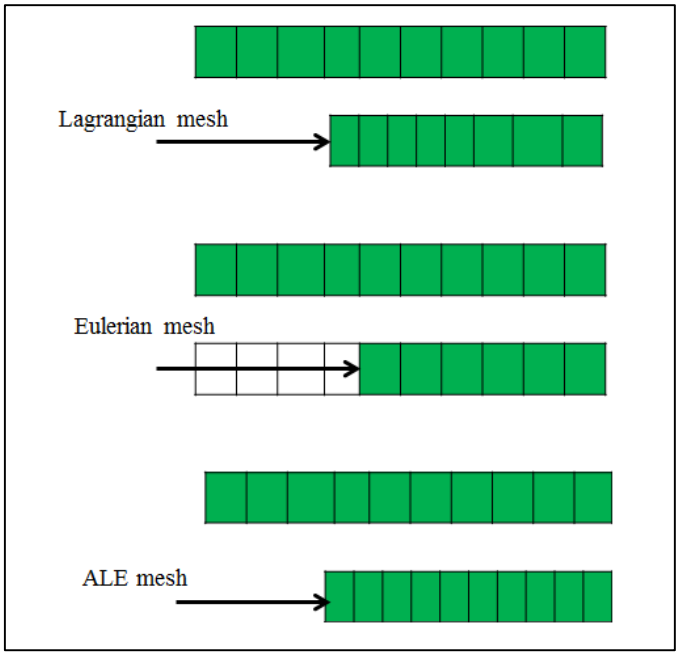

Figure 3.8: Meshing techniques [91]

- In a pure Lagrangian mesh, the elements and the nodes move exactly with the material point during deformation. The advantage of this meshing technique is that it is easy to track the surface regions and associate boundary or contact conditions to the mesh. This meshing technique is suitable for metal forming analysis; however the mesh can be severely distorted during deformation with a large strain rate.
- In a Eulerian mesh, the elements and the nodes remain fixed while the material flows though the meshed region [93]. This meshing techniques finds many applications in computational fluid dynamics analysis, however applications in metal forming are limited.
- Arbitrary Lagrangian-Eulerian (ALE) mesh; the ALE meshing method combines the advantages of both Lagrangian and Eulerian meshing and is found to be accurate in many metal forming analyses [94-96]. In ALE meshing, the motion of the mesh and the material is independent at most places in the material; however the mesh is only constrained within the material being deformed.

3.4 Modelling powder forging in Abaqus

Abaqus is a powerful numerical tool for aiding product and process design. In this section we will discuss some of the key parameters involved in powder forging and the method used to simulate them in the present work through Abaqus software. As mentioned previously, Abaqus is a finite element program used to solve coupled thermo-mechanical problems. It can also be used to simulate powder forging. The program can solve complex non-linear problems that involve heat transfer, a temperature distribution and material flow. The program provides useful information such as deformation patterns, stress and strain distributions that are helpful in assessing the performance of a die and a particular preform design.

In Abaqus software several porous material models are available that can be used for simulating a powder forming process such as powder compaction. For example, a modified Drucker-Prager cap model is favourable to predict the failure criteria in powder compacts [97]. The finite element analysis procedure in this research adopts an Abaqus built-in porous metal plasticity criterion.

Abaqus has the advantage of greater flexibility in material modelling and simplicity of implementation makes it the preferred software in the powder metallurgical field. However, the material parameters need to be calibrated for useful results. Some of the other popular software available for forging simulations are Deform 2D/3D, Q-form and transvalor. Deform 2D/3D has an in-built porous material model which is based on the Shima and Oyane yield criterion [98, 99].

3.5 Material property definition

For simulating powder forging it is important to define the property of the material for accurate results. The material property for the tooling material is obtained from the literature. The tooling material used in the experiments and the simulation is H13 tool steel. The material properties defined in the simulation are tabulated as below.

Young's modulus	2.1 E+011 N/m^2
Poisson's ratio	0.28
Density	7.8 g/cc
Specific heat	0.468 J/g °C
Thermal conductivity	24.3 W/m^2. K
Expansion coefficient alpha	1.2 E-005 /° C

Figure 3.9: Mechanical and thermal properties of the tooling material [100]

The material data for the commercially pure HDH titanium was obtained by Gleeble testing. The method adopted to obtain the flow stress curves by Gleeble testing is described in the following section.

3.6 Gleeble hot deformation testing

Gleeble compression testing is a method used to determine the flow stress of a material under investigation. The compression tests were performed at Harbin Institute of Technology, China using their Gleeble 1500 thermo-mechanical simulator as shown in figure 3.10. The test sample was mounted in between two jaws whose movements were computer controlled. The sample was heated by a resistance heater and the temperature was monitored using welded thermocouples. Liquid graphite was used to reduce the interfacial friction between the sample and the jaws. The strain rate was determined using strain gauges mounted on the sample.

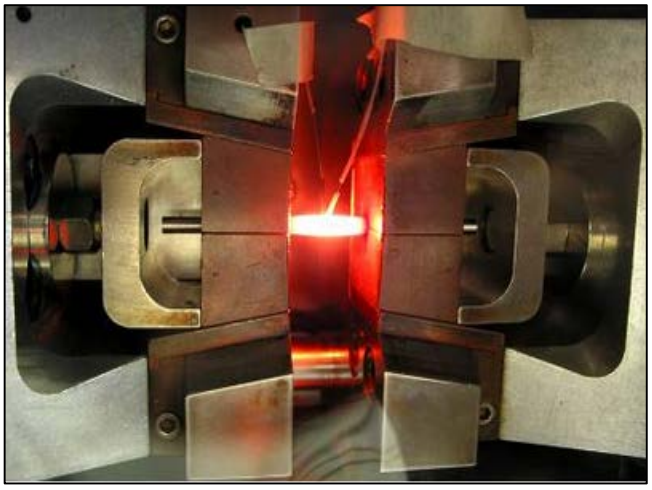

Figure 3.10: Gleeble 1500 thermo-mechanical simulator

The samples were prepared by powder compaction and induction sintering at different condition as described in the literature [101]. The compacts were cut, stress relieved and polished before testing in China. Four commercially pure titanium samples with a dimension of Ø8mm×12mm were cut (using a wire cutter) from each powder compact (dimension Ø42mm×40 mm) to maintain consistency. The bulk relative density (ratio of actual density to the theoretical density) of each sample was measured and the average relative density was found to be 0.78. The tests were carried out at three different strain rates (i.e. 1 s^{-1}, 0.1 s^{-1}, 0.01 s^{-1}) and at three different initial temperatures (i.e. 1200 ºC, 1100 ºC, 1000 ºC). Figure 3.11 shows the flow stress data for HDH titanium obtained after Gleeble compression testing.

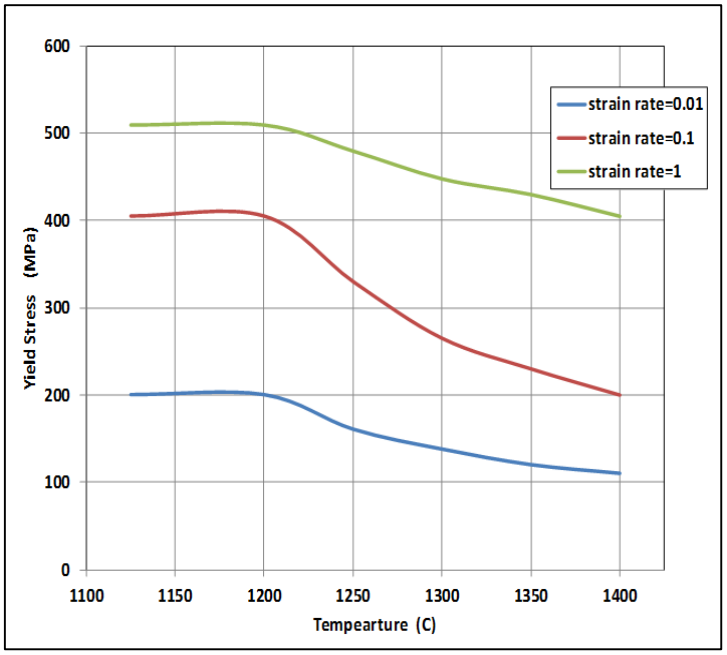

Figure 3.11: Flow stress for HDH-titanium obtained by compression tests

The data obtained by Gleeble testing was defined in the Abaqus material plasticity option as a strain and temperature dependent plastic material. Most of the material property data was obtained by Gleeble testing; however some of the property information was obtained from the literature. Table 5 summarises some important material properties that are used in the simulation;

Parameters				
Temp.° C	Conductivity (W/m^K)	Temp. ° C	Modulus of elasticity (N/m^2)	Poisson's ratio
700	20.205	900	135E+009	0.32
800	23.078	1000	130E+009	0.33
900	25.633	1100	118E+009	0.34
1000	26.749	1200	110E+009	0.35
1100	31.827	Temp. ° C	Specific heat (J/Kg-K)	
1200	33.129	700	855.01	
Temp. ° C	Expansion Coeff. (/° C)	800	925.86	
800	7.7E-005	900	1045.08	
900	7.8E-005	1000	1116.8	
1000	7.9E-005	1100	1618.59	
1100	7.95E-005	1200	1098.55	
1200	7.97E-005			

Table 5: Material properties of an HDH-titanium powder compact

3.7 The Gurson model in Abaqus

In Abaqus/ standard the Gurson model is incorporated as a porous metal plasticity option for modelling materials that exhibit void nucleation and growth. It can also be used to model powder metal forming processes with an initial relative density. Although the model was originally intended to be used for material with a high relative density greater than 0.9, several recent publications [5, 12, 43, 102] have highlighted its application for materials with lower initial relative density. Previously several researchers implemented this model for lower density processes such as ECAP and powder compaction.

The Gurson model available in Abaqus (both implicit/explicit) is strain-controlled taking void nucleation, void closure and void coalescence into consideration. The Gurson model is available in both Abaqus/standard and Abaqus/explicit. However, Abaqus implicit does not include a void coalescence function (not relevant for powder metal forming simulations), meanwhile Abaqus explicit code does not include relative density calculations that are required in powder metallurgical applications. Several, researchers have overcome this problem by writing a VUMAT (vectorized user material model) subroutine in FORTRAN enabling a relative density distribution with the explicit code. The explicit code allows for simulation of complex geometrical problems with advanced meshing capabilities that are not available in Abaqus implicit.

From a numerical perspective, some published work [103, 104] has tried to integrate the Gurson model into a finite element program. The integration allows for complex analysis involving different load configurations and eventually a prediction of void nucleation or density distribution. The numerical integration of the Gurson model has been historically referred to as computationally intensive [105], thus numerical aspects of the model integration play a crucial role in the efficiency of the finite element calculations. The numerical scheme to implement the Gurson model in Abaqus was first introduced by Aravas [103] using implicit integration. The Aravas integration scheme includes two steps; i.e. an elastic prediction and a plastic correction.

The principal strain is divided into elastic and plastic parts;

$$\dot{\varepsilon} = \dot{\varepsilon}_{el} + \dot{\varepsilon}_{pl} \quad 3.1$$

The plastic strain increment is further divided into hydrostatic and deviatoric components and is given as;

$$\varepsilon_{pl} = \frac{1}{3}\Delta\ddot{\varepsilon}_p + \frac{3}{2\bar{\varepsilon}_m}\Delta\ddot{\varepsilon}_q \quad 3.2$$

$$\text{where,} \quad \Delta\ddot{\varepsilon}_p = \ddot{\lambda}\frac{\partial f(p,q)}{\partial p} \quad 3.3$$

and

$$\Delta\ddot{\varepsilon}_q = -\lambda\frac{\partial f(p,q)}{\partial q} \quad 3.4$$

The volume fraction V_f and the equivalent plastic strain of the material is treated as two internal state variables; i.e.H^1 and H^2. The implementation procedure is as follows;

1. The first step begins with initialisation of the variables at time t=0; σ_t, ε_t, H_t^1 and $\Delta\varepsilon_{t+\Delta t}$. Where, H_t^1 is a state variable and $\Delta\varepsilon_{t+\Delta t}$ is the strain increment.
2. The elastic predictor is calculated by assuming that the strain increment is purely elastic, i.e;

   $$\sigma_{t+\Delta t}^1 = \sigma_t + C_e \quad 3.5$$

   where, $\sigma_{t+\Delta t}^1$ is the next elastic stress increment and C_e is the isotropic linear elastic fourth order stiffness tensor.
3. The hydrostatic stresses are determined, i.e.:

   $$p_{t+\Delta t}^1 = -\frac{1}{3}\sigma_{t+\Delta t}^1 : 1 \quad 3.6$$

4. The equivalent Von Mises stresses are determined, i.e.:

   $$q_{t+\Delta t}^1 = \sqrt{\frac{3}{2}\, S_{t+\Delta t}^1 : S_{t+\Delta t}^1} \quad 3.7$$

5. The yield surface is calculated. i.e;

$$\Phi^1_{t+\Delta t} = \Phi^1_{t+\Delta t}(\sigma^1_{t+\Delta t}, H^1_t) = \Phi^1_{t+\Delta t}\,(p^1_{t+\Delta t}, q^1_{t+\Delta t}, H^1_t) \qquad 3.8$$

If $\Phi^1_{t+\Delta t} \leq 0$, the current state of the material is elastic, thus $\sigma_{t+\Delta t} = \sigma^1_{t+\Delta t}$; the iteration ends and solution is obtained as in step 7.

If $\Phi^1_{t+\Delta t} \geq 0$, the current state of the material is plastic, hence iteration proceeds to step 6.

6. A Newton-Raphson iteration is performed to determine the plastic correction until the following non-linear equations are satisfied.

$$g_1 = \Delta\varepsilon_p{}^{s+1}\frac{\partial \Phi}{\partial q} + \Delta\varepsilon_q{}^{s+1}\frac{\partial \Phi}{\partial p} = 0 \qquad 3.9$$

$$g_2 = \Phi(p^{s+1}, q^{s+1}, H_t^{1(s+1)}) = 0 \qquad 3.10$$

The flow rule and the condition that the above stress states must be within the yield surface curve must be satisfied. At the same time a consistency condition must also be satisfied. i.e;

$$\sigma_0{}^{s+1} = \frac{d\sigma_0}{d\bar{\varepsilon_p}} \cdot \bar{\varepsilon_p}{}^{s+1} \qquad 3.11$$

The Newton-Raphson iteration is continued until $|g_1|$ and $|g_2|$ is less than the specified tolerance for convergence is achieved. Once convergence is achieved the following solution matrices are updated as in step 7.

7. Update the p, q and H^1 i.e;

$$p = p^1 + K \cdot \Delta\varepsilon_p \qquad 3.12$$

$$q = q^1 - 3G \cdot \Delta\varepsilon_p \qquad 3.13$$

where, G is the shear modulus of the material and K is the bulk modulus. Once the p and q are calculated the stress state and plastic strain of the material is calculated by the following equation;

$$\sigma = -p \cdot I + S \qquad 3.14$$

$$\overline{\Delta\varepsilon_p} = \frac{-p.\Delta\varepsilon_p + q.\Delta\varepsilon_q}{(1-f).\sigma_0} \qquad 3.15$$

Once the plastic strain increment is determined, it is possible to calculate the volumetric strain increment and finally the relative density.

3.8 State of the art of the Gurson model in powder metal forming applications

As introduced in the previous chapter, the Gurson model was originally developed for ductile materials with a considerable amount of porosity undergoing ductile fracture. In the original work, it was acknowledged that the model can be applied to sintered powder compacts assuming that the powder contains approximately equi-axed voids. Gurson and Buno [7] developed a procedure to simulate a powder compaction process for intermediate initial relative density between 0.75 and 0.90 and showed that it closely matched the experimental results. The Gurson model has been used by several researchers [34] in predicting the densification behaviour of titanium alloy powder by hot isostatic pressing. Kaushik et. al. [5] applied Gurson' s model to simulate densification of powder material via Equal Channel Angular Extrusion (ECAE). They also compared the results with the Duva and Crow model [106] which showed promising results.

Only a few investigations, to predict the densification of forged powder compact products, have been made using the Gurson model. For example, Biner and Spitzig [107] studied the consolidation of iron powder compacts under hydrostatic pressure. They altered the original Gurson model by considering internal pressure within the pores during the last stage of deformation. Wang and Karabin [108] studied the further densification of aluminium powder sheets via rolling. Parteder et. al. [12] modelled (via the Gurson model) the densification of sintered molybdenum powder compacts during hot upsetting. Parteder et. al. [109] also simulated the hot deformation of refractory metals using the Gurson model. They compared the density distribution results, given by the model, with those of a tapered disc produced by hot pressing.

Using Gurson's model, Chen et. al. [43] studied the predicted density distributions after consolidation of titanium powder by multi-stage compaction. Kim and Yang [34] used the model to simulate the densification behaviour of Ti-6Al-4V alloy by hot

vacuum pressing. They compared their result with Flecks [75] model and concluded that the Gurson model agreed well with experimentally obtained results.

3.9 Stability and convergence issues

Gurson's model is a highly computational intensive model and could experience numerous numerical stability problems. Finite element calculations are generally said to be stable when approximation errors are not magnified. Numerical instability can arise for different reasons as explained below [104].

- When the material deforms to such a large extent that the finite element mesh does not represent the geometry of the problem, the analysis might be terminated prematurely. This problem can be solved by simplifying the geometry and using appropriate re-meshing rules.
- In powder metal forming analysis, such as powder forging, the elements under high hydrostatic stress states can yield under a different criterion. For example, elements experiencing high shear stress, which triggers a sudden difference in the local stiffness matrix, could lead to instability.
- Stability is important when the material model is being implemented in Abaqus/implicit, where the program determines the time increment size necessary for the solution. Increment size needs to be controlled with care if the material model is being implemented using VUMAT. A material model algorithm needs to be developed in such a way that instability is controlled.
- There can be instability due to a random loading path direction, such as for problems with geometric complexity. A material element can experience a wide range of loading conditions (tensile, compression and shear) simultaneously depending on their location in the geometry.
- Contact instability can be induced when the material under deformation experiences a large resistance due to the boundary or contact conditions. For example, high frictional contact at an interface could magnify the non-linearity of the problem and this might be more computationally intensive than previously assumed.

3.10 Summary

In this chapter the general aspects of metal forming analysis in Abaqus software have been discussed. This included geometric modelling, material property definition, contact interaction, boundary conditions and mesh generation. Some of the important points in this chapter are summarised below;

- Abaqus software can be used to solve non-linear problems. Non linearity arises for three main reasons: material model, geometric sources and initial and boundary conditions. Non-linear problems require several iterations and can be computationally expensive.
- A Finite Element Analysis of metal forming problems involves large deformation, hence appropriate mesh and distortion control is necessary. Different mesh distortion control schemes have been discussed. An arbitrary Lagrangian-Eulerian (ALE) mesh adapted in this work is also discussed.
- Analysing powder forging in Abaqus requires a description of the material model that includes accurate physical and thermal properties. A Gleeble thermo-mechanical simulator was used to obtain the properties of the powder compact. The implementation procedure for the Gurson material model in Abaqus/implicit was discussed. However, model parameters (i.e. q_1, q_2, and q_3) need to be calibrated for different materials and processes.
- Application of the Gurson model to predict the relative density distribution in powder metallurgical processing is not novel, however to the best of the author's knowledge only a small amount of work has been previously carried out to model the powder forging process using Gurson's model for material with low initial relative density.
- Implementing Gurson's model can lead to stability and convergence issues. It can be challenging in Abaqus/implicit where the time increment sizes are determined by the user. Hence it is important to understand the factors that cause instability. Stability and convergence issues are minimal in Abaqus/explicit where the program automatically calculates the time increment sizes.

4 Implementation of porous metal plasticity (original Gurson's model) and simulation results

In this chapter, the implementation procedure and the simulation results for powder forging of porous titanium materials will be discussed. In order to analyse the densification behaviour of titanium powder compacts during powder forging a simple circular disc was upset forged. Figure 4.2 shows the initial powder compact geometry (Ø 42 mm x 40 mm) and the final forged shape. For convenience and efficiency in the simulation procedure the model is reduced by making use of the axisymmetric geometry, as shown in figure 4.1.

The first part, discusses the influence of important parameters that need to be considered for accurate representation of the upset forging of a circular disc. In the second part the implementation of a porous metal plasticity model is explained and few results are discussed.

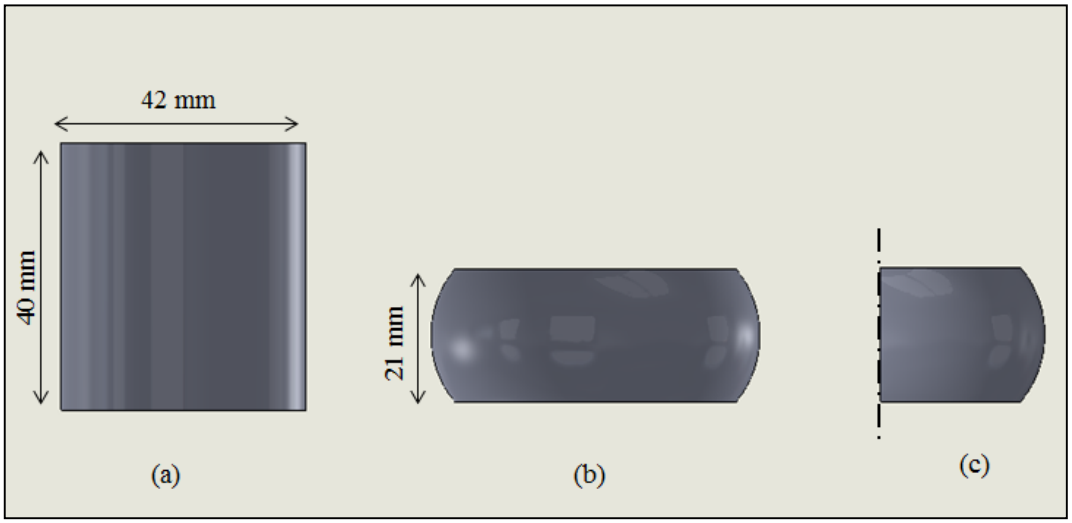

Figure 4.1: (a) initial powder compact; (b) powder forged disc; (c) axisymmetric geometry

4.1 Simulation study on the densification of a circular disc by upsetting

To understand the densification behaviour during thermo-mechanical forging and to determine the influence of the material parameters during powder forging, a simple 2D circular disc was created in Abaqus/standard as shown in figure 4.2. A coupled temperature-displacement analysis procedure was selected for the analysis step. The geometry was modelled as per the technique illustrated in section 3.1.1. The powder

compact and the dies were meshed with CPE4RT elements and the mechanical properties were assigned. The initial temperature of the powder compact was assigned based on the simulation plan. In Abaqus/standard the Gurson-Tvergaard model is introduced along with the material properties with an initial relative density of 0.75 and Tvergaard parameter q_1, q_2 and q_3 equal to one. For the initial simulation trials the frictional and thermal contact interaction was estimated. A value of coefficient of friction μ=0.1 was chosen and a default thermal contact property was assigned, however this would be validated later on, based on experimental temperature histories which will be explained in later sections.

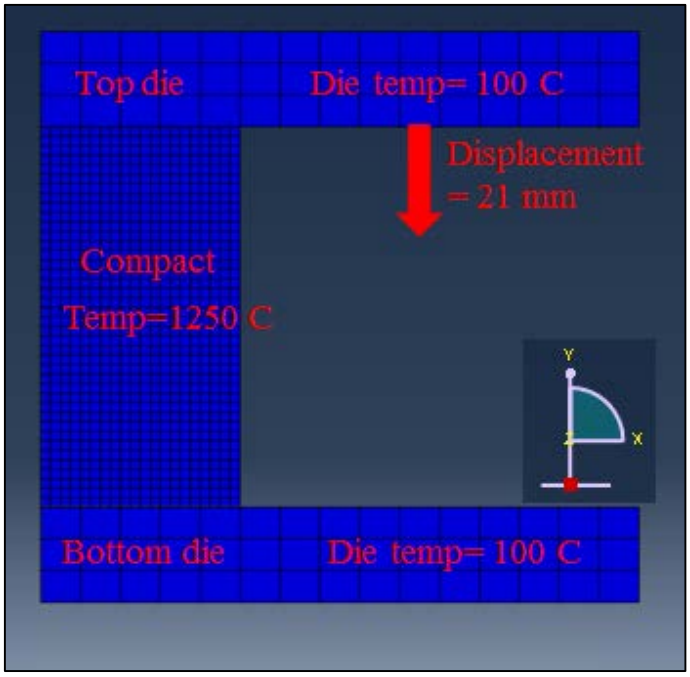

Figure 4.2: Simulation setup for circular disc powder forging analysis

The radial boundary conditions were applied to the powder compact allowing it to deform in both x and y direction. The bottom die was constrained (u1=0, u2=0, ur1=0, ur2=0). The top die was allowed to move a distance of 21 mm in the negative y direction (u1=0, u2=0.021 meters, ur1=0, ur2=0).

4.2 Mesh density selection

To analyse the effect of mesh density on the deformation characteristics of a powder compact, three different mesh densities are chosen. The regions of interest in this study are the upper right and lower right regions of the forged compact. The reasoning

behind this choice is because these regions undergo large plastic deformation and mesh distortion as they interact with the dies. The powder compact mesh elements in this region, can penetrate the dies and can cause immediate termination or failure of the analysis. Thus it is crucial to mesh the compact in such a way that it does not penetrate the die mesh elements. It is therefore important to perform a mesh sensitivity study to select the right mesh density.

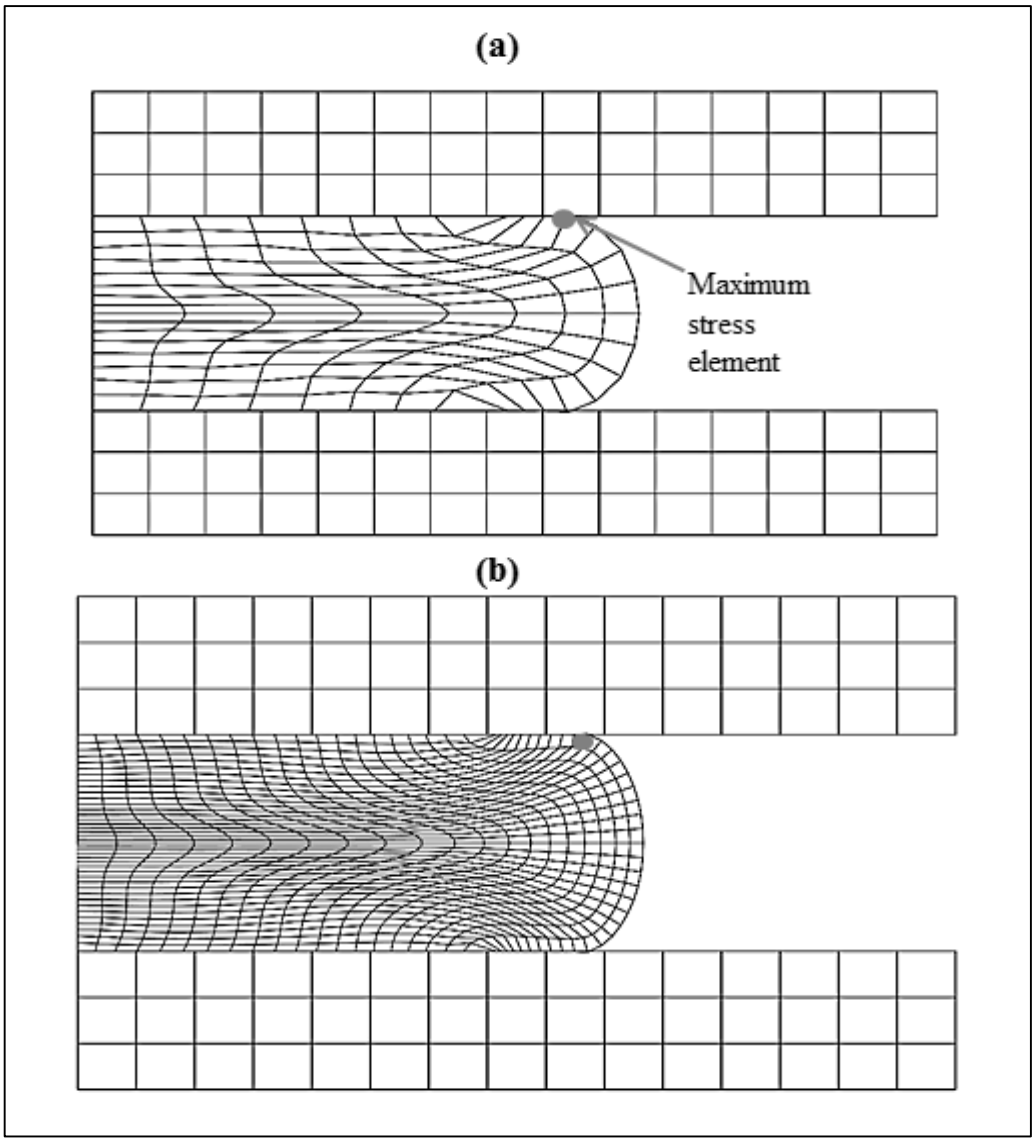

Figure 4.3: Deformed mesh shape of the powder compact (a) mesh density 8x32; (b) mesh density 40x40

4.2.1 Mesh sensitivity analysis

A mesh sensitivity analysis in FEM is a study performed to analyse the influence of mesh density on the simulated results. For analytical purposes the most highly stressed

element at the end of a forging step is selected. Eight different mesh densities were evaluated and maximum stresses at the nodes were plotted as shown in figure 4.4. It can be seen that there is a large variation in the maximum stress with a coarser mesh and as the mesh density increases there is a more uniform maximum stress. Further refinement of the mesh did not significantly affect the maximum stress value. However, it should be mentioned that although a finer mesh results in greater accuracy; it could lead to larger computational time. To be more computationally efficient a modest mesh density of 40x40 (1600 elements) was chosen for analysing powder forging of a circular disc.

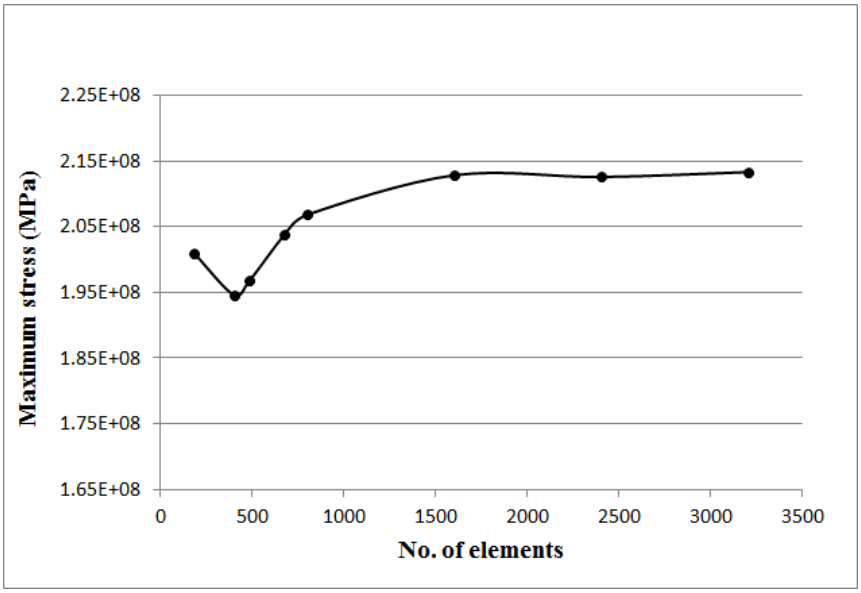

Figure 4.4: Mesh sensitivity study

4.3 Estimation of interfacial heat transfer coefficient between the powder compact and the die

The accuracy of a coupled thermo-mechanical simulation of powder forging depends on a proper description of the thermal contact at the die and powder compact interface. It is known that the heat flux at the powder compact and die interface is governed by the interfacial heat transfer coefficient. The interfacial heat transfer coefficient in metal forming simulations depends on several factors, such as the die material, work piece material, initial forging temperature, forging pressure, lubrication conditions and surface roughness of the die-work piece interface [110]. In many cases the data is not readily available in the literature, thus, it is common to formulate the boundary

condition in terms of the interfacial heat transfer resulting in a numerical solution that closely resembles the actual process. There are essentially two approaches to determine the interfacial heat transfer coefficient. One method is to choose a value of interfacial heat transfer coefficient such that the measured and calculated temperature distributions will resemble each other. Another method is to develop an inverse optimisation technique by model adjustment where the heat transfer coefficient is estimated, based on the difference between measured and calculated temperature histories (temperature-time profile). The latter is a more reliable method for an estimation of the heat transfer coefficient in powder forging, as it captures the influence of contact pressure and temperature on the heat transfer characteristics. The inverse optimisation technique used in this study is explained below.

The objective is to find the temperature dependent heat transfer coefficient value so that the measured and simulated temperature curves closely match. Although, it is known that the heat transfer during powder forging is a function of several variables, the temperature and contact pressure were assumed to be a predominant variable. The objective function is given below:

$$f(x) = \sum_{j=1}^{M} \sum_{i=1}^{N} \left(T_{i,j}^{simulated} - T_{i,j}^{experimental}\right)^2 \qquad 4.1$$

where, $T_{i,j}^{simulated}$ and $T_{i,j}^{experimental}$ are the simulated and experimental temperatures at the jth time step for the ith thermocouple. M and N are the number of time steps over which the calculations were carried out. The constraints in this optimisation were to maintain a decreasing heat transfer coefficient with decreasing powder compact temperature with respect to time and to get an increase in heat transfer coefficient with perfect interfacial contact (zero clearance).

4.3.1 Experimental measurements

Two thermocouples were used, one located inside the powder compact and another in the die, as shown in the figure 4.5. Temperature data was acquired during the forging process. The thermocouples were sampled every 0.25 seconds, as the overall forging step was completed in less than ten seconds. A smaller time step was necessary during

the forging cycle to capture the cooling histories of the powder compact and the dies. The thermocouples and the location holes were coated with copper paste (Loctite C5-A) to minimise the sensitivity error due to an interfacial air gap.

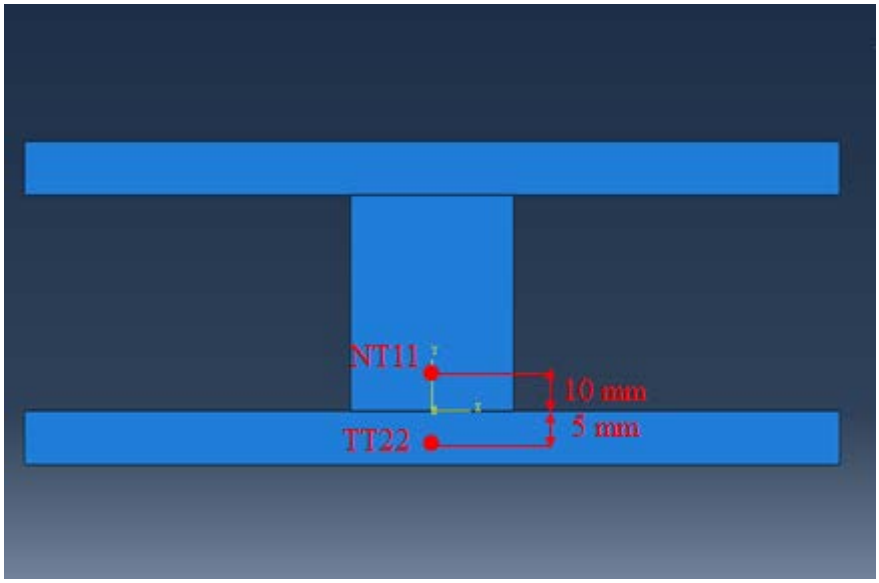

Figure 4.5: Thermocouple locations were temperatures were measured

4.3.2 Numerical model adjustment

The initial heat transfer coefficient value was based on a previous model obtained from the literature [84, 110]. From the literature it is found that for hot metal forging the interfacial heat transfer coefficient varied from a constant value of 10,000 W/m^2 K to 50,000 W/m^2 K [110]. Figure 4.6 shows the interfacial heat transfer coefficient data versus temperature. The temperature data obtained after the initial interface coefficient estimate can be seen in figure 4.7 where NE11 and NE22 are the temperature data obtained with the initial heat transfer estimate, NM11 and NM22 are the final temperature history data obtained with the modified heat transfer coefficient data shown in figure 4.7 and NT11 and NT22 are the experimentally measured temperature data obtained at the locations described in figure 4.5. Since the heat transfer is a time and space dependent process, the temperature in the die gradually increases while the compact drastically cools down with time.

Several iterations were performed to obtain the final temperature history that closely matched the experimental results using an inverse optimisation technique, described

in section 4.3. Although an exact match was not obtained, there was an improvement to the existing model. This could be for several reasons, for instance heat transfer is both time and space dependent, i.e. the temperature drop near the surface is greater than in regions away from the surface. The heat transfer coefficient model, used here, is temperature dependent and for an accurate description of the interfacial heat transfer coefficient it is important to capture the effects of pressure, surface roughness and interfacial air gap etc. However, the present work is reliable enough to predict the heat transfer during powder compact upsetting, as the overall computational results agree well with the simulated FEA and experimental results.

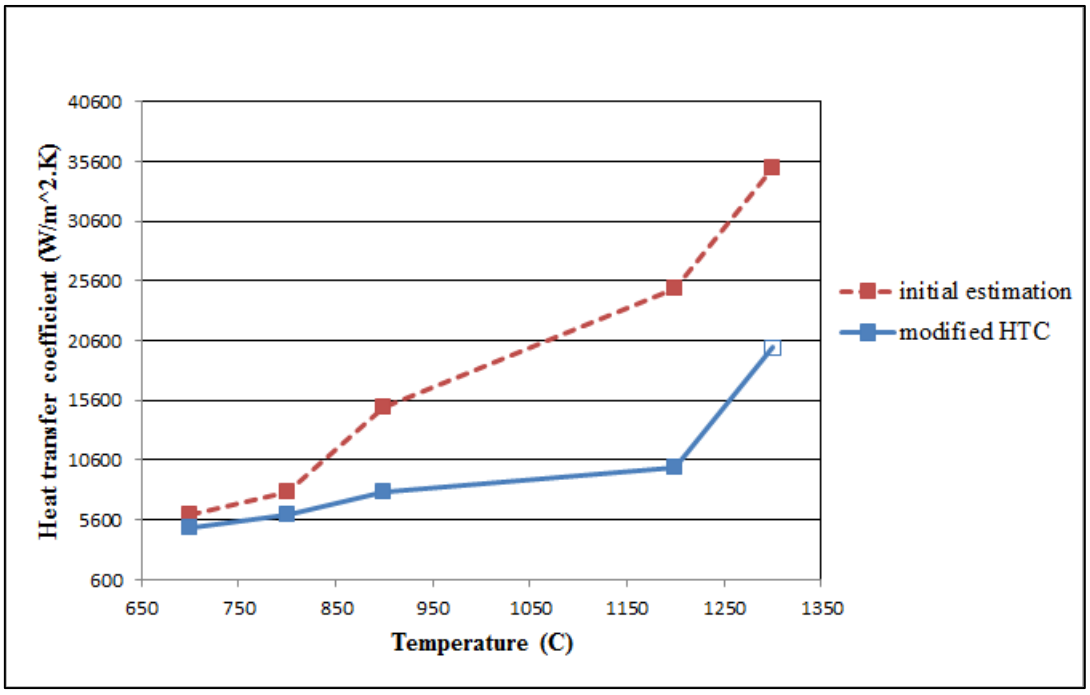

Figure 4.6: Heat transfer coefficient vs. temperature

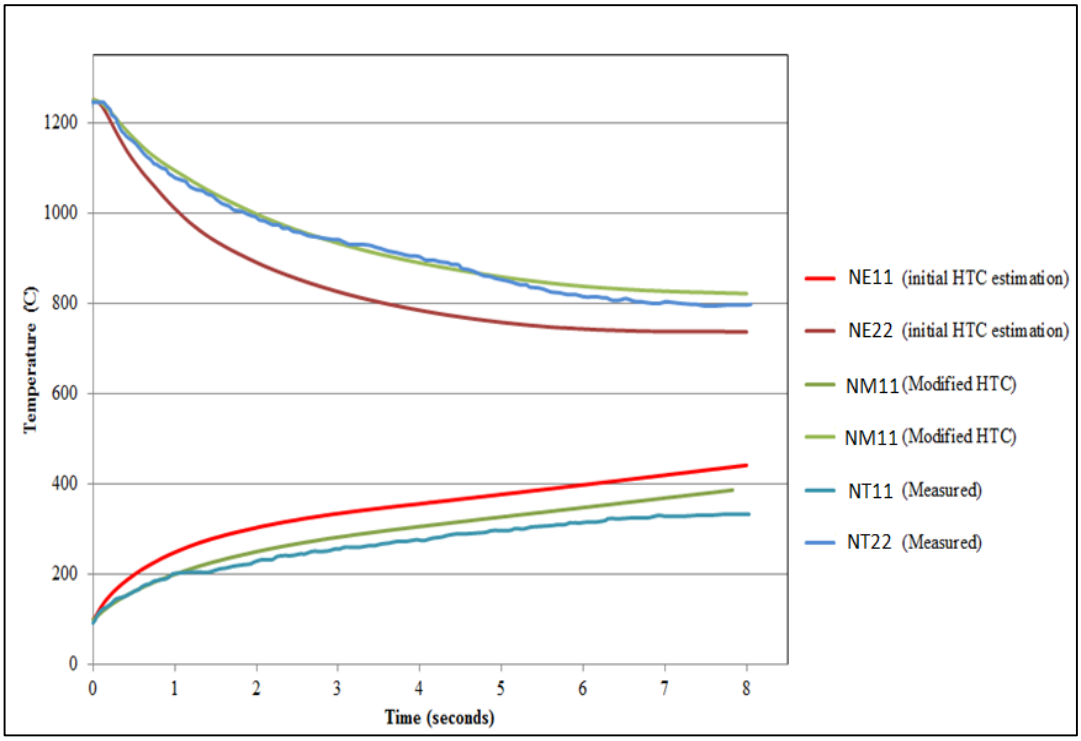

Figure 4.7: Measured and numerically obtained temperatures with modified HTC

4.4 Simulation results for upsetting of a circular disc

After the upset forging parameters were defined, simulation models were setup according to table 6. An upsetting simulation was performed for HDH titanium and Ti-6Al-4V powder compacts with two deformation percentages (50 % and 65 %). From the initial simulations, the effect of the degree of deformation on stress, plastic strain, strain rate, temperature distribution and relative density are results of interest.

Model	Simulation time	Alloy type	Deformation percentage	Initial forging temperature	Initial die temperature
Model 1	8 sec	HDH titanium	50 %	1250 °C	100 °C
Model 2	8 sec	HDH titanium	65 %	1250 °C	100 °C
Model 3	15 sec	Ti-6Al-4V	50 %	1250 °C	100 °C
Model 4	15 sec	Ti-6Al-4V	65 %	1250 °C	100 °C

Table 6: Simulation plan

4.4.1 Influence of deformation percentage on equivalent stress distribution

According to the simulation plans, simulations were performed to deform the powder compact to 50 % and 65 % respectively. It is well known that the deformation degree has a direct influence on the consolidation behaviour in powder forging. The Von-Mises stress distributions obtained for four simulation results is shown in figure 4.8.

From the simulation results it can be seen that when using HDH titanium powder the maximum Von-Mises stresses at 50 % reduction are at the top and bottom corners. However, when the reduction is 65 % the maximum stresses occur near the centre of the disc. Compared to HDH titanium powder, the stresses in a Ti-6Al-4V alloy are higher, however this is expected as the flow stress for the latter is higher than that for HDH titanium powder. In all the four simulation cases the stress value increased with the amount of deformation. This is expected, as the material being modelled is porous, with a low initial relative density. Thus as the density increases the equivalent stress also increases. Figure 4.9 shows equivalent stress plotted against deformation for the central node. From the figure, it can be seen that the equivalent stress value at the centre of the preform increases with the deformation percentage. Higher stresses for Ti-6Al-4V indicate that larger forging forces are required for further reduction. The lowest equivalent stress is recorded for an HDH titanium powder compact with 50 % reduction.

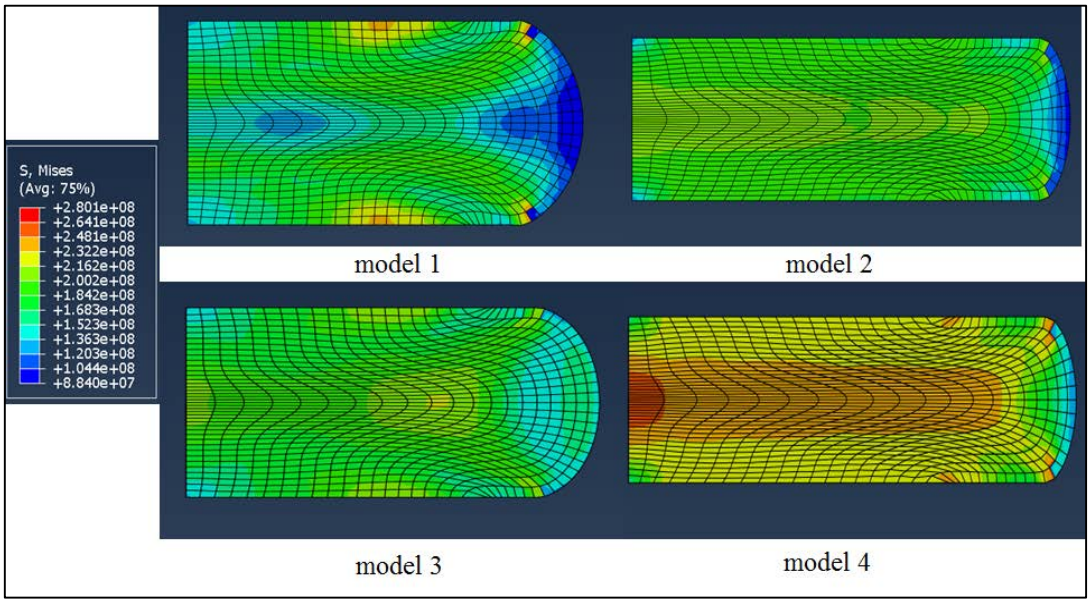

Figure 4.8: Von Mises stress distribution at 50 % (model 1 and 3) and 65 % (model 2 and 4) reduction

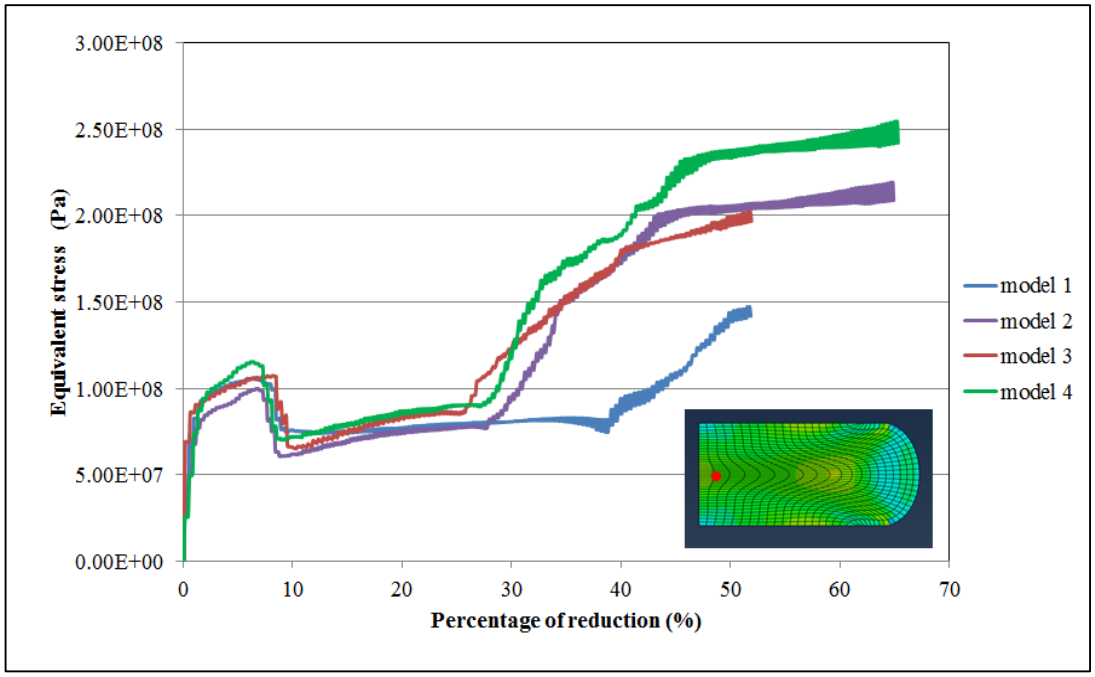

Figure 4.9: Equivalent stress vs. percentage of reduction

4.4.2 The influence of the degree of deformation on the equivalent plastic strain distribution

The equivalent plastic strain is shown in figure 4.10. The maximum plastic strain in all four cases occurred at the centre of the compact which is consistent with the plastic strain results described in the literature for different plasticity models [12, 13, 64]. The minimum plastic strain occurred around the circumference of a powder compact. The explanation for low plastic strain on the outer circumferential surface can be found in the deformation pattern during upsetting which is explained in section 4.4.5. It can also be seen from figure 4.10 that plastic strain is minimum at the top and bottom faces of the powder compact after 50 % reduction in height. The plastic strain at the top and bottom faces improves with further reduction in height, as shown in models 2 and model 4. Figure 4.11 shows the equivalent plastic strain histories vs. percentage reduction in thickness. The amount of plastic strain is higher in model 4 (Ti-6Al-4V, 65 % reduction) compared with the other three cases.

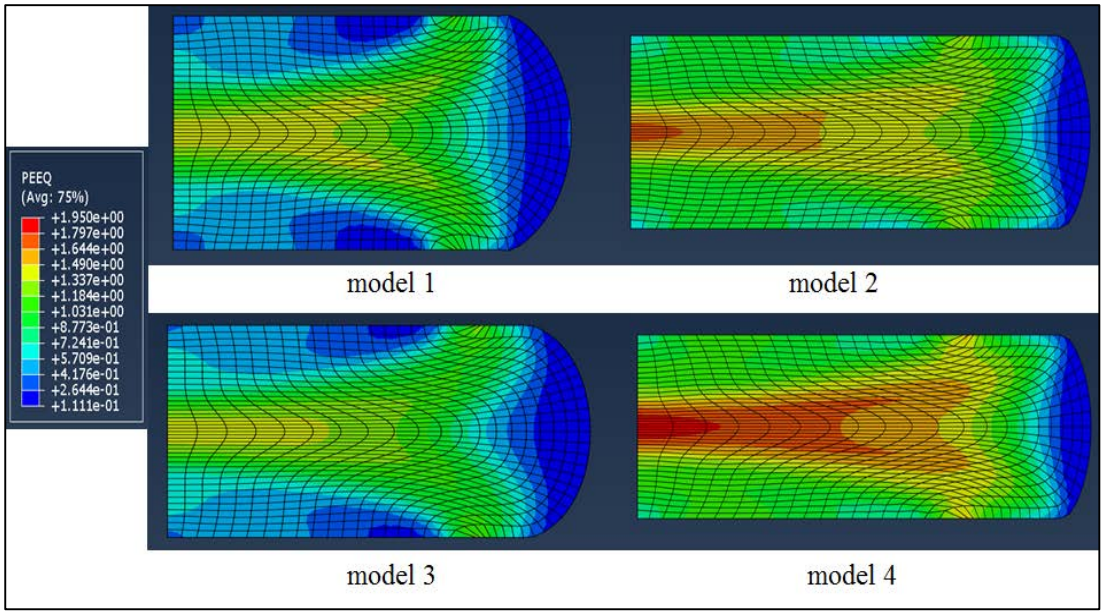

Figure 4.10: Equivalent plastic strain distribution at 50 % (model 1 and 3) and 65 % (model 2 and 4) reduction of height

The plastic strain increment in models 2 and 4 follows a similar trend after 35 % reduction. This can be explained by the load vs percentage of reduction curve explained in a later section.

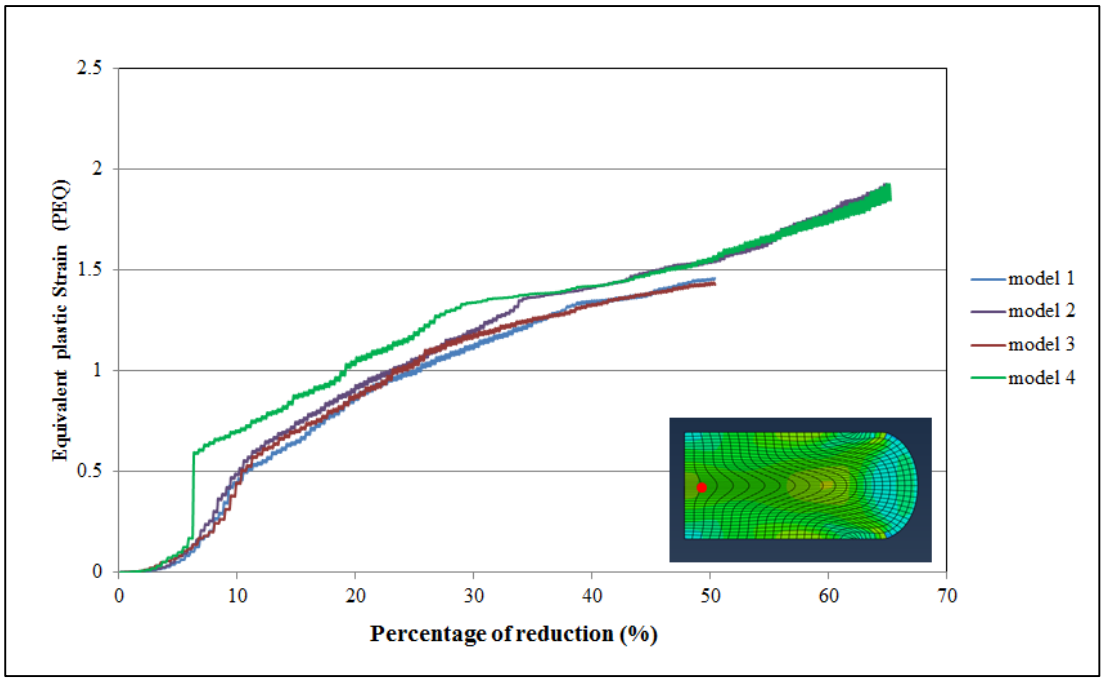

Figure 4.11: Equivalent plastic strain vs. percentage of reduction

4.4.3 Influence of powder compact temperature during deformation

As illustrated in the earlier sections, a coupled-thermo-mechanical simulation procedure was chosen for forging analysis, thus it is expected that there will be heat transfer between the powder compact and the forging dies. The temperature distribution in a powder compact before forging, after 30 % and 50 % reduction is shown in figure 4.12. According to the initial simulation plan (table 6) the powder compact and die temperatures were pre-set to 1250^{o} C and 100^{o} C. The interaction between the powder compact and its surroundings was defined by the film coefficient and atmospheric temperature during the experiments. The temperature field distribution during forging was calculated using a program based on the thermal conductivity of the material and the interfacial heat transfer coefficient determined by the algorithm detailed in section 4.4.5. It can be seen that the heat transfer between the die and compact played a major role in the decrease in compact temperature during forging, thus heat losses by radiation were neglected in the calculation.

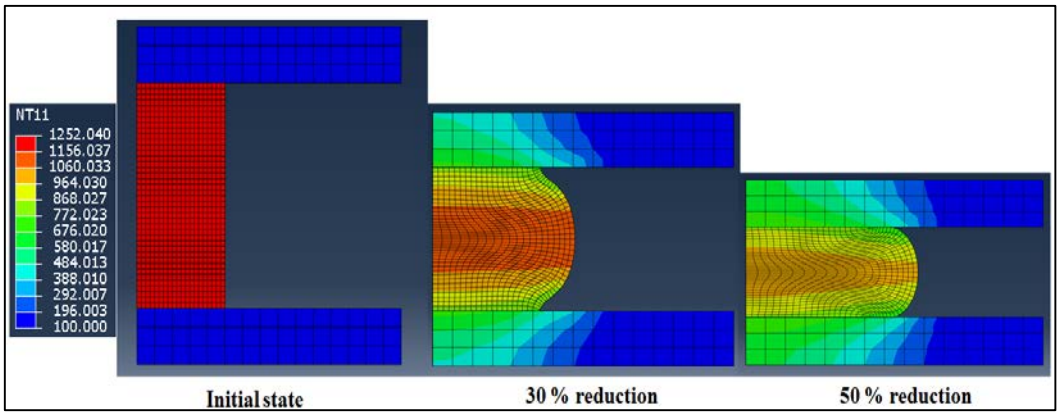

Figure 4.12: Temperature distribution in the powder compact and the die during forging

Figure 4.13 illustrates the temperature distribution in a powder compact for four simulation conditions. In all the four cases, losses in thermal energy are observed during deformation and the heat generation from the deformation itself did not compensate for the temperature losses. The highest temperature losses are observed in an HDH titanium powder compact during both a 50% and 65 % reduction, compared with a Ti-6Al-4V powder compact. This can be explained by the lower thermal conductivity of Ti-6Al-4V (6 - 7 W/ m^2 K) powder compacts compared with HDH titanium powder (20-24 W/m^2 K). In the simulation and the experiments, an assumption was made that initially the temperature of the powder compact was

uniform; however from the literature and induction heating experience, this might not have been the case. A lower thermal conductivity means that the material requires a longer holding time at temperature to achieve a uniform temperature distribution, which is often the case with Ti-6Al-4V powder compacts [111].

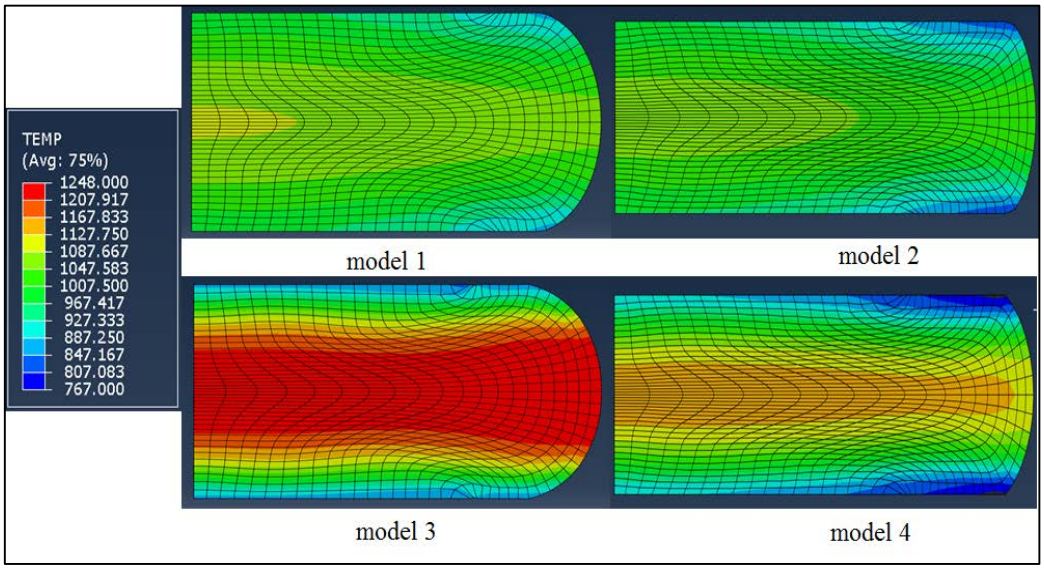

Figure 4.13: Temperature distribution at 50 % (model 1 and 3) and 65 % (model 2 and 4) reduction

4.4.4 Influence of strain rate sensitivity during deformation

In ingot forging practise, it is desirable to have a uniform strain rate, as a non-uniform deformation rate can adversely affect the quality of a part. In an industrial setting, a uniform strain rate can be achieved by controlling the ram movements, lubricant conditions and die geometry. The strain rate sensitivity of the flow stress of materials such as titanium is significant and known to be especially so at high temperature [24]. The flow stress curves for porous materials tested over a range of strains and strain rates are expected to be lower when compared to fully dense materials. In this work, titanium powder compacts were modelled as porous and so there is a change in density with deformation. It is of interest to see how the strain rate distribution changes with respect to changes in geometry, temperature and percentage reduction during upset forging. Figure 4.14 shows the strain rate distribution obtained after simulation.

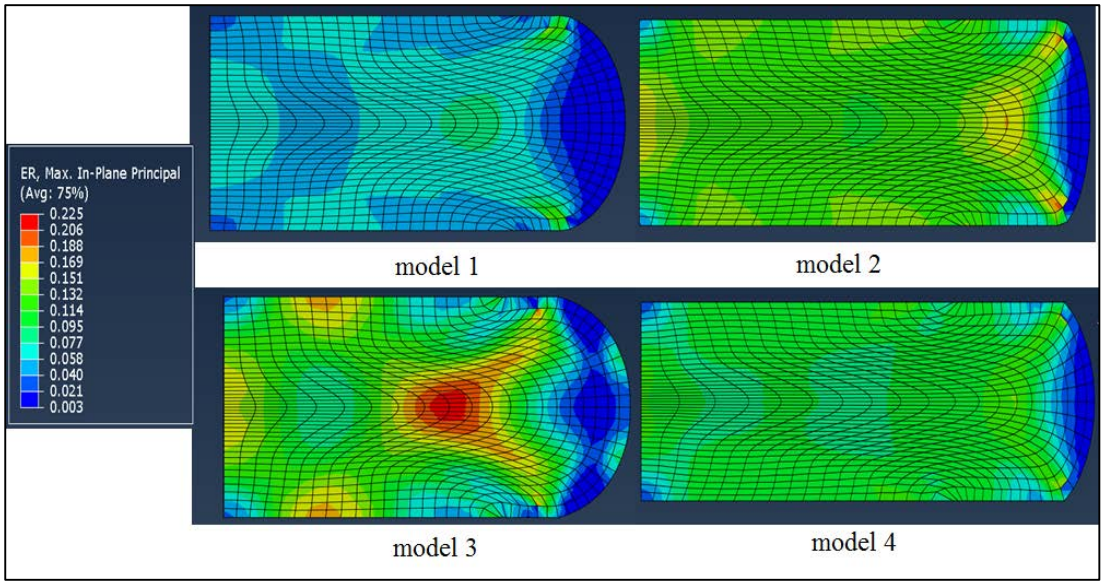

Figure 4.14: Strain rate distribution at 50 % (model 1 and 3) and 65 % (model 2 and 4) reduction

It can be seen from the figure that in all four cases, the lowest strain rate can be observed at the outer circumference of a powder compact. This is consistent with the low equivalent stress and pressure distribution. The highest strain rate is observed in model 3, because of the high temperature of a compact after 50 % reduction. The strain rate distribution tends to become more uniform with increasing amounts of deformation, as can be seen in models 2 and 4. This is due to the fact that at larger deformations the material densifies and tends to behave like fully dense material. This trend is consistent with deformation studies of porous materials reported previously by several researchers [12, 32, 109].

4.4.5 Relative density evolution during deformation

The simulated relative densities for the four models are shown in Figure 4.15. An initial relative density of 0.75 for the material was specified in all of the four models. From the simulations it is clear that the relative density increases with increasing amounts of deformation. The highest relative density obtained was at the centre of a powder compact. On further deformation the densified region in the centre of a powder compact expanded outwards because of the larger stresses in the centre of a compact. This causes pores to collapse and then full closure of the pores takes place. The lowest relative density was found to be at the circumference of a powder compact. These trends are consistent with the equivalent stress and strain distribution results. Also, a high relative density at the centre of the compact during hot upset forging has

been reported in several studies [12, 32, 107]. It is also worth noticing that, despite an initial starting relative density of 0.75, the simulation results show a lower relative density of 0.70 in model 3 and model 4. This is due to the characteristics of the Gurson- Tvergaard material model, which takes into account not only the void closure but also void coalescence. From experiments and 3D simulation results, it can be seen that such low relative density states can lead to circumferential cracks at the outer edges of circular forged discs, as shown in figure 4.16 (a). These cracks propagate due to the circumferential tensile stresses in the regions with residual porosity. With increasing deformation, the tangential tensile stresses increase in magnitude in the peripheral area causing further cracking and void nucleation.

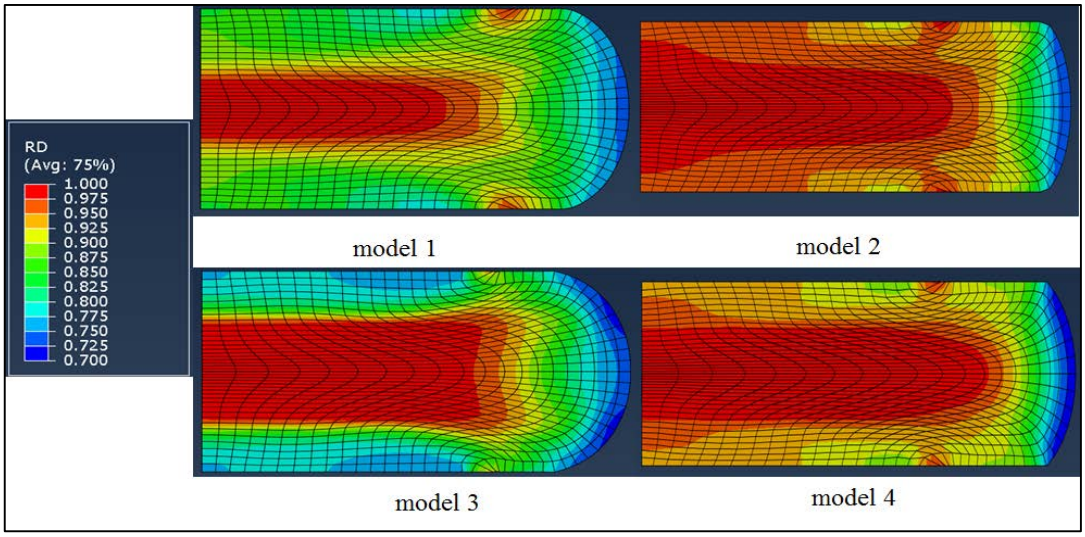

Figure 4.15: Relative density distribution at 50 % (model 1 and 3) and 65 % (model 2 and 4) reduction

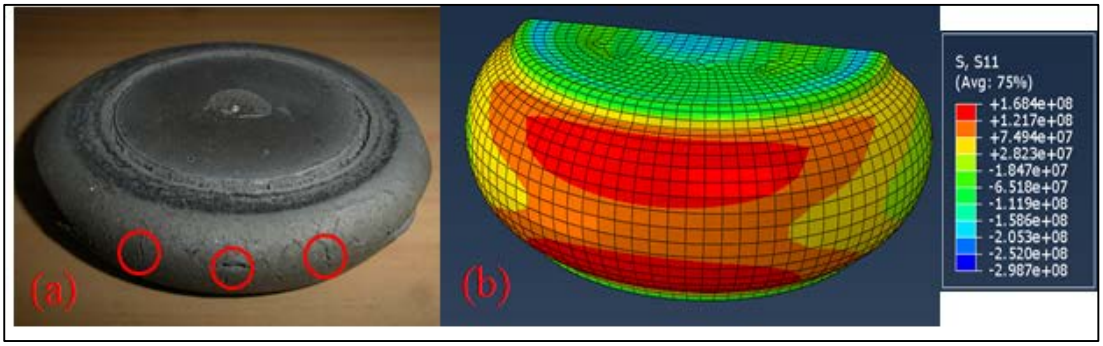

Figure 4.16: (a) forged circular disc with circumferential cracks; (b) 3D simulation indicating tangential tensile stresses

For obtaining relative density history during deformation at specific locations within the powder compact, nine unit cells where selected at predetermined locations as shown in figure 4.18 (a). The co-ordinates of these cell locations are shown in figure 4.18 (b). The unit cell data was monitored and recorded using Abaqus output during the simulation. Abaqus provided relative densities at four nodes corresponding to the each unit cell. Average relative density history was then calculated using the tools provided in the Abaqus results module and plotted against percentage of reduction as shown in figure 4.17. The figure shows the relative density histories for the central node in the models defined according to the simulation plan. It can be seen that for the central node, in all the four simulation cases, complete densification occurs at nearly 30 percentage reduction. However, this is not true for the nodes located at predefined distances within the powder compact.

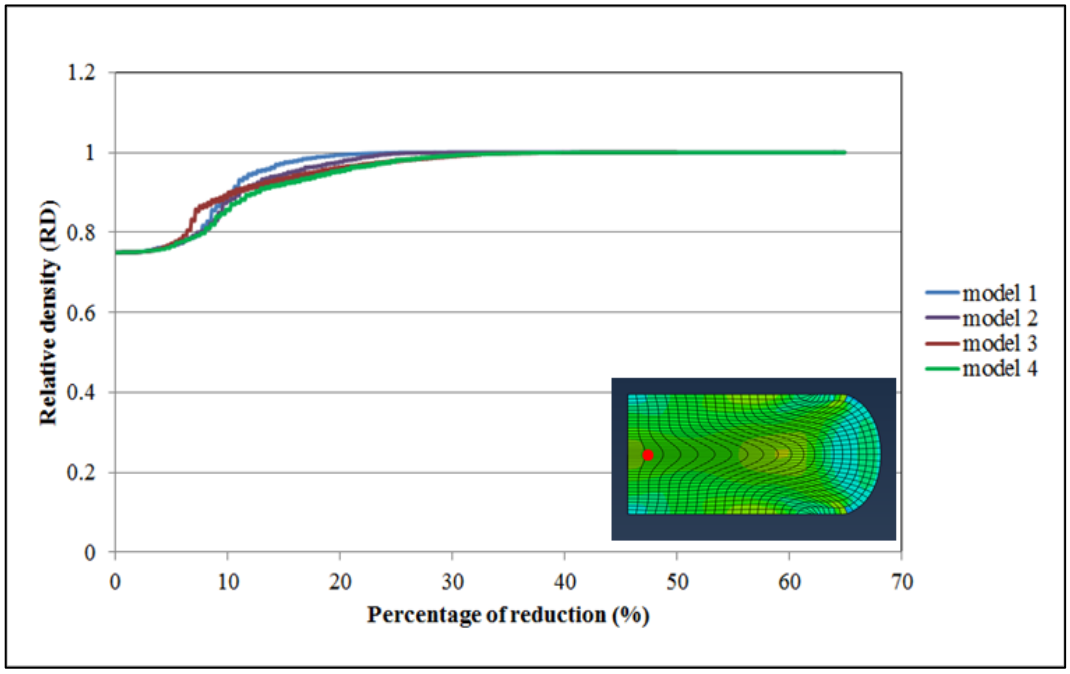

Figure 4.17: Relative density vs percentage of reduction

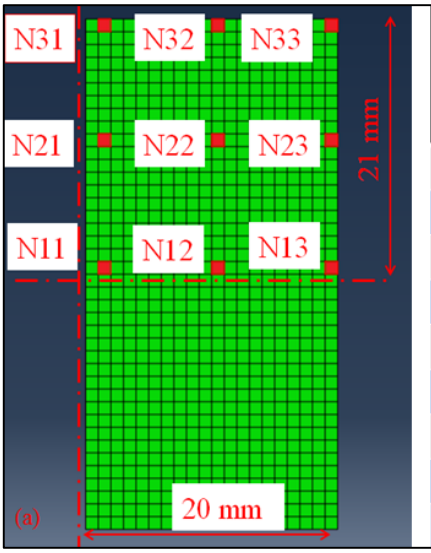

Element set	Co-ordinates	
	(x) (mm)	(y) (mm)
N11	0.8	0.6
N12	9.9	0.6
N13	18.9	0.6
N21	0.8	10.7
N22	9.9	10.7
N23	18.9	10.7
N31	0.8	20
N32	9.9	20
N33	18.9	20

Figure 4.18: Unit cell locations in the model with co-ordinates

Figure 4.19 to figure 4.22 show relative density histories at nine locations within the powder compact for the four simulation cases. The densification rate is highest for the central node (N11) in all four simulation cases. In model 1 and 2, for a HDH titanium powder compact, the maximum relative density is achieved after 20 percent of deformation, while in models 3 and 4 the same amount of densification occurs after a 30 percent reduction. The primary reason for this is the lower flow stress curve for HDH titanium compared with that of Ti-6Al-4V alloy. Though this difference in densification rate may be significant at this stage of consolidation, it is interesting to note that on further deformation there is a tendency to follow the behaviour of a fully dense material.

Higher densities were seen at the top right node (N33) in the compact. The densification rate at this node differs after 50 percent and 65 percent deformation. The maximum relative density found at this region was above 0.9 in all the four simulation cases. However, the relative density achieved for Ti-6Al-4V alloy was lower than that for HDH titanium and it was noticed that the relative density increased further with increasing deformation.

The lowest densification in all four simulations was at the central circumferential node (N13). In the case of models 3 and 4, for a Ti-6Al-4V alloy, the relative density at this region after 50 % and 65 % deformation is below the initial relative density of the material. In practice, the material in this low density region is considered to be

redundant or it breaks away from the powder compact, as explained in the density field distribution plots in the previous section.

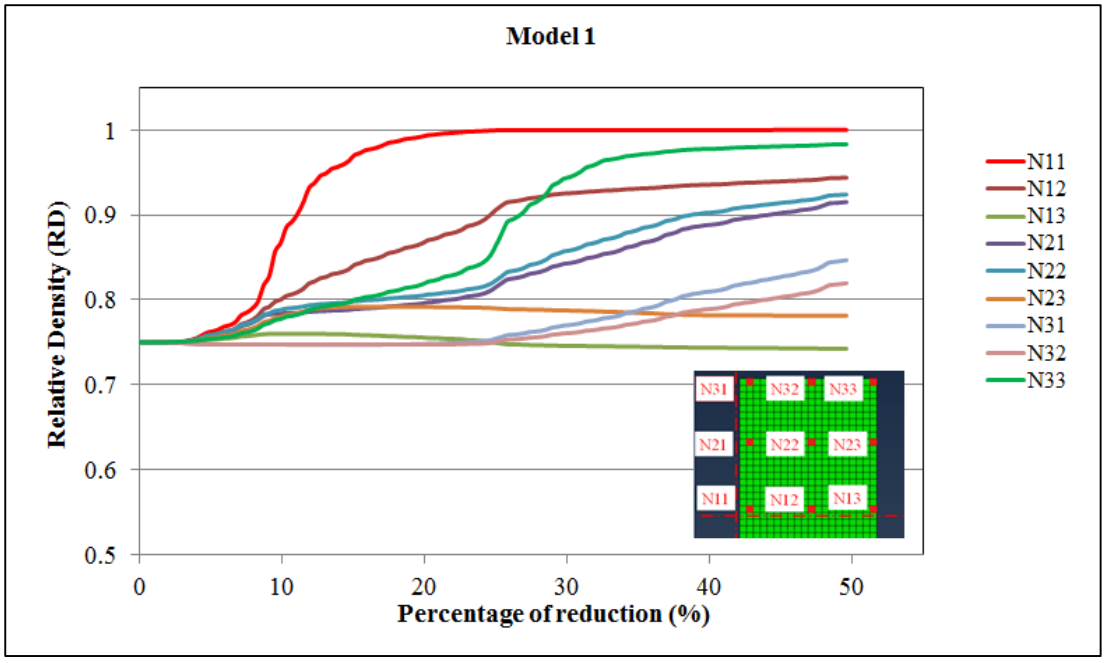

Figure 4.19: Relative density history vs. percentage of reduction for model 1

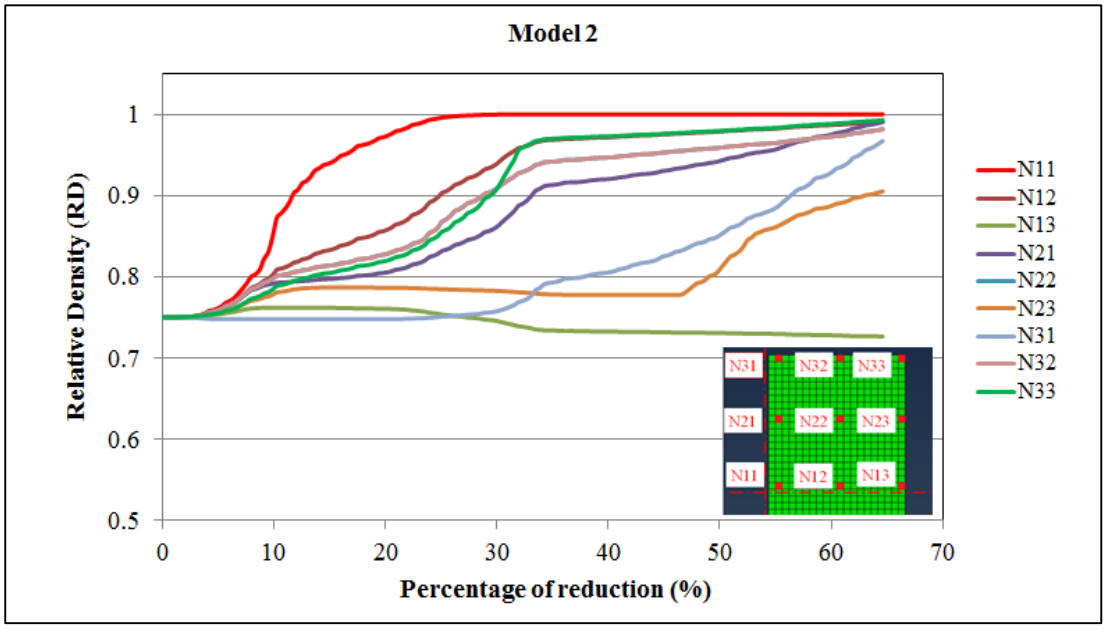

Figure 4.20: Relative density history vs. percentage of reduction for model 2

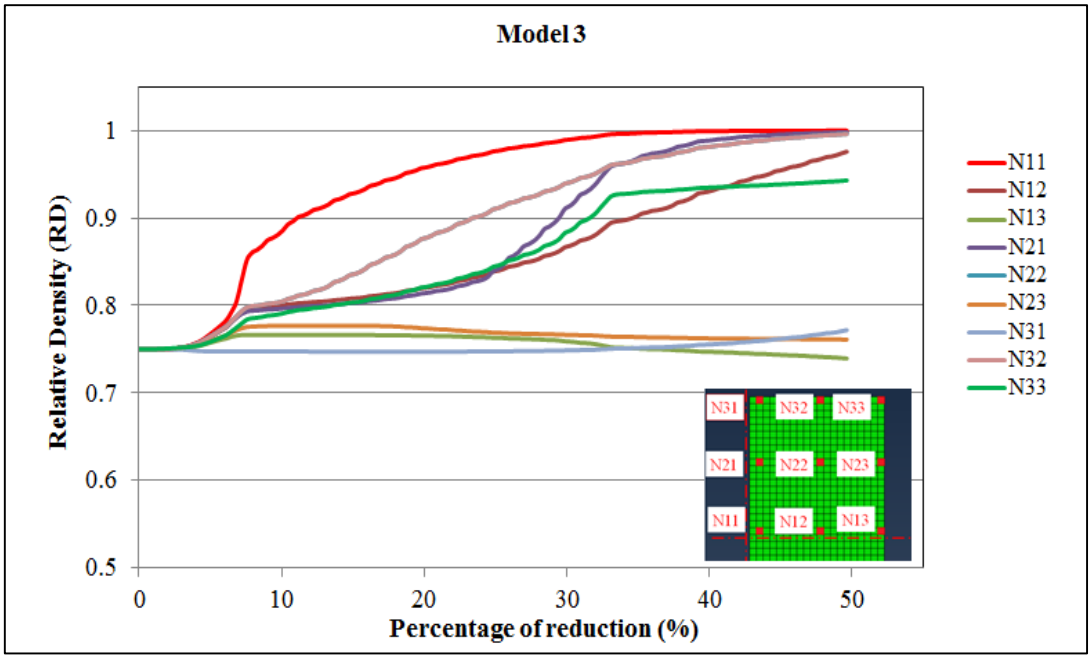

Figure 4.21: Relative density history vs. percentage of reduction for model 3

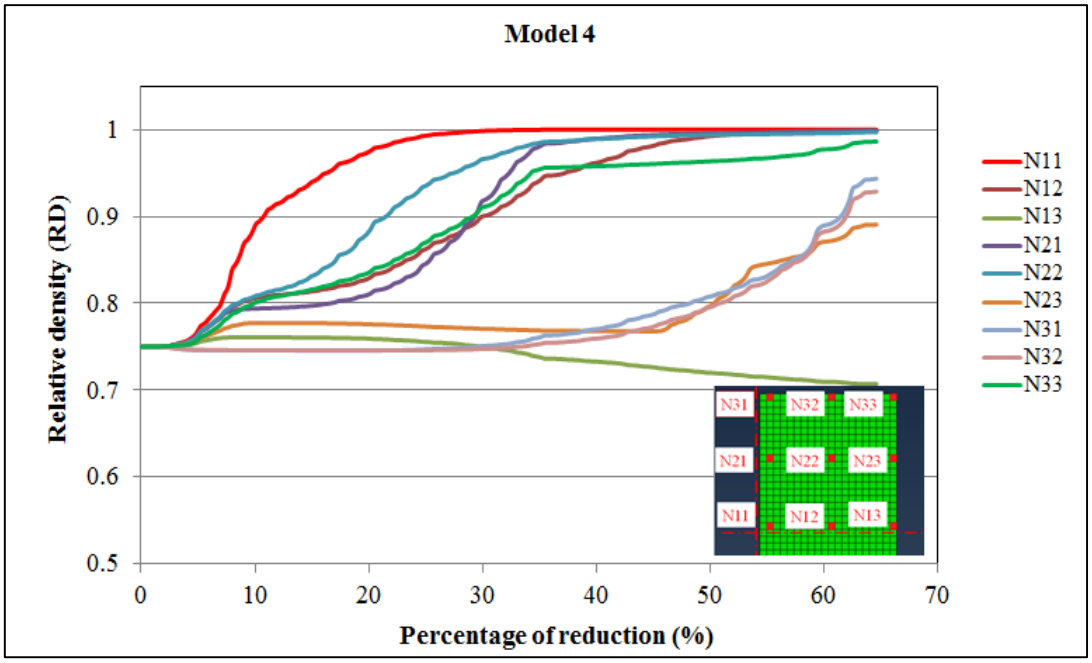

Figure 4.22: Relative density history vs. percentage of reduction for model 4

4.4.6 Force evolution during upset forging

Load-displacement curves are quite helpful in guiding our understanding of determining the workability of specific materials and therefore the selection of press equipment. It is known that the flow stress, frictional conditions, part geometry and material temperature influences the load required for forging operations. The flow stress of a material increases with increasing deformation rate and decreases with compact temperature. In addition to this, in powder forging the deformation load also depends on the densification rate. For example, when the density is low the material flows more easily; therefore a lower forging load is required. As the density of the material increases the applied forging load also increases.

Figure 4.23 shows the simulated forging load histories during upsetting for four different simulation cases at an initial billet temperature of 1250℃. Abaqus determines the load-displacement curves during forging based on the material flow stress data, taking into account the effects of thermo mechanical coupling. The load increases rapidly at the beginning and then more steadily in all the simulation cases. Larger forces are required for models 3 and 4 due to the higher flow stress of Ti-6Al-4V alloy compared with models 1 and 2 at the same temperature. The forging load rapidly increases after 55 percent deformation as a result of material densification.

The maximum forging load occurred at 65 percent reduction in height for model 4 and closely reached the full capacity of the 100 ton press machine. This is important to note as hydraulic machines are essentially force-restricted machines and their capabilities are limited by the maximum available force. But from experience, it is seen that the material will continue to deform at full capacity as long as the temperature of the powder compact is within a workable range. However it is not advisable to run a press at close to full capacity as it can lead to leaks and failure of hydraulic components such as piston rings etc.

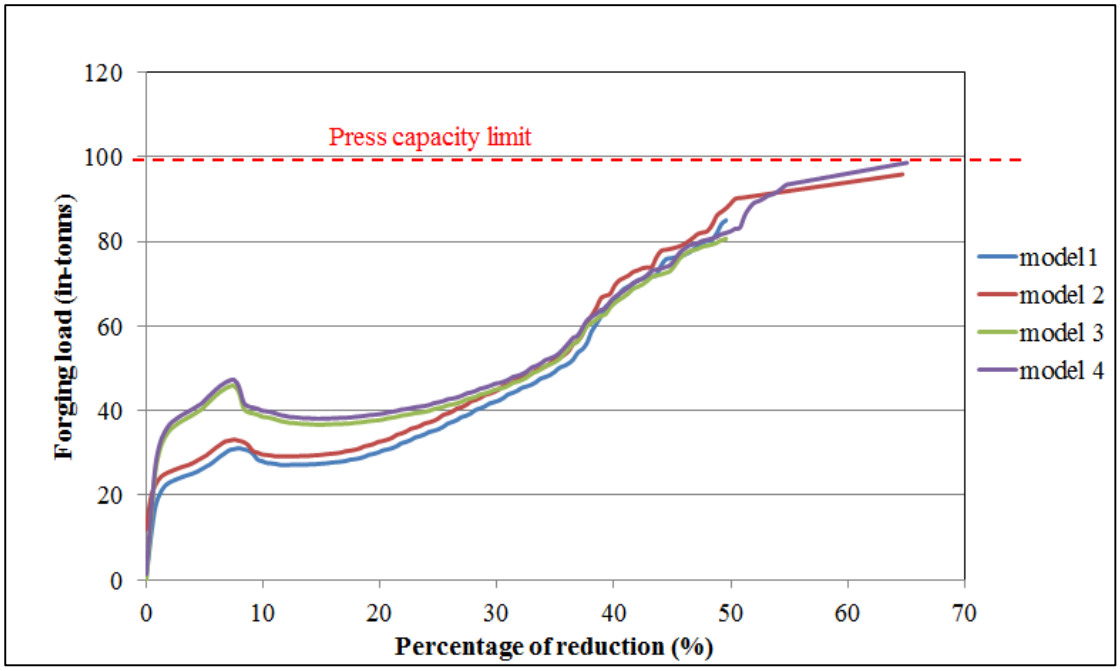

Figure 4.23: Load vs percentage of reduction curve

It can be seen that the load histories of models 1 and 2 correspond quite well (same material), there is only a slight difference between the curves and this is as a result of the different time increment steps used in the simulation. Also, it can be seen that after an initial rapid increase the load curve becomes steady after 10 percent reduction until 40 percent reduction. After 40 percent reduction the forging load further increases to a maximum. This trend corresponds to the density increase as seen from the relative density plots.

4.4.7 Material flow and densification during upset forging

The deformation pattern during upset forging can be visualised by a series of flow direction vectors as shown in figure 4.24. The following observations are made from these figures.

At the early stages of compact reduction the flow vectors in the material tend to move along a line parallel to the load application. After 12 % reduction the material near the centre tends to move outwards at the onset of barrelling. The deformation and densification at this stage is a complex phenomenon due to the collapse of pre-existing pores at the centre. The high temperature causes the stresses, deriving from the applied pressure, to reach the compressive yield strength of the material. However due to the

friction and chilling effect at the face of the die, only minor lateral flow of the material is observed. As the material near the circumference barrels outward only a limited amount of pressure is transferred thus there is very little increase in densification. On further reduction, the material at the top unifies with the material flowing in the lateral direction and further densification occurs at the top and bottom surfaces of the compact. However the final density observed is lower than that seen at the centre of the compact.

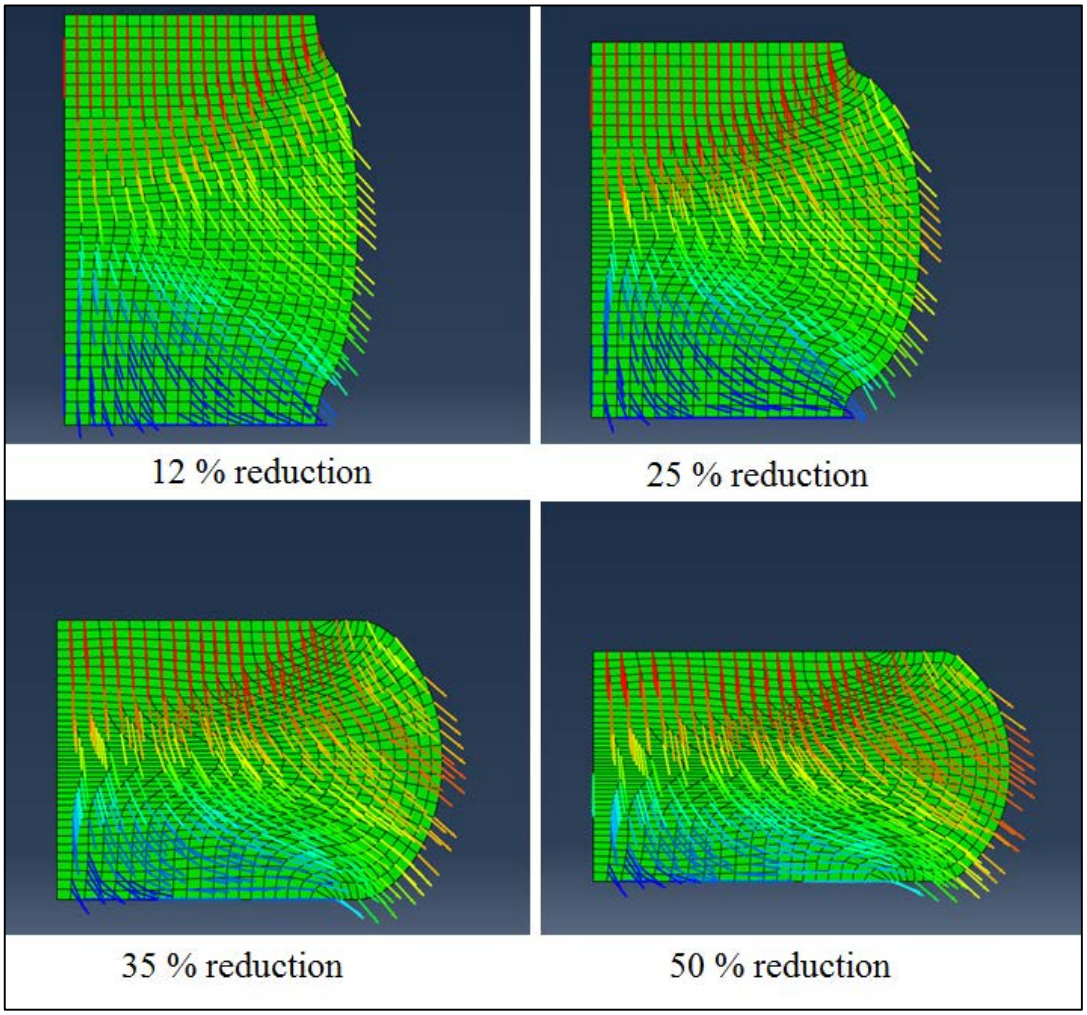

Figure 4.24: Material flow during at various reductions

Barrelling due to frictional constraints increases the tangential circumferential stresses and further opens the pre-existing pores near the peripheral region.

4.4.8 Effect of the frictional coefficient on the relative density distribution

In this section the respective relative density variations during powder forging are modelled for different frictional conditions. Simulations on HDH titanium compacts, with an initial relative density of 0.75, were carried out at an initial forging temperature of 1200℃ and a reduction in height of 50 percent. Two different friction conditions were studied. The coefficient of friction values were chosen based on the solid lubrication conditions used in the powder forging process. From the literature it was found that the coefficient of friction with a solid graphite lubricant ranges from 0.1 to 0.3, depending on the temperature of the surface [112, 113]. The intention of this section is to show the effect of the frictional condition on relative density. Simulation studies were performed with coefficients of friction of 0.1 and 0.3.

Figure 4.25 to figure 4.26 show the relative density distribution with two different frictional conditions. It was seen that the frictional condition had an influence on the uniformity of the density distribution during upsetting. For lower the friction coefficient, the density distribution was found to be more uniform. As the frictional coefficient increased, the magnitude of the density distribution decreased. It must be noted that, apart from friction the density distribution also depended on temperature, forging load and the contact surface area.

From these simulation results, it is clear that lower frictional coefficients can result in more uniform densities in the forged powder compacts. In practice, the frictional effect can only be reduced through appropriate die lubrication. When studying densification models, it is important to isolate the effect of frictional coefficient on density distribution, thus in all the case studies in this work a consistent frictional coefficient of 0.1 is chosen to simulate friction.

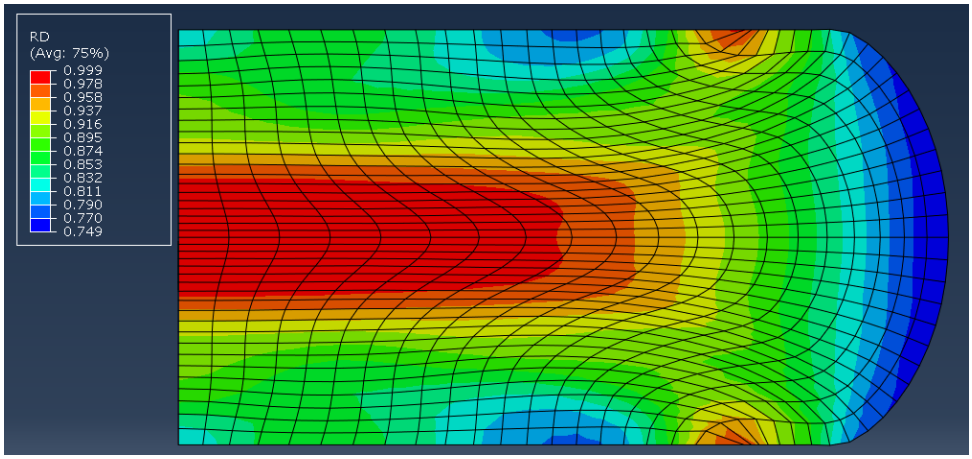

Figure 4.25: With friction ((μ=0.1)

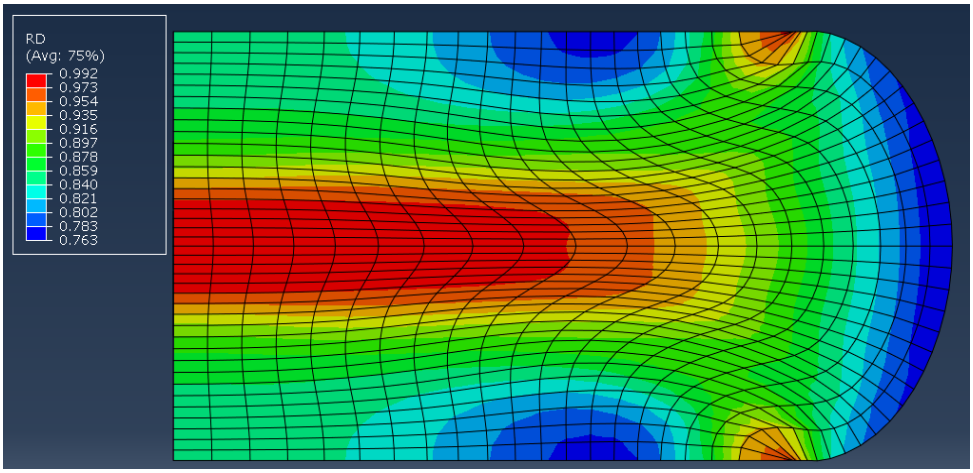

Figure 4.26: With friction ((μ=0.3)

4.5 Summary

This chapter discussed the procedure for implementing the Gurson porous metal plasticity model in Abaqus. The deformation and densification characteristics for a titanium powder metal compact, under upset forging, were studied using a porous metal plasticity yield criterion.

- Emphasis on the first part of the chapter was placed on conveying the relevance of mesh sensitivity on the simulation results. The accuracy of the results was compared with various mesh densities to obtain results with a satisfactory computational response.
- Since the simulations performed in the present study involved thermo-mechanical coupling, an accurate interfacial heat transfer between the dies or systems in direct contact was required. An inverse optimisation procedure was followed to obtain these values, as a function of temperature, by comparing the preliminary simulation results to the experimental work.
- Upset-forging simulation of HDH titanium powder compact and Ti-6Al-4V alloy cylindrical discs was performed using the original Gurson model. The degree of deformation was analysed in terms of simulation results such as equivalent stress, strain, temperature distribution and strain rate.
- Changes in relative density with increasing amounts of deformation were predicted by the original Gurson model. The highest density was observed at the centre of a billet during upset forging. The frictional forces and material flow pattern had a direct influence on the relative density distribution in the final part.
- Relative density during densification by deformation was the main objective of the present work. From the work done so far it was found that the original Gurson model is very general for porous materials and does not take into account internal state variables, such as pore shape and mode of application of the load, for specific materials. This therefore requires further investigation, taking these into account.

5 Gurson-Tvergaard model parameter estimation (q_1, q_2 and q_3) and relative density validation

As described in section 2.4; the parameters q_1, q_2 and q_3 where first introduced by Tvergaard to bring the model prediction into closer agreement with the experimental results for deforming porous materials containing cylindrical or spherical voids. Tvergaard suggests a value for q_1 in the range of 1.5 to 2.5, whereas q_2 equated to unity improves the accuracy of numerical results when compared to the experimental data for several powder compacts [114]. It is important to mention that the parameters q_1 and q_2 are described as an internal state variable and are an attempt to capture the influence of pore shape. Several researchers have attempted to understand the Gurson-Tvergaard parameters, however only a few have attempted to estimate the values for porous titanium material undergoing large plastic deformation [12, 43, 115].

To determine the effect of the Gurson-Tvergaard model parameters on the relative density distribution we compare three different scenarios. In the first scenario we assume q_1, q_2 and q_3 are equal to one. When the scalar parameters are equated to unity the material model reduces to a basic Von-Mises criteria with porosity. In the second scenario we use the parameters suggested by Tvergaard to take into consideration the effect of spherical or cylindrical voids. In the third scenario we empirically determine the Gurson-Tvergaard parameters by carrying out an inverse iteration procedure introduced by Cheng et. al. [13].

The computation algorithm for determining the Gurson-Tvergaard parameters are illustrated in figure 5.1. A least square approach was followed to formulate the objective function in terms of Tvergaard parameters. The objective function is given in equation 5.1;

$$Fun\ (q_j), = \sum_{i=1}^{N}[\boldsymbol{\phi}(\sigma_i, f_i)]^2] \qquad j\text{=1-3;} \tag{5.1}$$

where, σ_i and f_i are one set of data for each of the scalar parameters values from q_1 to q_3. An initial Gurson-Tvergaard parameter was assumed to be equal to one and the subsequent parameters were calculated by iteration based on the above equation. An error tolerance criterion was specified according to equation 5.2:

$$\left|\frac{q_{j_s}}{q_{j_p}} - 1\right| \leq \text{Error tolerance, j} = 1 - 3 \qquad 5.2$$

where, q_{j_s} is the temporarily updated value by substituting the previous value of q_{j_p}.

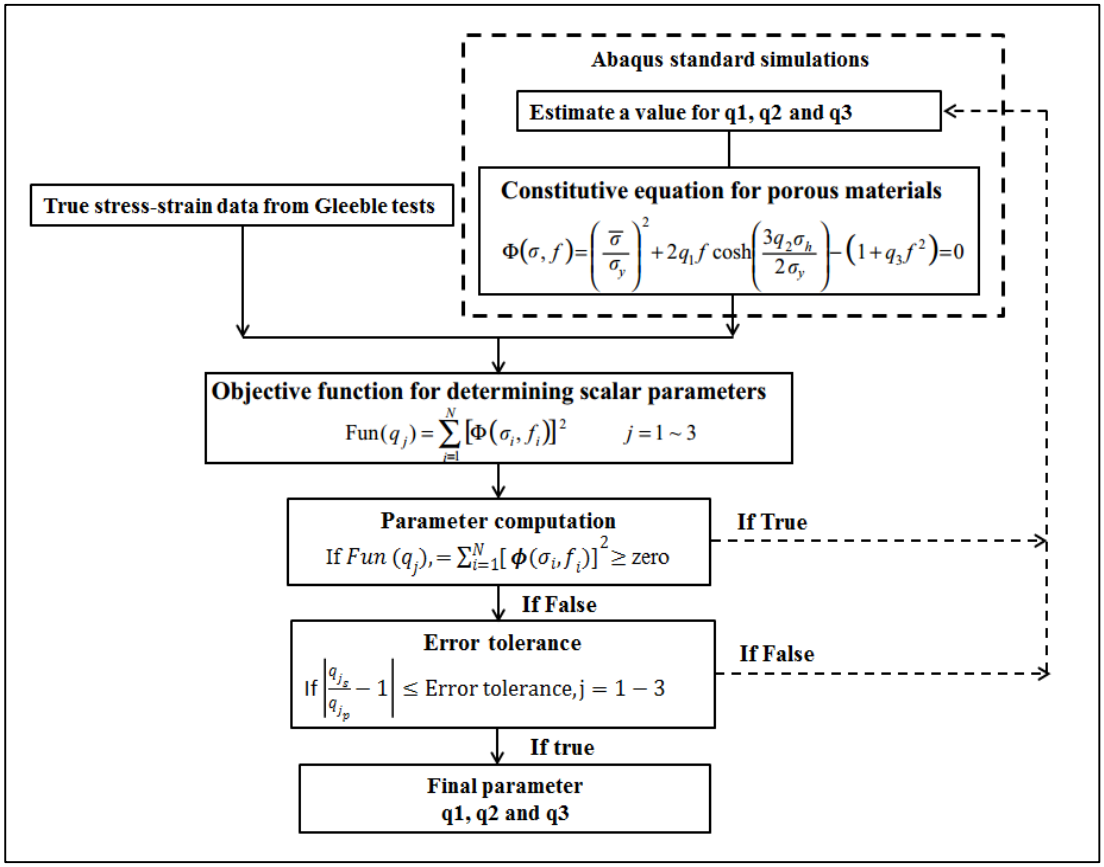

Figure 5.1: Computation algorithm for fitting experimental data with simulated results

Three initial powder compact temperatures were considered in the simulation according to the Gleeble compression test conditions. The samples were compacted and induction sintered to 75 % of full density and cut into Ø 8.2 mm × 12.8 mm cylinders. A graphite lubricant was used on both surfaces of a sample to reduce friction. Figure 5.2 shows the true stress-strain data obtained from compression tests.

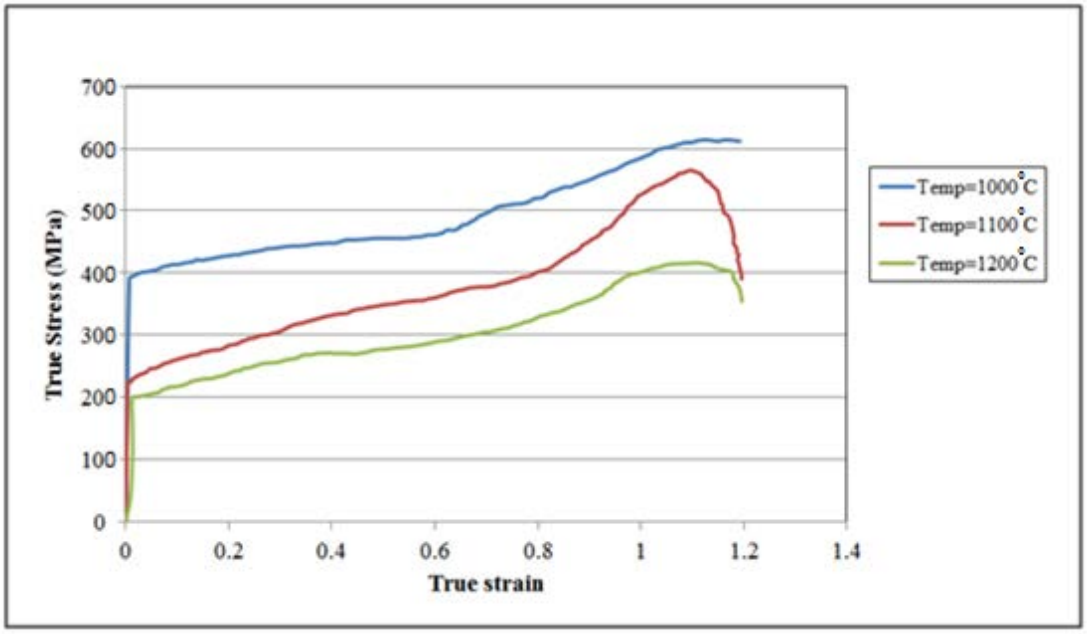

Figure 5.2: True stress-strain curves for HDH titanium powder compact obtained by Gleeble compression tests at a strain rate of 1/s

The measured relative density after the Gleeble tests was nearly 99 %. An axisymmetric model was created in Abaqus standard with CPE4T elements as shown in figure 5.3. The initial material model was defined with the flow stress data obtained for 75 % porous material and initially estimated Gurson-Tvergaard parameters. A frictional coefficient value of 0.1 was used throughout the simulation. The computation was carried out manually using an excel spreadsheet.

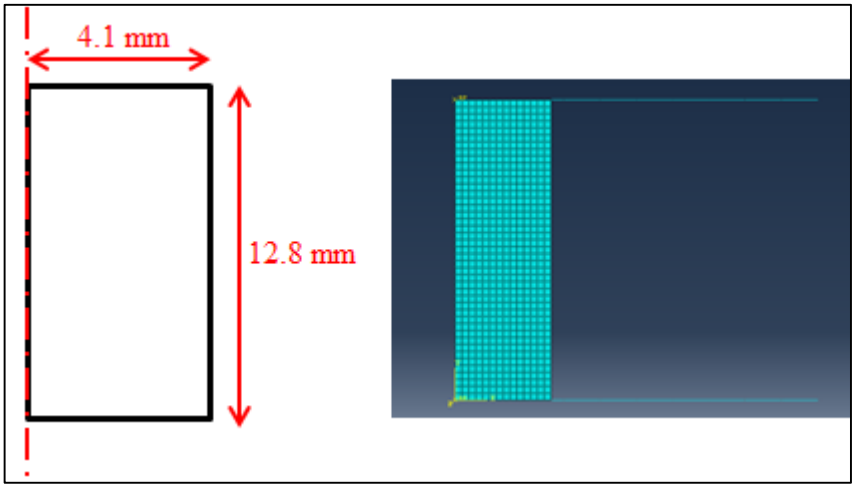

Figure 5.3: Axisymmetric model for model parameter computation

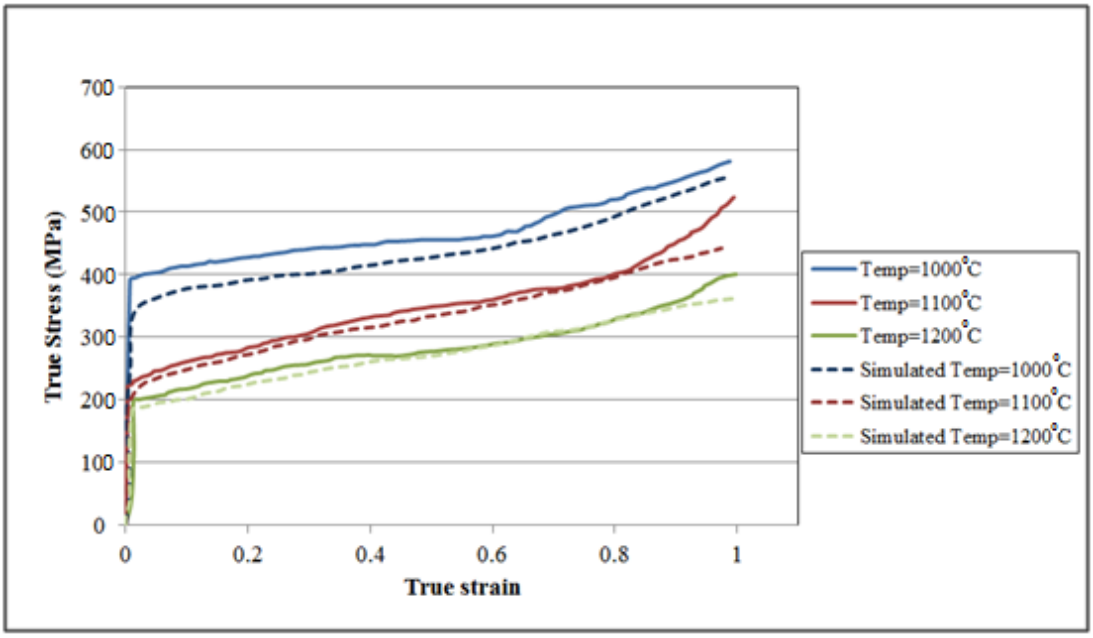

Figure 5.4: A comparison of true stress-strain curves at different initial temperatures obtained experimentally and by simulation with q1=1.7, q2=1.2 and q3=2

A total of 24 iterations were performed to determine the values of the Gurson-Tvergaard parameters that closely match the experimental true stress-true strain data as shown in figure 5.4. It is observed that the model parameters had a significant effect on the plasticity or flow behaviour of the porous material. The parameters q_1 and q_2 had the most influence on a stress-strain curve for compressive loading; the influence of parameter q_3 was relatively insignificant. Both large and small values of q_1 and q_2 had an effect on the numerical stability in the simulation. Thus, an error tolerance was specified for q_1 between 0.5 and 2; for q_2 between 0.8 and 1.8 and for q_3 not to exceed more than 3. After iterations the final Gurson- Tvergaard parameters for porous HDH titanium at 75 % full density and undergoing hot compression were found to be: q_1= 1.7, q_2= 1.2 and q_3 = 2.

The procedures were repeated to determine the Gurson-Tvergaard parameters for 75% dense HDH Ti-6Al-4V alloy powder compacts. The Gurson-Tvergaard parameters which gave the best fit with the experimental data were found to be q_1= 1.2, q_2= 0.8 and q_3 = 1.5. Compared to HDH titanium, typical true stress values were higher for a Ti-6Al-4V alloy.

5.1 Assumptions made in the parameter determination

It must be noted that the above procedures are based on the following assumptions;

- The friction is constant during the tests.
- The true stress-strain curves obtained by Gleeble tests were sufficiently accurate.
- The density was homogeneous prior to testing, uniform heating occured and die chilling effects were neglected due to the small size of the sample.

5.2 Gurson-Tvergaard model parameters and void geometry

Both the Gurson and Gurson-Tvergaard models are based on the assumption that the voids are spherical or cylindrical. However, in reality void shapes can be quite irregular, as in a titanium powder compact. Also, thermo-mechanical processing, such as powder forging, can exacerbate the void geometry. Budiansky et. al. [116], in earlier work, analysed the shape changes of voids located in a viscous and visco-plastic material undergoing plastic deformation. Further expanding this concept Gologanu applied his ideas to non-spherical pore shapes in combination with an ideal plastic material model [117]. The effect of void shape irregularities was dealt with by defining a shape parameter and this approach predicted a relative density distribution which agrees more closely to experiment [117, 118].

The change in void shape in a titanium powder compact depends on the following factors;

- powder morphology (spherical or irregular powders),
- compaction pressure,
- induction sintering temperature,
- heating rate and holding time,
- forging temperature and cooling rate.

5.2.1 Void geometry and evolution during powder forging

The micrograph in figure 5.5 shows the void shape and its distribution in a fully dense titanium matrix after compaction and forging using HDH titanium powder.

The porous powder compacts illustrated in figure 5.5 were prepared from HDH titanium powder of size 200 mesh. The powder had irregularly shaped particles which promoted mechanical interlocking between the particles during compaction.

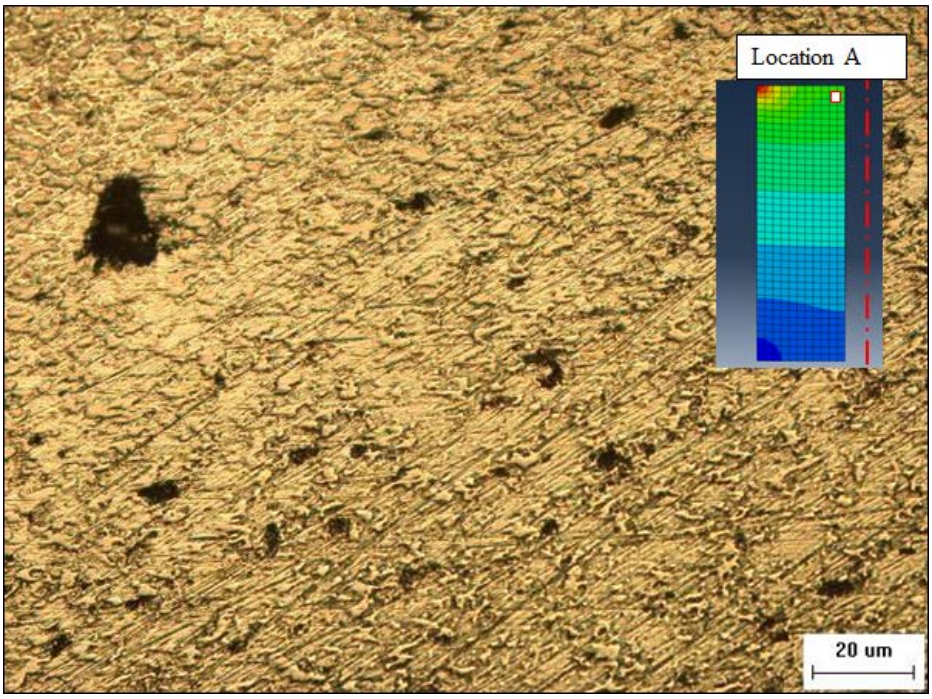

Figure 5.5: Micrograph showing pore geometry for HDH titanium at location A after compaction at 140 bars

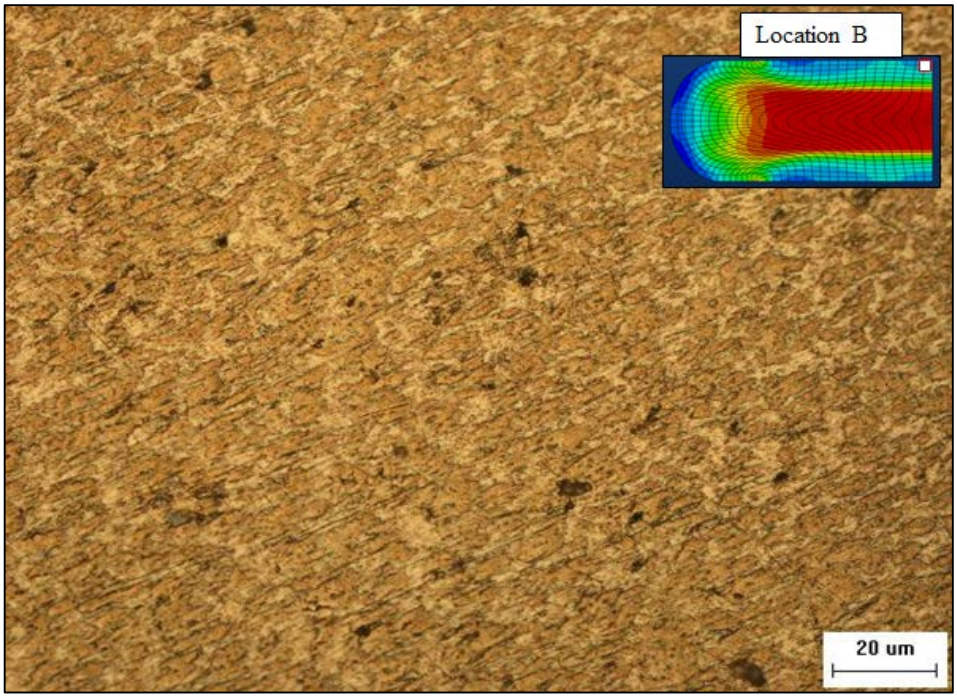

Figure 5.6: Micrograph showing pore geometry for HDH titanium at location B after powder forging at 1250° C.

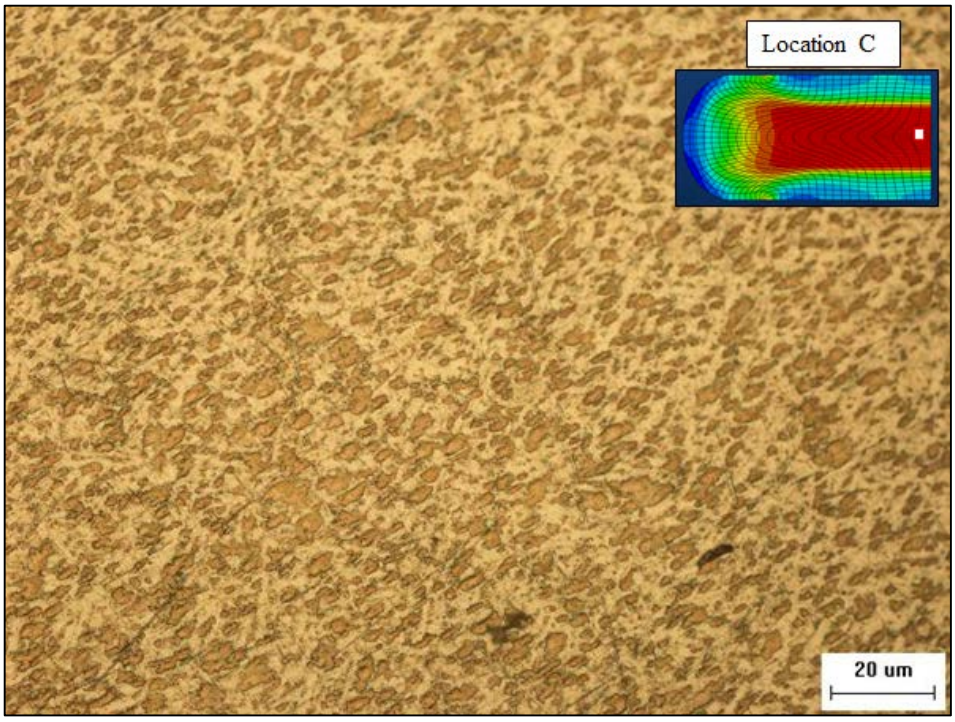

Figure 5.7: Micrograph showing pore geometry for fully dense HDH titanium at location C after forging at 1250° C

Metallographic examination showed that the change in pore shape before and after forging followed an expected trend. It must be noted that a significant difference exists between the pore geometry observed under the micro-scope and the assumption in the Gurson model that pores have a spherical shape. It is evident that during uniaxial

upsetting many pores changed shape and were significantly flattened by the compressive stresses. In the central region of a deformed part the material is fully consolidated because of a total collapse of the pores.

From the perspective of numerical simulations, not many models exist that take into account pore shape geometry evolution during the consolidation process. However it is worth noting that there is a direct relationship between the rate of densification, the initial pore geometry and the orientation of pores with the direction of load application. Micro-graphically it is observed that material obtained after compaction and sintering tends to have a cusp-shaped pore geometry at lower densities. Depending on the direction of load application, as the density increases the pores flatten and change to a more ellipsoidal shape. Budiansky et. al. [116] proposed that for a linear creeping material under conditions of high load tri-axiality (compression and hydrostatic loading), the spherical voids initially collapse to a point purely as a result of the uniaxial loading and then flatten to a crack-like shape, as found in this work. Budiansky et. al demonstrated that the void shape evolution was also a function of the mode of loading and material non-linearity. Budiansky et. al. noted that the time to densify porous bodies is significantly shorter under uniaxial compressive loading compared with hydrostatic or constrained compression. However the magnitude of the densification rate depends on the instantaneous pore geometry. Similar observations were made by Lee and Mear [119]. Thus, in practice pore shape evolution under deviatoric loadings is a contributing factor in the calculation of densification rate. For predicting densification, the Gurson model in the original form does not take into account the pore shape changes taking place during hot upsetting. However, a satisfactory solution could be obtained by two different methods proposed by Ponte Castaneda and Zaidmann [120] and Cheng et. al [13]. In the method used in this work, a much simpler approach was followed in which the Gurson model was modified by experimentally fitting the Gurson-Tvergaard parameters to represent the stress-strain data directly obtained from Gleeble tests.

5.2.2 Void distribution and material anisotropy

To understand the pre-existing void distribution and material anisotropy after compaction and powder forging, optical microscopic analysis was done. HDH titanium and Ti-6Al-4V powder compacts were prepared with a target relative density of 0.75 to observe the void distribution. The samples were cut at location specified in figure 5.8. Although established techniques exist for metallographic preparation of fully dense titanium and Ti-6Al-4V, polishing low density powder compacts was a challenge. However, multiple low temperature (150 ^{o} C to 200 ^{o} C) curing cycles helped in obtaining relatively good results for HDH titanium, but this technique proved unsuccessful for polishing Ti-6Al-4V powder compact samples. Thus the micrographs of the porosity distribution shown in figure 5.8 were obtained after compaction and induction sintering with a holding time of 5 minutes. It must be noted that after induction sintering, observed void geometry and distribution can alter significantly from that expected after compaction. However the micrographs of induction sintered samples were good enough to show the general trend of void distribution in that particular alloy.

Figure 5.9 and figure 5.10 show the void distribution in HDH titanium and HDH Ti-6Al-4V alloy after forging. It can be seen that after compaction there is a non-uniform distribution of voids in the powder compact. It is well known that under single stage cold compaction the highest relative density is obtained at a top corner of a compact and the lowest is achieved at the bottom of a compact. This trend is quite visible from the void distribution in the compact. It is interesting to note that the voids at the bottom corners were quite large. After forging HDH titanium, the voids at the centre had collapsed and the material tended to be fully dense titanium.

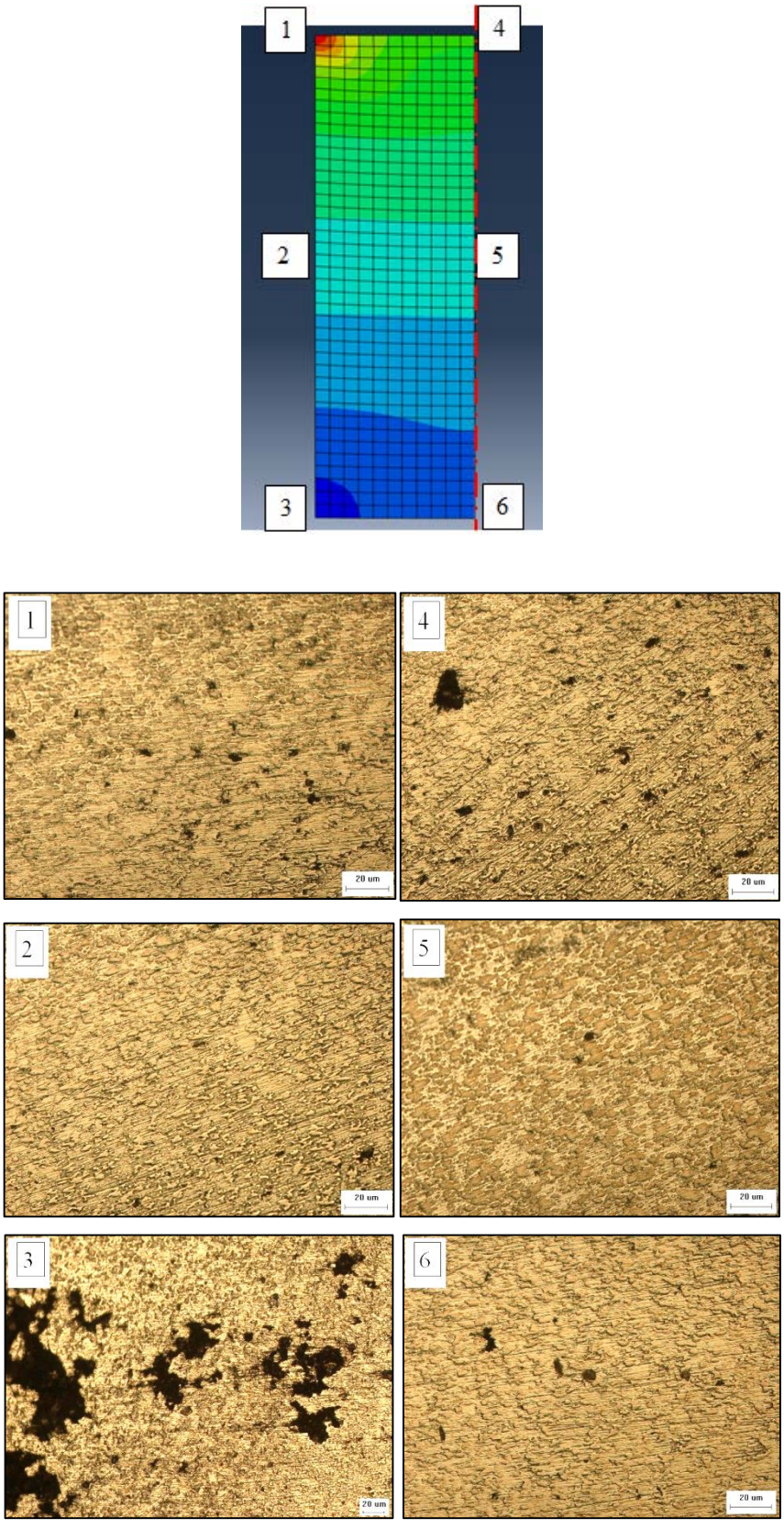

Figure 5.8: Micrographs showing the porosity distribution after compaction for HDH titanium

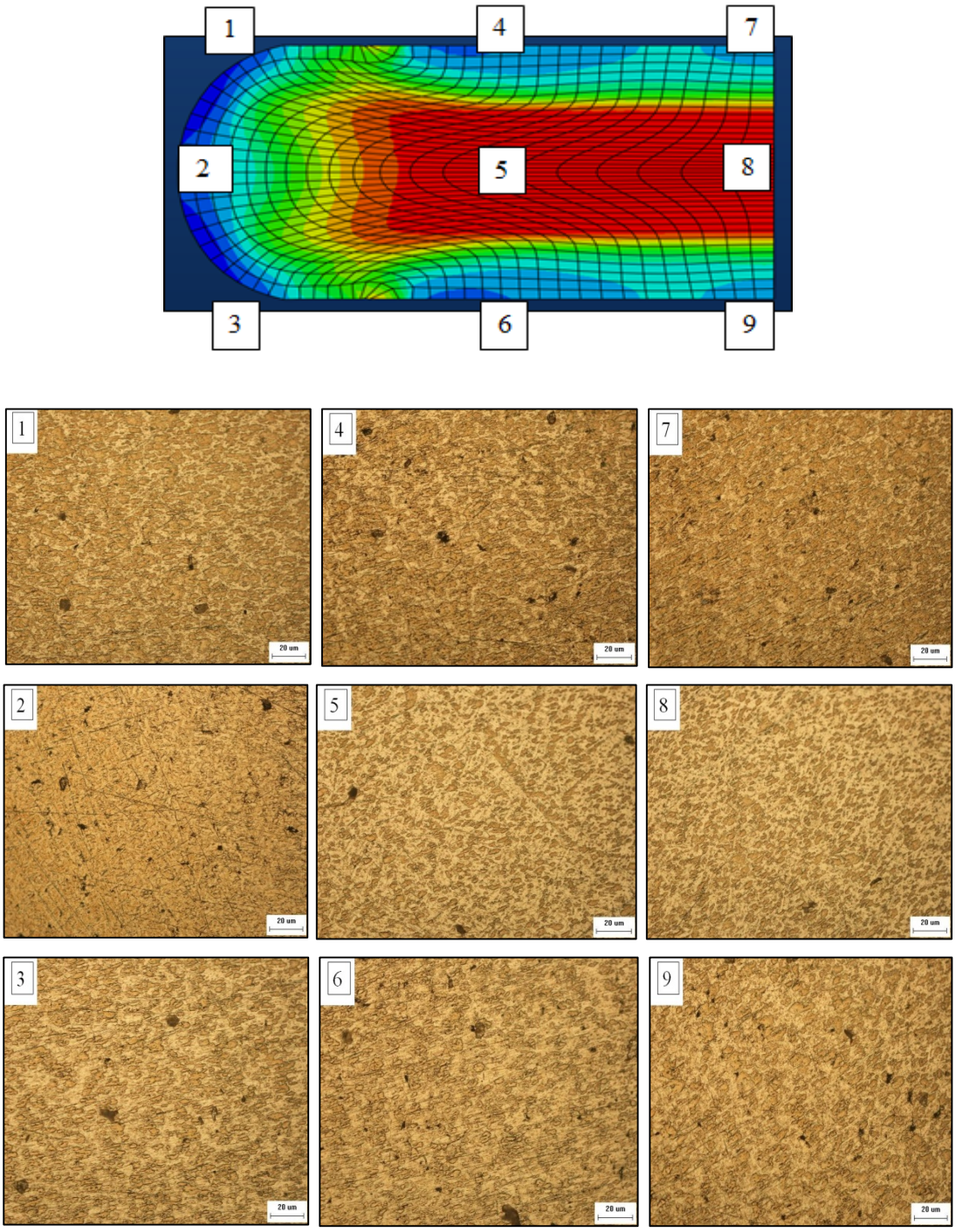

Figure 5.9: Micrographs showing the porosity distribution after powder forging at 1250º C for HDH titanium

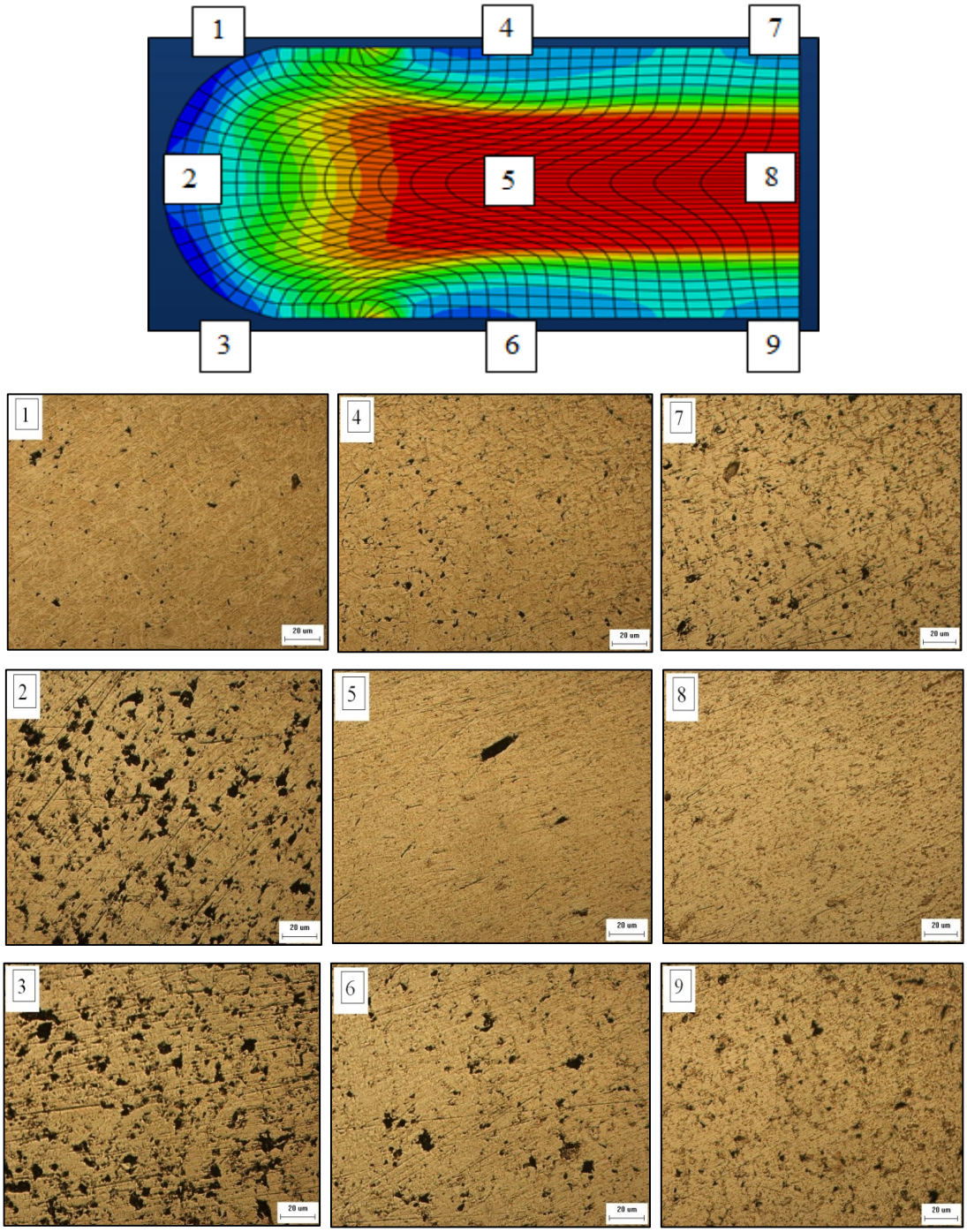

Figure 5.10: Micrographs showing the porosity distribution after powder forging at 1250º C for Ti-6Al-4V alloy

5.3 Summary

The main aim of this chapter was to determine the Gurson-Tvergaard parameters that best represent porous material. These parameters improve the accuracy of simulation results as they capture the influence of pore geometry on densification. These parameters relate internal state variables of the material with the flow stress.

- A computational algorithm has been developed to determine these parameters by an inverse iteration procedure. The Gurson-Tvergaard parameters for HDH titanium powder with particle size of 200 μm are determined as $q_1 = 1.7$, $q_2 = 1.2$ and $q_3 = 2$. Whereas for HDH Ti-6Al-4V powder they are determined to be $q_1 = 1.2$, $q_2 = 0.8$, and $q_3 = 1.5$.
- An important assumption made in both the Gurson and Gurson-Tvergaard models is that the pores are circular or cylindrical; however in reality pores are irregularly shaped, which is confirmed by optical microscopy. Optical micrographs show that there is a change in void geometry after powder forging.
- Micrographs taken at different locations in a powder compact show that the porosity distribution is non-homogeneous and irregular. After powder forging the porosity collapses at the centre of a forged compact, whereas at the edges it becomes more marked.

6 Powder forging experiments and validation

Introduction

The powder compaction and forging experiments were carried out using a 100 tonne hydraulic press machine, shown in figure 6.1. For upsetting experiments, the powder was formed into a powder compact using a powder compaction die using the conditions explained in the subsequent section. Powder compaction was done using the same compaction pressure to give a consistent initial relative density. HDH titanium powder compacts were produced with HDH titanium powder and Ti-6Al-4V powder compacts were produced using a blended elemental approach with HDH powder blended with the Al-V master alloy powder.

Figure 6.1: 100 Tonne hydraulic press with forging dies assembled

Powder compaction was carried out using a single stage compaction die as shown in figure 6.2. The experimental procedure for both compaction and powder forging is given below.

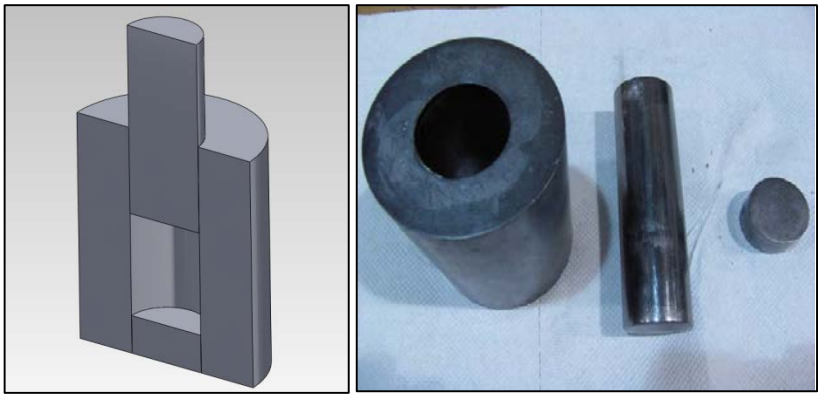

Figure 6.2: Single stage compaction dies

6.1.1 HDH titanium powder compaction

The powder compact size required for powder forging experiments was Ø 40 mm × 40 mm and the required mass of powder was first calculated according to the volume occupied by loose powder in the die. This calculated amount, equal to 180 grams of powder, was transferred to the die which was at room temperature and the powder level made even by tapping the die to ensure that the die filled equally. Finally, the powder was pressed using a pressure of 140 bars and was held for 2 minutes to produce the final powder compact. To maintain consistency and repeatability, the same procedure was followed for all the powder compacts used in this work. It is worth mentioning that the relative density of a powder compact is a function of the applied pressure, the mass of powder and the die temperature, in other words the relative density can be improved by varying any of these parameters. Figure 6.3 shows the relative density vs. compaction pressure for HDH titanium powder. The final relative density of powder compacts was found to be 0.75 for an applied pressure of 140 bars; however it was impossible to quantify the overall relative density variation within the powder compact, thus an assumption was made in the simulation that the initial relative density of a powder compact was uniform before powder forging.

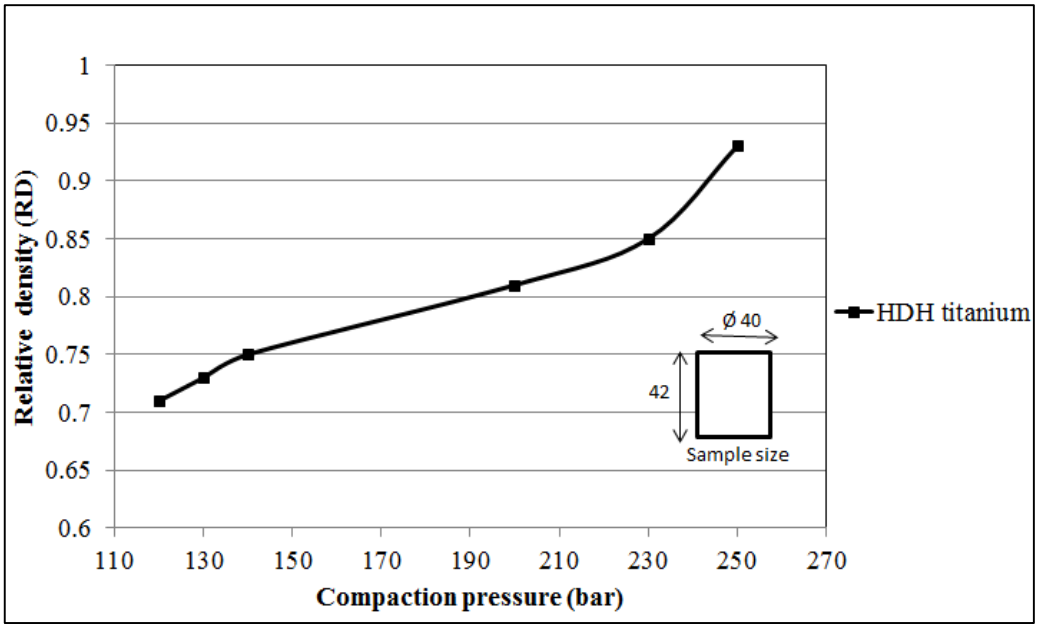

Figure 6.3: Relative density vs. compaction pressure for HDH titanium powder

During the cold powder compaction experiments the holding time had little effect on the final relative density. A holding time of more than 2 minutes led to central cracks in a powder compact during ejection. On the other hand a lower holding time led to excessive spring back after ejection.

6.1.2 Ti-6Al-4V powder compacts

The procedure for producing Ti-6Al-4V powder compacts was similar to that for the production of HDH titanium powder compacts, however HDH Ti-6Al-4V required a higher compaction pressure for achieving the target density, due to its high initial yield strength and the cohesive nature of the powder. Figure 6.4 shows the relative density versus compaction pressure during cold compaction for Ti-6Al-4V powder.

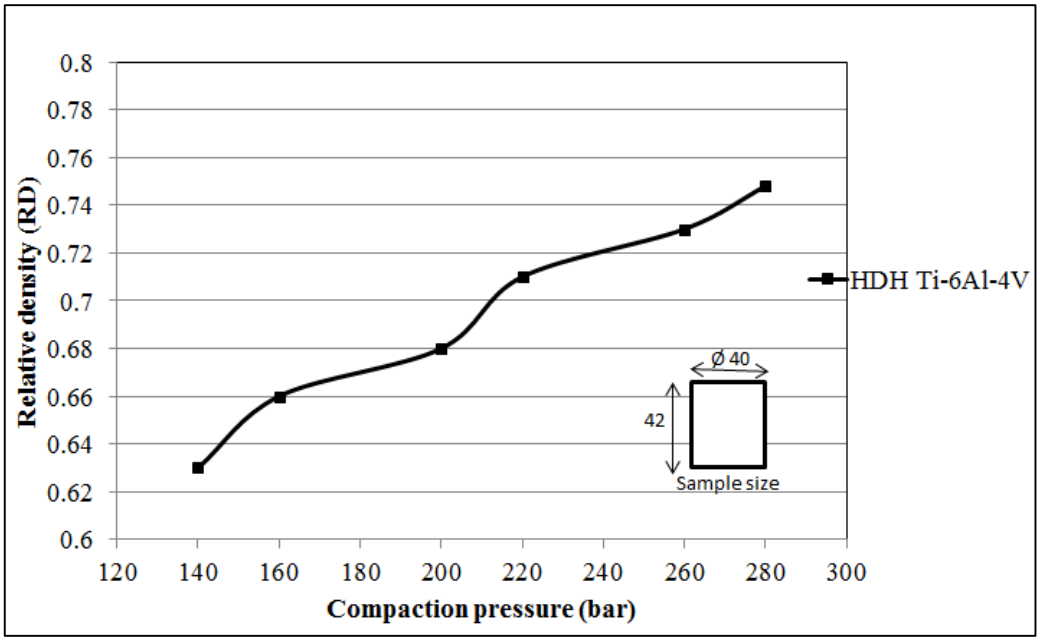

Figure 6.4: Relative density vs. compaction pressure for Ti-6Al-4V alloy powder

It must be noted that a higher relative density for Ti-6Al-4V powders may be obtained by warm powder compaction; however in this study the required density was achieved by cold compaction alone. The height of a powder compact reduces with increasing compaction pressure; however the target compact height was preselected to be 42 mm for consistency with the simulation trials. The 'spring-back' effect in Ti-6Al-4V powder compacts was seen to be up to 3 mm after 5 minutes of ejection time. In order, to achieve the required height and diameter for the powder forging, the compaction pressure and holding time needed to be adjusted. Increasing the holding time of the powder compact in the compaction die significantly reduced the spring-back effect, however on increasing the holding time above 5 minutes, cracks were seen in the powder compact. During experiments based on a trial and error approach, a holding time of 2 minutes was selected to achieve powder compact samples of the required size, according to the experimental plan.

6.2 Powder forging experiments for producing circular discs

Figure 6.5 shows the die setup for circular disc powder forging experiments. The dies were made of H13 tool steel with the forging surface polished. A thin layer of graphite lubricant dissolved in water was applied at the die surface. Thermocouple holes Ø2 mm were located at 5 mm from the forging surface and Type K thermocouples were

used to monitor the die temperature. A ceramic band heater was used to heat the die to the required temperature and the heating was controlled by the temperature probe located in the bottom die. Both the top and the bottom dies were heated together to the equilibrium temperature defined by the experimental settings.

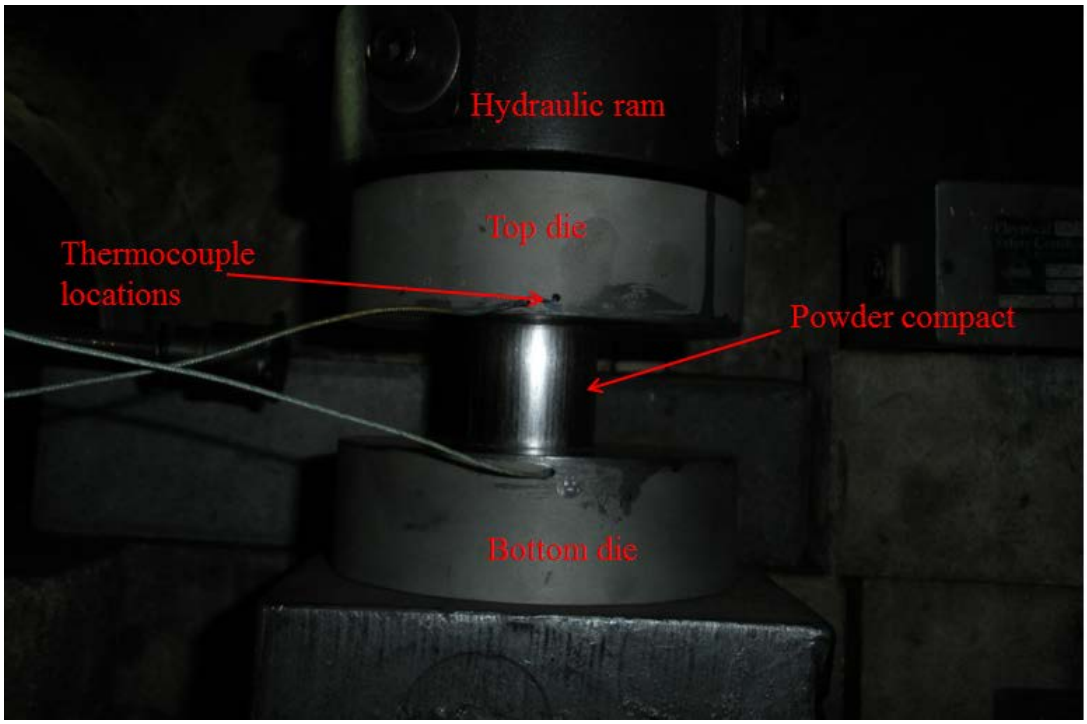

Figure 6.5: Forging dies for titanium disc forging

Before starting the experiments, the chamber was evacuated and filled with argon gas to a point where the percentage of oxygen was below 0.5 ppm. The powder compacts were heated in an argon atmosphere using an induction furnace, as shown in figure 6.6. For uniform heating, a powder compact was precisely located within the induction coil at a distance of 10 mm from the bottom and 35 mm from the top. A refractory ceramic support was used to ensure that no heat was lost from the bottom of a compact.

Figure 6.6: Powder compact heating within the induction coil

A 5 mm hole was drilled at the top of a compact for locating a type K thermocouple and the temperature of a powder compact was measured in-situ using a data logger connected to the thermocouple. The heating rate and time were monitored during induction heating and for consistency, these were kept the same for all forgings. A 5 minute holding time at temperature was used before forging and the time taken to transfer powder compacts from the induction furnace to the forging die was less than 4 seconds. It was important to minimise the transfer time as a considerable amount of heat is lost during transfer to the die. After transferring the billet to the die, full load was applied to the hydraulic ram until 50 percent deformation was indicated by the stopper blocks.

Figure 6.7: (a) Powder compact before forging, (b) forged circular discs

6.3 Experiments

The purpose of these experiments was to evaluate the influence of initial temperature on the final relative density of a powder compact and to compare this to the results obtained numerically. These experiments were carried on for both HDH titanium and Ti-6V-4V alloy with an initial relative density of 75 percent. Though there are several parameters (holding time, interfacial friction and deformation strain rate) that influence material densification, the initial compact temperature and the degree of deformation are crucial parameters for the validation of the Gurson-Tvergaard model.

6.4 The influence of the initial forging temperature on the relative density prediction by the Gurson and Gurson-Tvergaard models

Table 7 shows the experimental conditions followed. The target relative density for all the samples after compaction was 0.75, however after compaction there was a slight variation in the measured relative density as shown in table 7. It must be noted that, despite an aim for a consistent 50 percent deformation during the experiments, the sample T63 was over-deformed by 3 percent due to slippage of the stopping block. All the samples were compressed at a pre-set ram velocity of 7 mm/ sec.

Material	Sample Id	Forging temperature	Die temperature	Holding time	Initial relative density	Percentage reduction
HDH titanium	CP1	1250 °C	100 °C	300 sec	0.752	50 %
	CP2	1100 °C	100 °C	305 sec	0.743	50 %
	CP3	1000 °C	100 °C	301 sec	0.751	52 %
HDH Ti-6Al-4V	T61	1250 °C	100 °C	301 sec	0.741	50 %
	T62	1100 °C	100 °C	308 sec	0.738	50 %
	T63	1000 °C	100 °C	304 sec	0.754	53 %

Table 7: Experimental plan

6.4.1 Experimental result

Figure 6.8 shows the circular discs obtained after powder forging HDH titanium and HDH Ti-6Al-4V at the different temperatures shown in table 7. It can be seen that for initial forging temperatures of 1250^{o} C, 1100^{o} C and 1000^{o} C no cracks were detected in HDH titanium discs. However, for HDH Ti-6Al-4V, cracks were visible even when forged at a temperature at 1250^{o} C. The degree of cracking worsens when the alloy is forged at the lower temperatures of 1100^{o} C and 1000^{o} C. This indicates that, even with a low initial relative density of 0.75, HDH titanium powder compacts can be still workable, while Ti-6Al-4V is not. This may be due to greater sensitivity of temperature on flow stress for Ti-6Al-4V alloy when compared to HDH titanium.

Figure 6.8: Circular discs forged at different experimental conditions

It is interesting to point out that Ti-6Al-4V alloy is known for its strain-rate sensitivity, especially during non-isothermal forging used in these experiments, where the heat losses were higher. Larger strain rates are generally favourable to compensate strain rate sensitivity effect and heat loss during deformation. Strain-rate does have an effect on the rate of densification in both HDH titanium and Ti-6Al-4V alloy, however the limited capability of the hydraulic press used in this work precluded any strain-rate sensitivity analysis. Also, reductions in temperature from the initial compact temperature, because of heat losses to the dies are important factors which need to be taken into account when validating experimental results with simulated results in the present work.

Because of the heat losses from the Ti-6Al-4V alloy to the die during closed die forging, it is possible that at certain regions within the part the temperature might be below 1000^{o} C. This can lead to cracking during forging of complex shapes. Thus powder compact forging with HDH Ti-6Al-4V, with the current initial relative density is not recommended. From a practical perspective it is possible to improve the initial relative density of HDH Ti-6Al-4V powder compact using a better compaction

method such as warm powder-die compaction, CIPing, vacuum sintering, spark plasma sintering or high velocity compaction (HVC) [43, 121-123].

6.4.2 Predicting the influence of the initial powder temperature on relative density using the Gurson and Gurson-Tvergaard models

Figure 6.9 shows the density distribution in a forged part at three initial temperatures using the two models. Comparing the predictions of the original Gurson model and the Gurson-Tvergaard model significant differences can be observed. The Gurson-Tvergaard model predicts a higher densification at all the three temperatures. This is expected and is due to the fact that the model captures the effect of porosity collapse and the degradation of a materials stress capacity during deformation. Simulation with both material models shows no significant change in the final geometry. However, at 1000^{o} C there are fewer higher density regions shown in figure 6.9 compared with an initial temperature of 1250^{o}C.

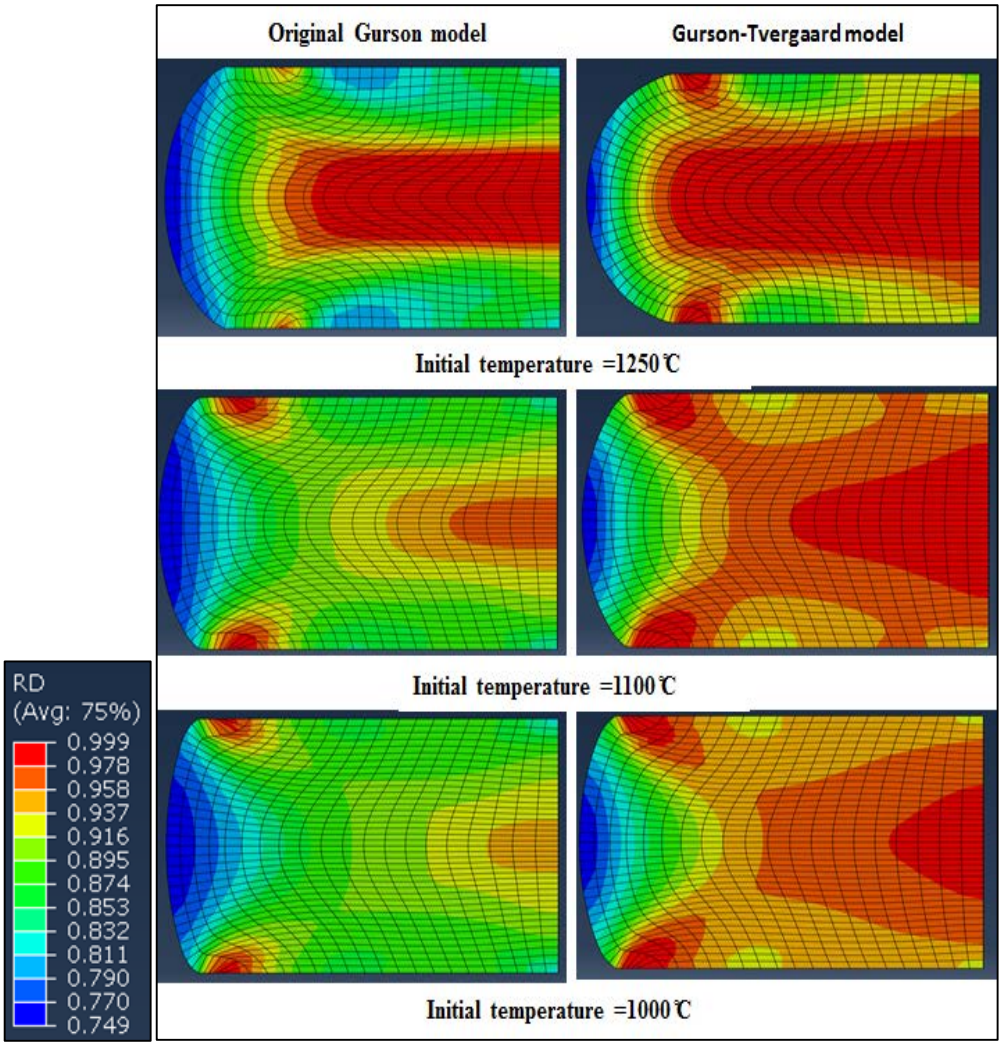

Figure 6.9: Relative density distributions at various initial temperatures for HDH titanium forged parts

From figure 6.10 it can be seen that at initial temperature of 1250^{o} C, both models predict similar density profiles. The highest densities in all cases were observed at the centre. In general the relative density distribution showed a direct relationship with increasing initial temperature. For practical considerations, it is advisable to forge HDH titanium and Ti-6Al-4V powder compacts at a higher temperature to obtain a higher uniform relative density distribution.

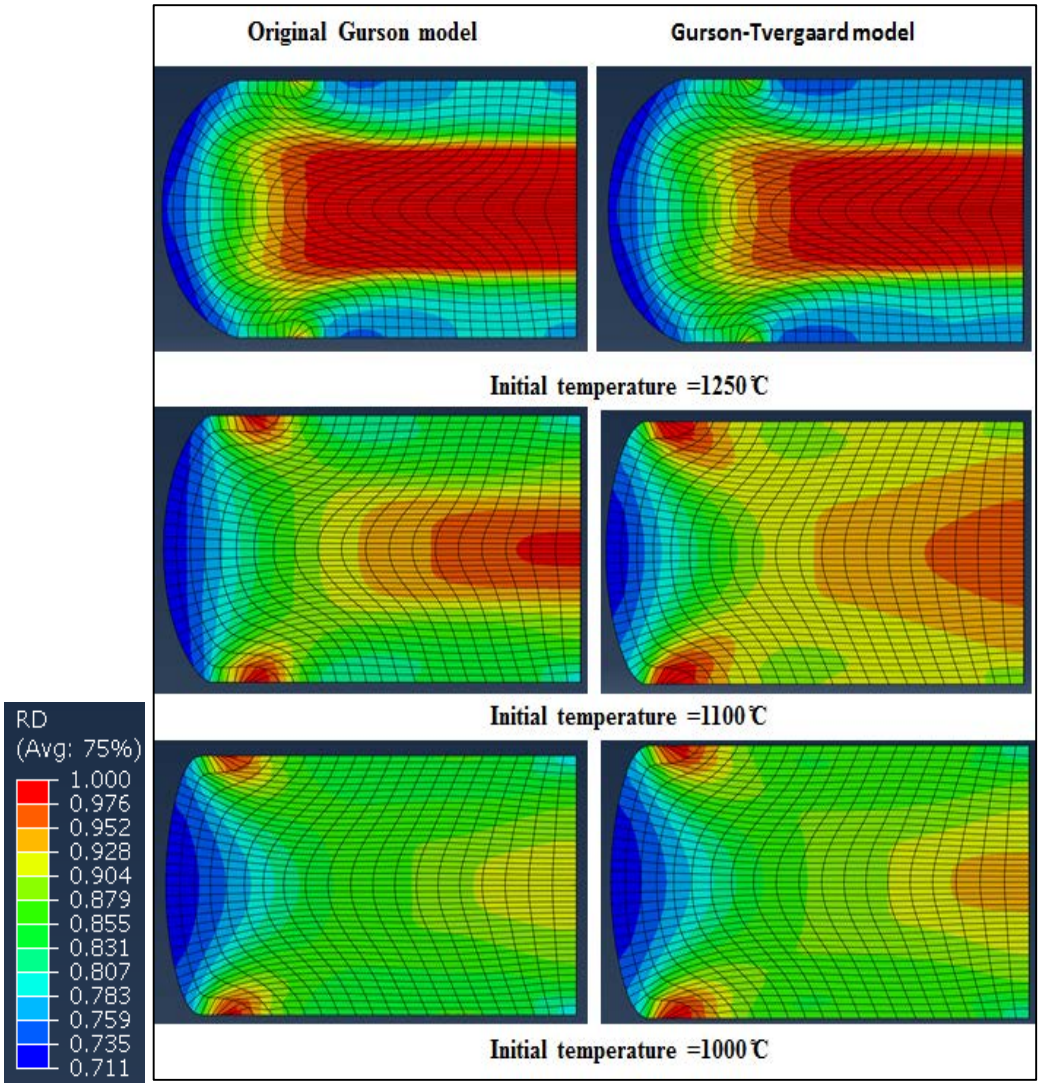

Figure 6.10: Relative density distributions at various initial temperatures for HDH Ti-6Al-4V titanium forged parts

Simulation results also highlighted the temperature dependence of the flow stress at elevated temperatures. In all cases the central part of a powder compact remains at high temperature. It must be noted that the material yield stress of a powder compact is dependent on the differences in density at different degrees of plastic strain. However, in this analysis a direct method is used where a constant velocity was applied to the top die. The equivalent plastic strain and the evolution of density are calculated depending on the yield stress of the deforming material at various temperatures.

The values q_1 and q_2 defined in the Gurson-Tvergaard model take into account the internal variables representing the influence of porosity as determined by a best fit with the flow stress data. The values for these parameters influence the tri-axiality

levels within the material. Figure 6.11 shows the density evolution at the investigated temperatures using the Gurson and Gurson-Tvergaard model at the central node. A significant difference was seen between the two models in terms of densification rate and the final density obtained at the same level of plastic strain. At lower temperatures a slower densification was observed with the original Gurson model. With the Gurson-Tvergaard model the densification rate was highest at an initial temperature of 1250 ^{o} C; as a result the final density at the end of forging was highest. The densification rate obtained with the Gurson model at 1100^{o} C and 1000 ^{o} C was significantly lower than at 1250 ^{o} C.

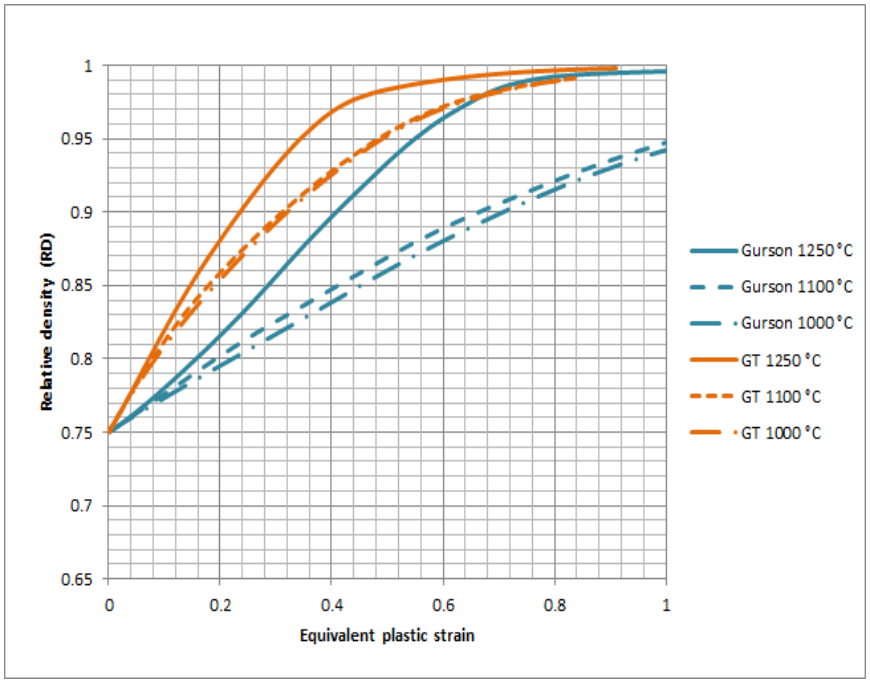

Figure 6.11: Equivalent plastic strain vs. Relative density comparison

Though the densification rate is significant for analysing the effect of a particular constitutive model, in practice it also indicates that the material needs to deform further to enhance densification.

6.5 Relative density measurements

Several methods are available for measuring the relative density in a metal powder part. Archimedes' principle is one of the common methods used to measure relative density of porous materials with a high level of open porosity. The method works on the principle that when an object is immersed in liquid, the hydrostatic forces in the

liquid exert buoyant forces proportional to the volume of the part. The density measurement procedure using Archimedes' principle is a recommended method standardised by ASTM B 328 [124], MPIF test method 42 [125] and ISO 2738 [126]. The limitation of this method is that it is not capable of capturing local density variations, as the part needs to be cut into smaller sections and some of the material is lost during the cutting process.

Weber and Brown [127] and Riera and Prado [128] developed a method to characterise local density variation by using micro-hardness testing and correlating density with hardness. Wagle et. al. [102] measured localised relative density by machining pre-sintered powder compacts and establishing a relationship between the volume of material removed and relative density. However, due to constraints in machining the relative density was determined only for a part of the powder compact.

Various researchers have previously demonstrated non-destructive relative density evaluation techniques such as metallographic image processing, an electrical resistivity test, gas permeability tests, an ultrasonic test, an eddy current test, X-ray radiography and gamma-ray density measurements. Despite the popularity of non-destructive testing (NDT) in the P/M industry, each technique has its limitations. For example ultrasonic testing is seldom precise because the low density powder compacts strongly attenuate the elastic waves. Eddy current methods encounter a limited field to medium interaction problem for powder compacts because a random particle distribution gives low electrical conductivity and poor reproducibility of measurements. X-ray imaging, despite being popular for sub-surface flaw detection, is not useful in locating micro-surface cracks or near corner cracks. Table 8 shows different techniques used to determine relative densities. In this work, a γ-ray density determination technique was used and this will be discussed in detail.

Method/ Principle	Measured/ detected	Advantages	Disadvantages
Archimedes method	Bulk density, open porosity, relative density.	Simple operation and low cost	Low accuracy, time consuming, cannot capture density variation and localised relative density.
Metallography and image processing	Localised relative density, variation of density, open and closed porosity, surface cracks.	Simple operation, low cost, high resolution.	Time consuming, cannot capture density variation.
Electrical resistivity	Localised relative density, can detect subsurface cracks and density variations.	Low cost, portable and easy operation.	Sensitive to surface imperfections
X-ray imaging	Localised relative density, variation of density, sub-surface cracks	Accurate and fast, suitable for low relative density measurement	Radiation hazard, sensitive to internal defects
Eddy current method	Localised relative density, density variations,	accurate, reliable and fast	Time consuming, test samples preparation required
Ultrasonic method	Localised relative density, density variations ,surface cracks, sub-surface imperfections etc.	Reliable, accurate and repeatable	Time consuming, test samples preparation required
γ-ray technique	Localised relative density, captures density variations.	Moderate cost, accurate, reliable and repeatable, suitable for thicker samples, suitable for powder compacts as well as sintered parts.	Radiation hazard; Accuracy depends on calibration with fully dense material.

Table 8: A comparison of different density measuring techniques

6.5.1 γ-ray density measurement

A gamma particle densitometer developed by GAMMATEC GmbH was used to determine the localised densities in the titanium powder compacts. This method can measure the densities of powder compacts that are partially or fully dense with sufficient accuracy, which is difficult to achieve by other techniques such as Archimedes' method. The equipment measures the amount of absorbed radiation where the degree of absorption of gamma rays depends on the density of the material. Figure 6.12 shows a schematic of a gamma particle densitometer provided by GAMMATEC. The device consists of a gamma ray source mounted inside a shielded container that emits radiation. The radiation emerges though a carefully directed

opening in the bottom of the shielding container and then passes through the sample powder compact, where it is partially absorbed. An aperture with a known dimension on the top of the detector screens-out the beam of radiation and the radiation passing through this is measured. The size of the aperture can be circular or segmental and is defined by the volume and shape of the test sample to be analysed. The intensity of the radiation detected by the detector is calibrated in terms of density.

From a simulation point of view this technique is quite favourable when parts exhibit localised density variations which are predicted by powder compaction or forging simulation results. The method also allows for the determination of local densities, especially at regions where the highest loading or densification takes place.

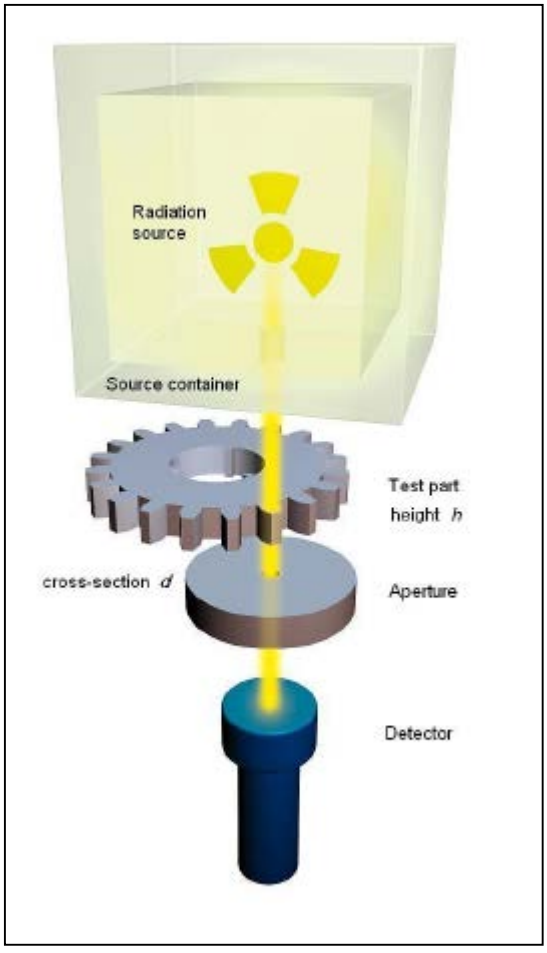

Figure 6.12: A schematics of a gamma ray densitometer [129]

6.5.2 Sample preparation for density measurement

An advantage of a gamma ray densitometer is that large sectional test samples can be analysed for density without the need for cutting them into smaller pieces, as is the case for the Archimedes density measurement method. The method is non-destructive and does not require any special preparation of the test sample. Also, no liquid medium is in contact with the test samples, which is essential for samples with lower densities, which could lose their green strength when infiltrated with water. The only requirement for the test is that the test surface, from which density measurements are to be taken, needs to be as flat as possible and free from surface imperfections, however no polishing is required. Figure 6.13 shows the accuracy of measurements obtained for different material thicknesses. From the OEM manufacturers experience and the statistical observations shown in figure 6.13, it has been suggested that for accurate results when taking measurements from titanium or titanium alloys, the samples should be cut to 4 mm thickness.

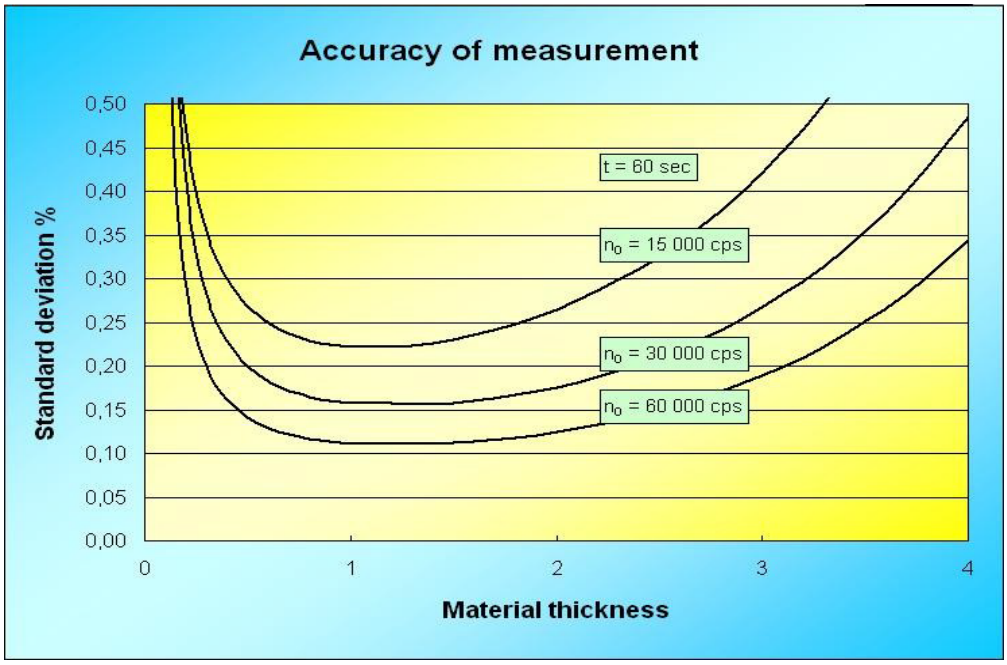

Figure 6.13: Accuracy of measurement based on material thickness [129]

Figure 6.14 shows marked-up test samples for density measurements. Material at the test point location was cut to 4 mm thickness and the measurement locations were identified. It should be pointed out that the marking process needs to be without indentation as it could increase the relative density at the test locations, thus an electro-

marking technique was adopted which leaves behind no damage or distortion in the metal.

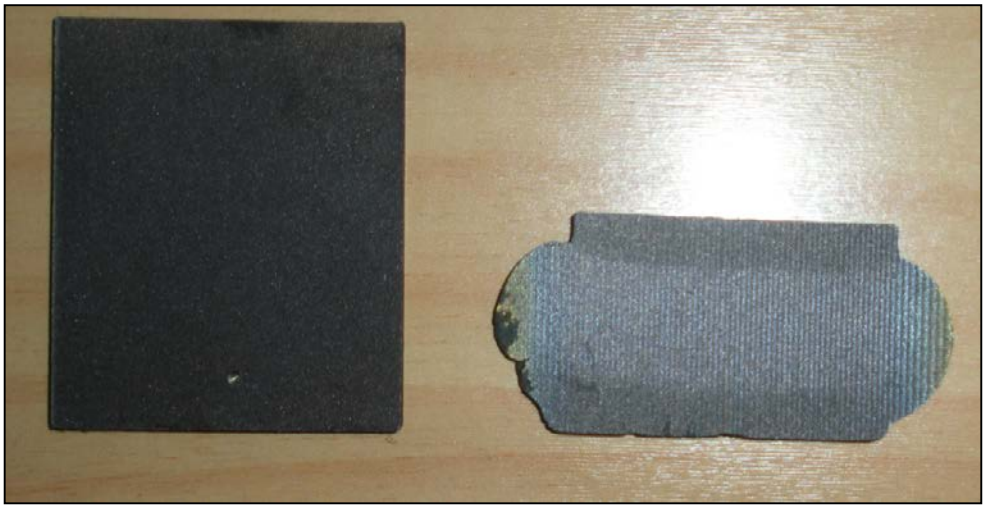

Figure 6.14: Cut samples marked for density measurements

6.6 Density measurements and FEA validation

The density measurements for HDH titanium forged parts are as shown in table 9.

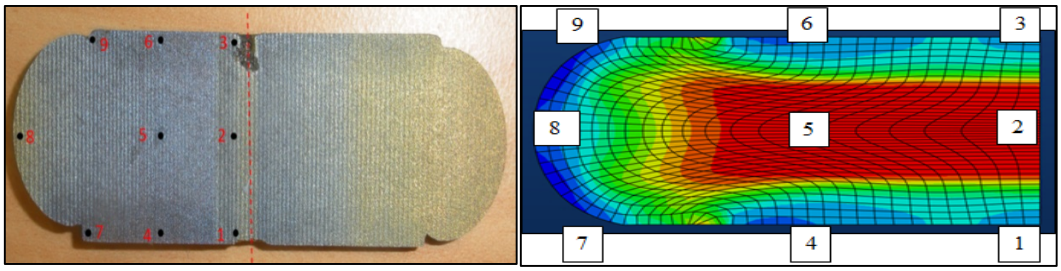

Sample No.	Test points	Simulated results		Gamma particle density measurements (c)	Relative error % (Gurson model) $(\lvert a-c\rvert)/c) \times 100$	Relative error % (G-T model) $(\lvert b-c\rvert)/c) \times 100$
		Gurson model (a)	Gurson Tvergaard model (b)			
CP1	1	0.88	0.92	0.94	6	2
	2	0.99	0.98	0.99	0	1
	3	0.88	0.89	0.94	6	5
	4	0.77	0.87	0.95	18	8
	5	0.99	0.99	0.98	-1	-1
	6	0.78	0.87	0.91	14	4
	7	0.95	0.94	0.96	1	2
	8	0.72	0.76	0.97	25	21
	9	0.95	0.94	0.93	-2	-1
Average RD		**0.87**	**0.90**	**0.95**		
CP2	1	0.82	0.91	0.88	6	-3
	2	0.93	0.96	0.98	5	2
	3	0.82	0.91	0.92	10	1
	4	0.89	0.94	0.87	-2	-8
	5	0.91	0.94	0.97	6	3
	6	0.89	0.92	0.88	-1	-4
	7	0.86	0.94	0.92	6	-2
	8	0.76	0.77	0.95	20	18
	9	0.88	0.94	0.98	10	4
Average RD		**0.86**	**0.91**	**0.93**		
CP3	1	0.81	0.94	0.91	10	-3
	2	0.94	0.95	0.98	4	3
	3	0.81	0.85	0.87	10	6
	4	0.86	0.91	0.85	-2	-7
	5	0.84	0.94	0.93	5	-5
	6	0.89	0.92	0.82	-8	-12
	7	0.81	0.98	0.92	8	-10
	8	0.74	0.75	0.94	18	17
	9	0.81	0.97	0.91	8	-8
Average RD		**0.83**	**0.91**	**0.89**		

Table 9: Simulated and measured densities for HDH titanium; a negative sign in the relative error indicates those locations where the simulated densities are higher than the predicted densities

Radio-graphical measurements indicated that the highest densities are observed at test points 2 and 5 and the lowest were at the circumference at test point 8. Though these results are consistent with the predicted densities by both models at the central region, the measured densities obtained at the circumferential region 8 were higher than the simulated results. The densities predicted by the Gurson-Tvergaard model were in closer agreement with the measured densities at regions 1, 2, 3, 4, 5, 6 and 7 compared with the original Gurson model. The prediction of densities at regions 7, 8 and 9 were lower with both models. This can be explained by the fact that the Gurson model is highly pressure dependent. Due to the high temperature at the centre of a forged part the peripheral region barrels outward in the early stages of deformation. Therefore there is not enough hydrostatic pressure transferring to this region to cause further densification.

Figure 6.15 shows the density measurements for an HDH Ti-6Al-4V forged part. It can be seen that the relative density obtained by measurements differs from the simulation results. The average relative density obtained by measurement is higher than the average predicted results for sample T61, which was forged at 1250 ^{o} C. However the average measured relative density is in closer agreement with the predicted results obtained from the Gurson-Tvergaard model. The Gurson-Tvergaard model showed good agreement with the measured results at regions 2 and 5, in all cases. In these regions the hydrostatic pressure is at its peak and this enhances the densification process. The measured densities in all cases were much higher at the peripheral region 8. This indicates that the Gurson-Tvergaard model underestimates the degree of densification in those regions where hydrostatic pressure is not fully transmitted.

Overall the density results from the Gurson-Tvergaard model agree well with the measured results. However, there are instances where the measured results are lower than the simulation results. There are three possible causes for this; (1) error in the density measurement technique at lower relative densities; (2) a density increase due to induction sintering which is neglected in the model; (3) a non-uniform density in the initial powder compact.

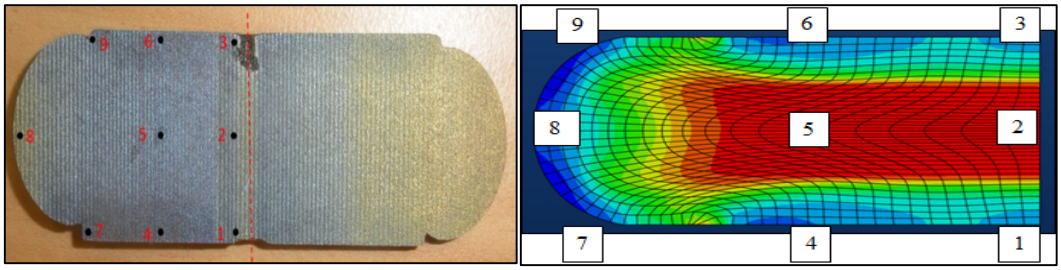

Sample No.	Test points	Simulated results		Gamma particle density measurements (c)	Relative error % (Gurson model) $(\lvert a-c\rvert)/c) \times 100$	Relative error % (G-T model) $(\lvert b-c\rvert)/c) \times 100$
		Gurson model (a)	Gurson Tvergaard model (b)			
	1	0.77	0.78	0.87	11	10
	2	0.99	0.99	0.99	0	0
	3	0.88	0.77	0.86	-2	10
	4	0.72	0.77	0.83	13	7
T61	5	0.99	0.99	0.99	0	0
	6	0.72	0.87	0.85	15	-2
	7	0.73	0.77	0.81	9	4
	8	0.71	0.78	0.89	20	12
	9	0.73	0.77	0.9	18	14
Average RD		**0.80**	**0.83**	**0.89**		
	1	0.74	0.82	0.83	10	1
	2	0.97	0.95	0.98	1	3
	3	0.74	0.82	0.95	22	13
	4	0.76	0.84	0.81	6	-3
T62	5	0.90	0.91	0.99	9	8
	6	0.76	0.84	0.81	6	-3
	7	0.91	0.93	0.80	-13	-16
	8	0.74	0.77	0.80	7	3
	9	0.90	0.89	0.84	-7	-5
Average RD		**0.82**	**0.86**	**0.87**		
	1	0.71	0.82	0.95	25	13
	2	0.91	0.92	0.98	7	6
	3	0.73	0.82	0.82	10	0
	4	0.70	0.87	0.85	17	-2
T63	5	0.87	0.89	0.98	11	9
	6	0.90	0.87	0.78	-15	-11
	7	0.91	0.96	0.83	-9	-15
	8	0.74	0.71	0.91	18	21
	9	0.91	0.93	0.84	-8	-10
Average RD		**0.82**	**0.87**	**0.88**		

Figure 6.15: Simulated and measured densities; negative sign in relative error indicate locations where simulated densities are higher than the predicted

6.7 Conclusion

In this chapter the experimental procedures used for powder compaction and forging were discussed. Powder compacts with a target relative density of 0.75 were produced and forged and the densities of forged parts were measured using a gamma particle radiography technique. The measured results were then compared with the predicted relative densities obtained using the Gurson and Gurson-Tvergaard models. From the results the following conclusions are drawn;

- It was confirmed that by using both coupled thermo-mechanical simulations and experimental measurements that the initial compact temperature has a significant influence on the final density.
- A significant difference in the relative density results given by the Gurson and Gurson-Tvergaard models was found. In general, the predictions given by the Gurson-Tvergaard model were higher than the results obtained from the Gurson model. This is due to the influence of the Gurson-Tvergaard material parameters q_1 and $q_2$on the plastic behaviour of the powder compact. The parameters q_1 and q_2 have a significant effect on the collapse or closure of the voids. In addition, the parameter q_3 had no significant influence.
- The relative density obtained for HDH Ti-6Al-4V was significantly lower than that for HDH titanium forged under the same conditions.
- For HDH titanium and Ti-6Al-4V, increasing the initial forging temperature had a significant effect on the final consolidation density; this has been proven by experiments and numerical results.
- Closed die forging HDH Ti-6Al-4V, with the present initial relative density of 0.75 is not recommended due to cracking at lower temperatures; however the results can be improved with a better compaction technique (warm compaction, high velocity compaction or CIPing) to achieve higher relative density. In contrast, HDH titanium powder compacts can be forged with the present initial relative density obtained by cold die compaction.
- The relative density prediction from the Gurson-Tvergaard model was closer to the radio-graphically measured results at locations towards the centre of a forging; however the predicted results underestimated the density at the

peripheral region. This is due to the dependence of the Gurson-Tvergaard model on the local hydrostatic pressure. The hydrostatic pressure at the peripheral region is lower due to the deformation and die chilling effect.

7 Case study A: Powder forging of a cylindrical component by hot-repressing and extrusion

Hot re-pressing is a potential method for the production of cylindrical titanium fastener grade components. The hot re-pressing technique involves heating a powder compact to the forging temperature and applying compressive forces in a rigid die to consolidate the powder compact into a fully dense part. Unlike hot upsetting, in hot re-pressing the pressure increases the driving force for densification, however the lateral movement of the material is often constrained. A hot re-pressing technique has never been applied to the fabrication of titanium components, thus this study attempts to investigate the deformation and densification mechanism using the original Gurson and Gurson-Tvergaard models.

Due to the large deformation involved in the geometries implicit modelling technique available in Abaqus standard proved to be inadequate for the densification case studies. Abaqus explicit modelling was chosen as more favourable re-meshing options were available. The difference between the implicit and explicit modelling method are described in section 3.1.7. An initial simulation study was performed using implicit and explicit method to compare densification results. The results showed no significant variation in density profiles using both methods.

7.1 Experimental details

Figure 7.1 shows the dimensions of the target component. From the results of work on compaction given earlier in this thesis, a lower density occurs at the bottom of a compact compared with the top. To achieve a more uniform density distribution a hot-repressing and extrusion approach was used. The dimensions of the target component are shown in Figure 7.1 and the die design is shown in figure 7.2 (a). This die design provides for a simultaneous partial extrusion and hot pressing. The extrusion ratio used was 2.44:1 and in order to streamline the flow through the die a 2 mm radius was specified for the extrusion end of the die.

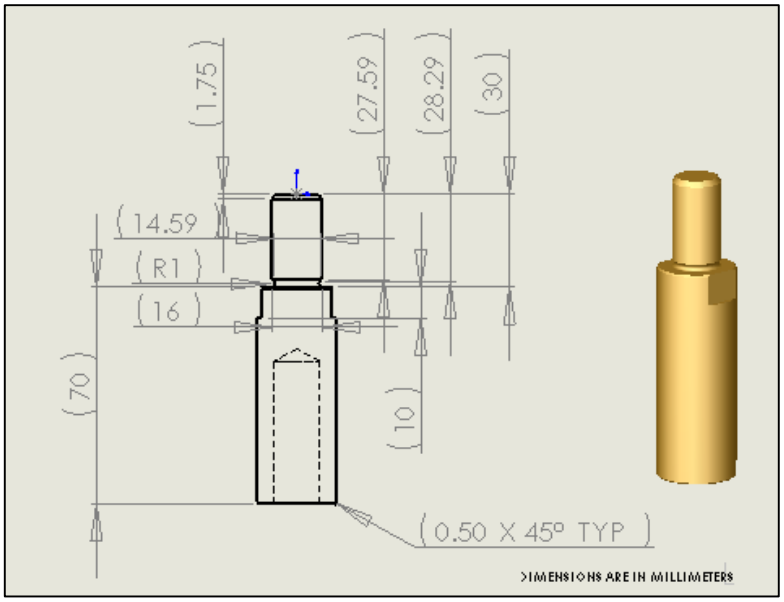

Figure 7.1: Dimensions of the target cylindrical titanium component

The material used in this experiment was HDH titanium alloy powder with mesh size 200 µm. Cylindrical powder preforms Ø 24.6 mm were cold compacted and the height was decided based on the final relative density required. For an initial relative density of 0.75 a height of 95 mm was chosen for the powder compact. The compacts were induction heated to 1250^{o} C and held for 5 minutes before being transferred to the forging die. The dies were preheated to 100^{o} C. A 100 ton load was applied by the punch to forge the material into the die and the final part was ejected out of the die as shown in figure 7.2 (b).

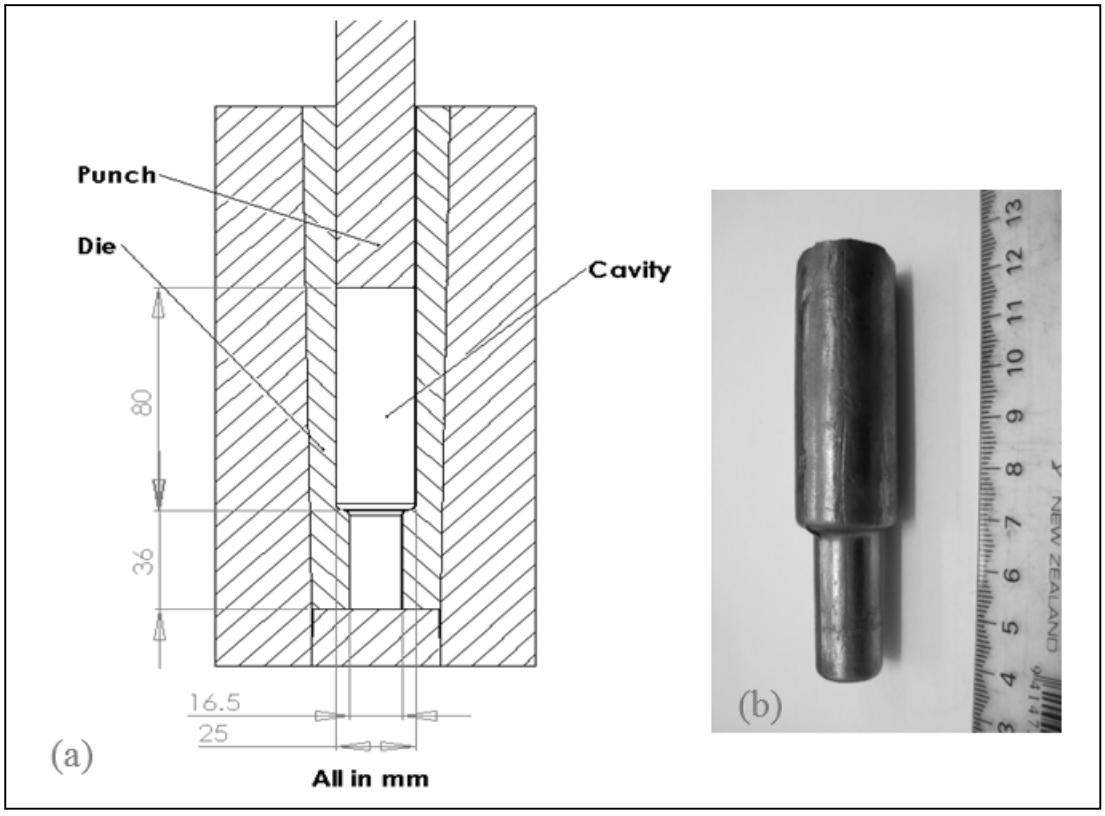

Figure 7.2: (a) Forging die assembly; (b) final part after hot-repressing

7.1.1 FEA modelling

The geometry of the part and the mesh used for FEA modelling of both the compact and the die are shown in figure 7.3. The finite elements used for the simulations are 4-node plane strain thermally coupled quadrilaterals with reduced integration and hourglass control. The punch and the die are modelled as elastically deformable materials. The contact conditions are defined according to the approach suggested in section 3.1.4 based on a master-slave surface relationship. A constant coulomb frictional condition of 0.1 was specified for all the surfaces in contact. An interfacial heat transfer coefficient model which was previously estimated in section 4.3, was used. An ALE mesh was assigned to the powder compact region to avoid convergence problems due to excessive distortion during the process. Mesh penetration was observed during the early stages of the simulation trials, thus a finer mesh was defined only at the radius of the die. The temperature of the powder compact and the die were set to 1250^{o} C and 100^{o} C respectively and the top punch was held at room temperature. A displacement boundary condition of 40 mm was applied to the top punch to simulate

the process. The simulations were carried out for HDH titanium powder using the original and the Gurson-Tvergaard models.

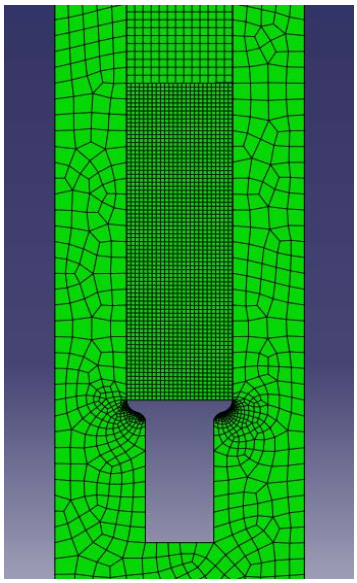

Figure 7.3: FEM model of compact die assembly

7.1.2 Simulation results

The relative density distribution plots and deformation obtained at an initial compact temperature of 1250^{o} C is shown in figure 7.4. It can be seen that the densification begins in the region that passes through the die radii. This is expected as the material in this region undergoes plastic strain first. Initially there was a slower densification in the rest of the component. The front end of the billet showed almost no densification as it exits the die. This anomaly is because there was no boundary condition applied to the powder compact at the front end during the early stage. However, after the extrusion region is completely filled the rest of the part undergoes subsequent densification.

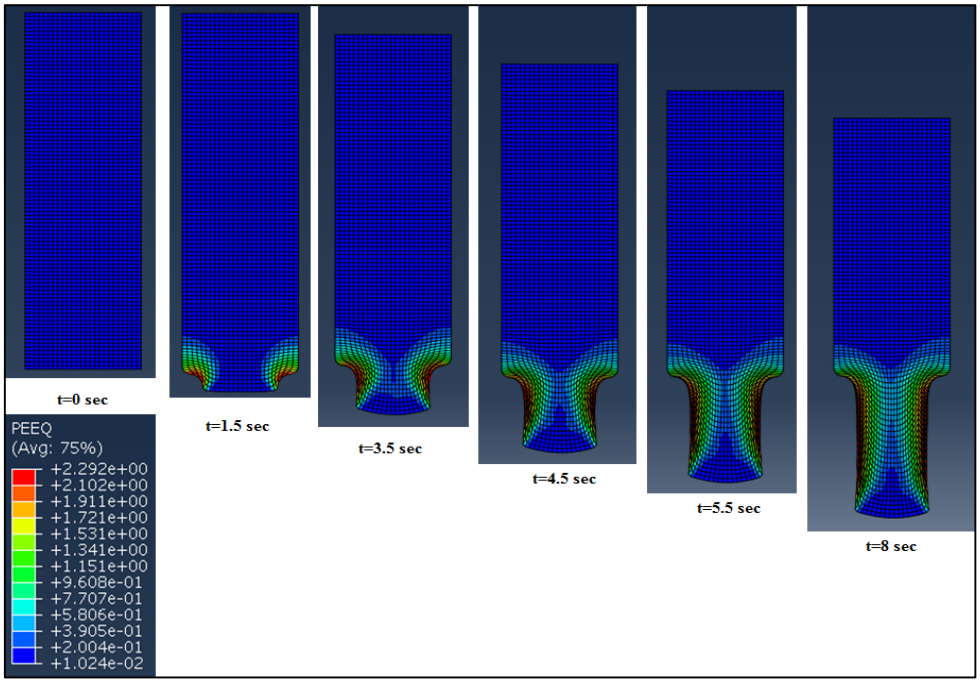

Figure 7.4: Equivalent plastic strain and final consolidated stage; t=0 is the initial state of the powder compact; t=8 sec is the consolidated state

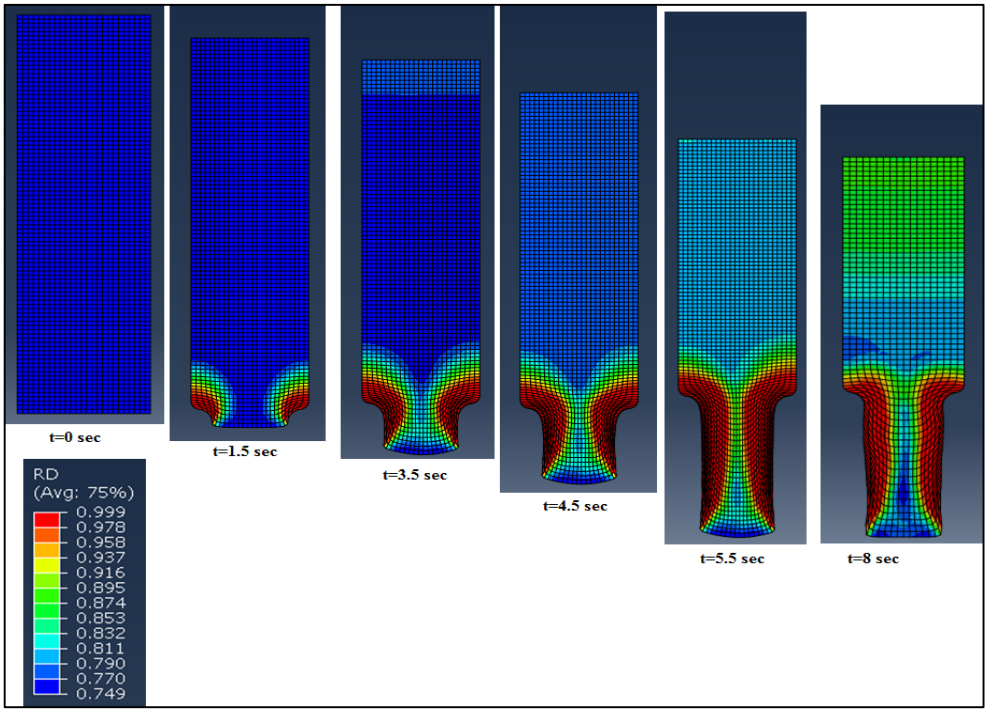

Figure 7.5: Relative density and final consolidated stage, at t=0 is the initial state of the powder compact; t=8 sec is the consolidated state

It can be seen that the densification profile and the deformation geometry predicted by the Gurson model and the Gurson-Tvergaard model show a significant difference in pattern, also the values predicted by the Gurson-Tvergaard model are higher than those predicted by the original Gurson model. It must be noted that, in contrast to the rest

of the part geometry, the densification occurring at the die radius is due to shear straining, whereas in the rest of the geometry the mechanism of densification is by hydrostatic pressure.

To investigate this further, plastic strain, hydrostatic pressure and relative density versus simulated processing time at selected nodes are shown in figure 7.6 to figure 7.8. It can be seen that during the initial stages of extrusion the plastic strain at nodes 1 and 2 is low; however it gradually increases after the die filling is complete. In contrast, the hydrostatic pressure at nodes 1 and 2 reaches maximum values of 193 MPa and 165 MPa respectively when die filling is complete. After the extrusion part of the process, the hydrostatic pressure further increases until the process is completed. Compared to nodes 1 and 2, the plastic strain at node 3 increases at the point where the extrusion begins, the plastic strain further increases after the front end hits the bottom die.

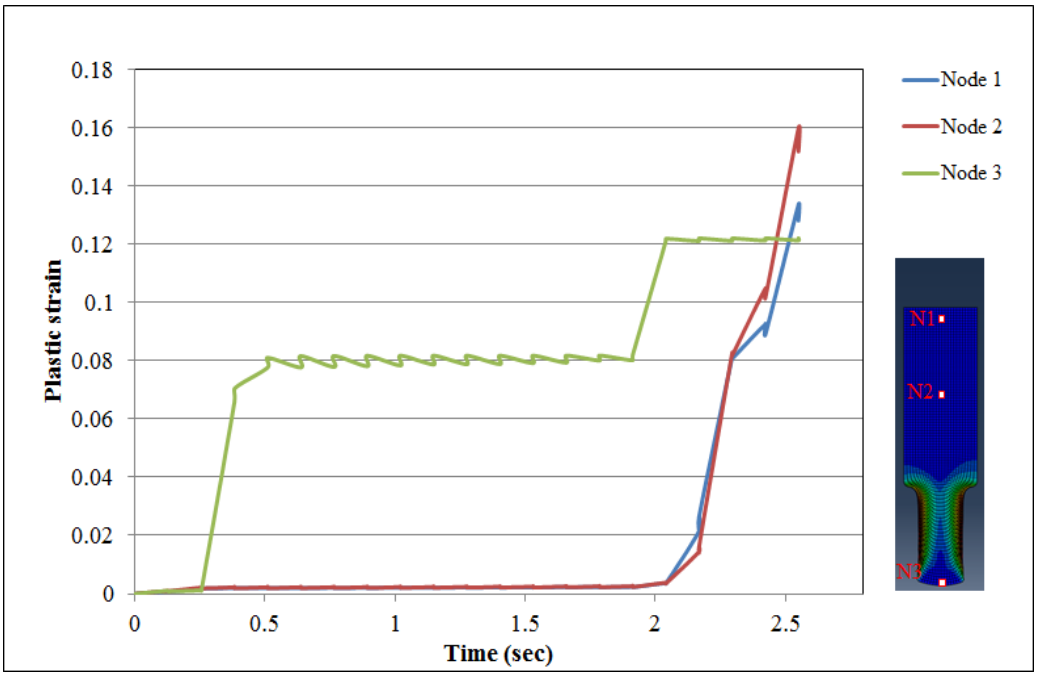

Figure 7.6: Plastic strain vs. time period at selected nodes

The hydrostatic pressure experienced by Node 3 fluctuates during the extrusion stage; however it decreases after the die filling is complete. The relative density versus time plot reflects the plastic strain and hydrostatic pressure data. No consolidation of the powder is seen at nodes 1 and 2 until the extrusion is complete. At these regions, the relative density increases gradually until the end of the process. Also note that low

densification is seen at node 3, which corresponds to the low hydrostatic pressure in this region. It is also worthwhile pointing out that the hydrostatic pressure, strain and relative density data presented here corresponds to the selected die radius and these data may vary depending on the die radius. For example, a higher die radius may increase the hydrostatic pressure and the corresponding density at the early stages of the process. The purpose of these results is only to highlight the dependence of hydrostatic pressure on densification in the Gurson model.

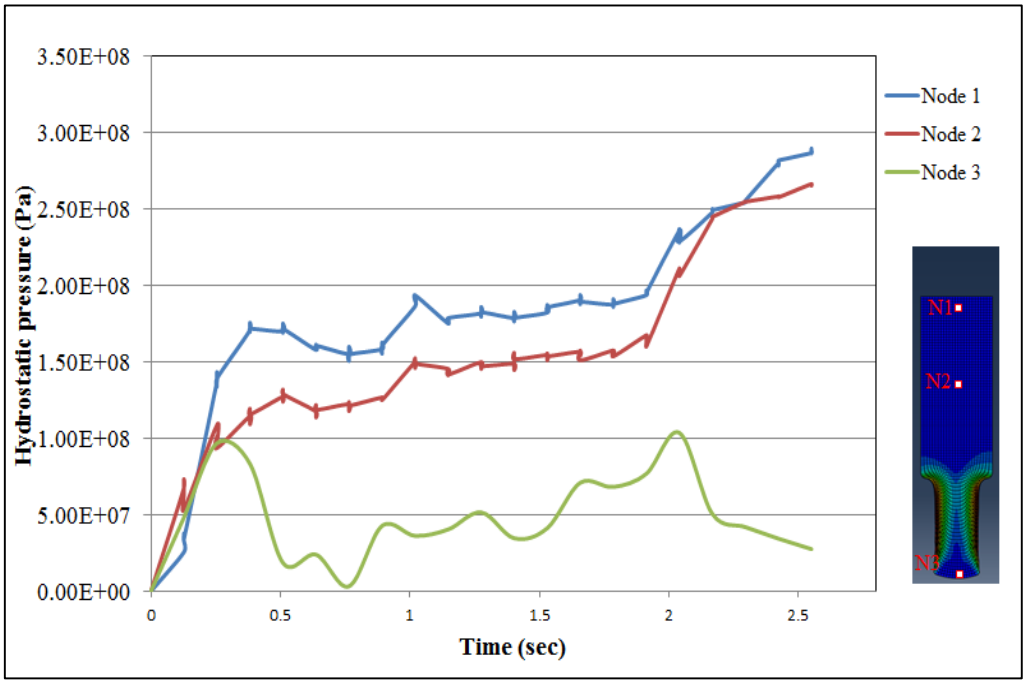

Figure 7.7: Hydrostatic pressure vs. time period at selected nodes

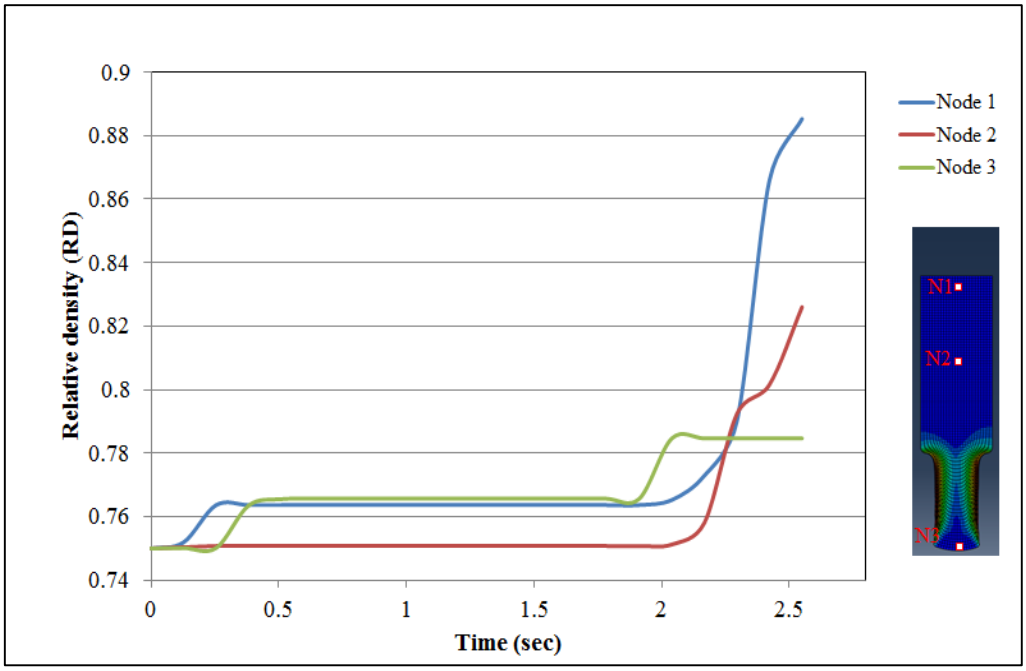

Figure 7.8: Relative density vs. time period at selected nodes

Figure 7.9 shows the final relative density profile and the shape obtained after simulation using the Gurson and Gurson-Tvergaard models. The density profile for hydrostatic consolidation predicted by both models is similar, however the final length of the leg and the densification histories differ. Figure 7.10 and 7.11 show the densification data versus time using the original Gurson and Gurson-Tvergaard models. By comparing these, an enhanced densification rate is predicted by the Gurson-Tvergaard model. Both models predict high densification in the extruded region.

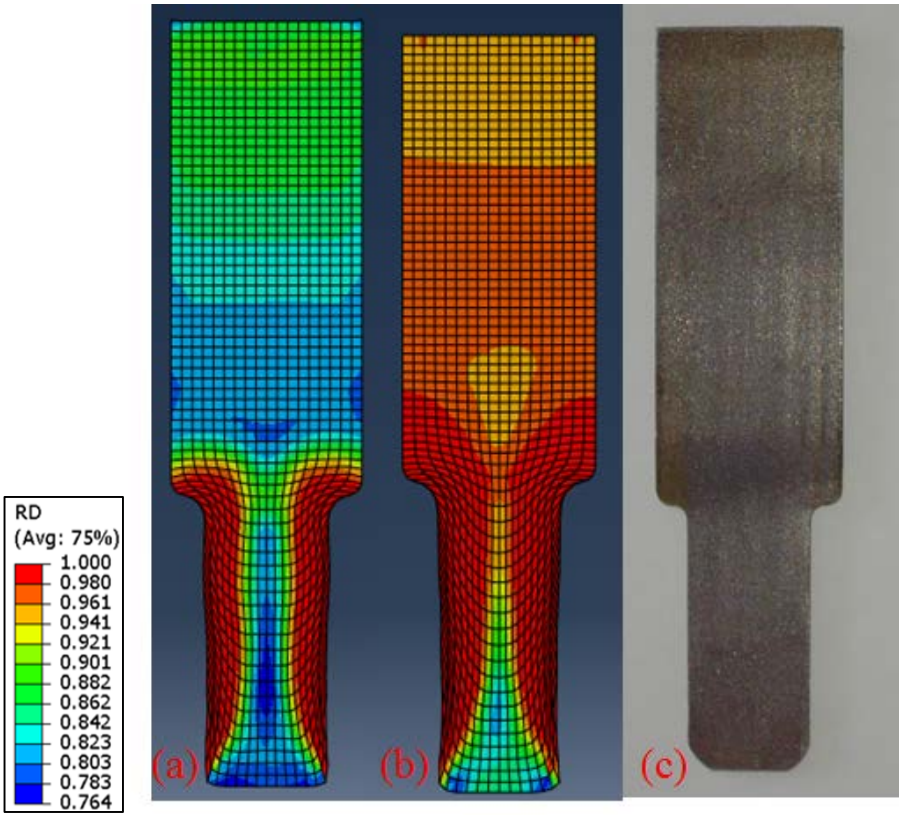

Figure 7.9: Relative density and final shape (a) Gurson model; (b) Gurson-Tvergaard model and (c) experimental

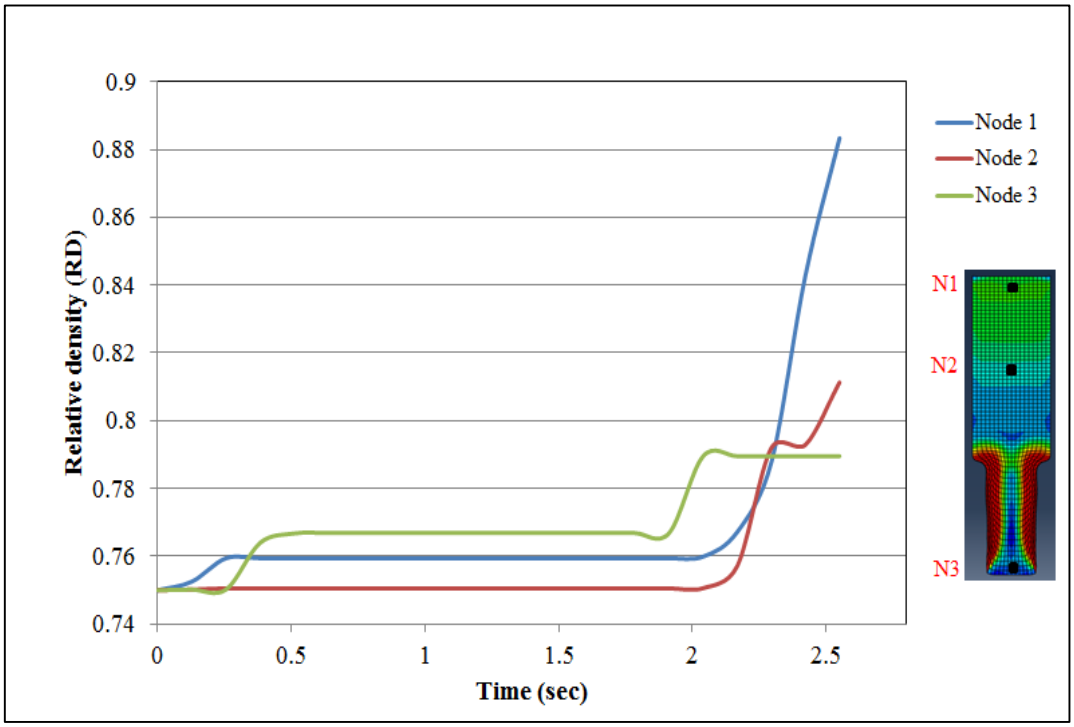

Figure 7.10: Relative density data versus time period at selected nodes using Gurson model

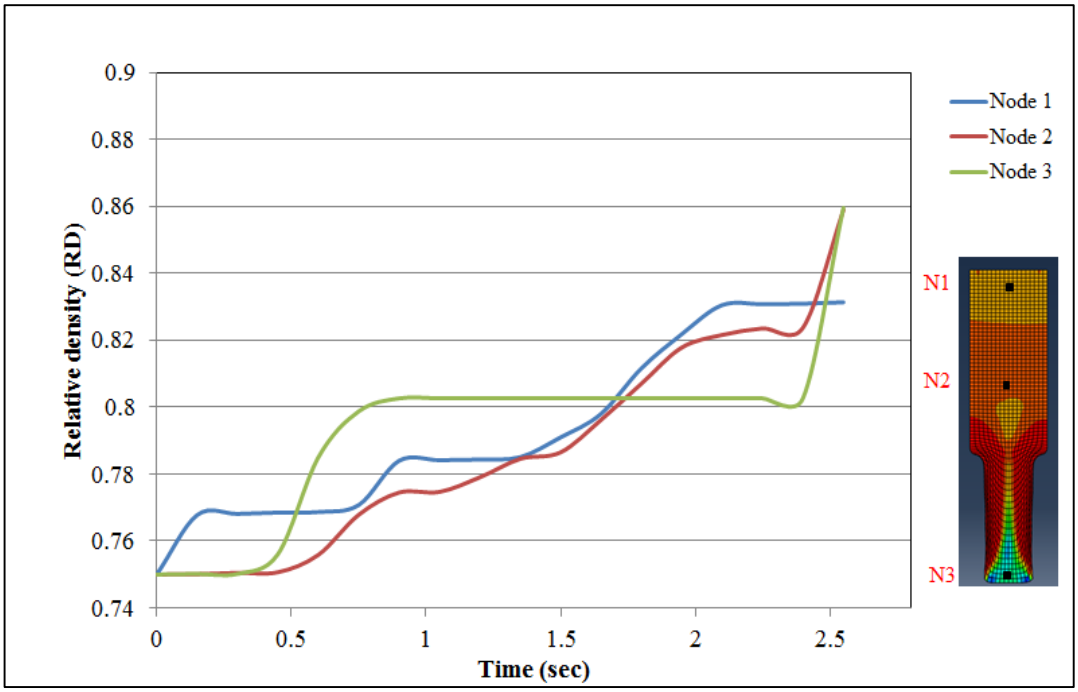

Figure 7.11: Relative density versus time period data at selected nodes using Gurson-Tvergaard model

7.1.3 Density measurements

The density of an HDH titanium cylindrical component was measured using a gamma-particle radiography technique. A sample was cut to a uniform thickness of 4 mm for the density measurements. Figure 7.12 shows the simulated and experimentally measured densities for a cylindrically shaped HDH titanium component.

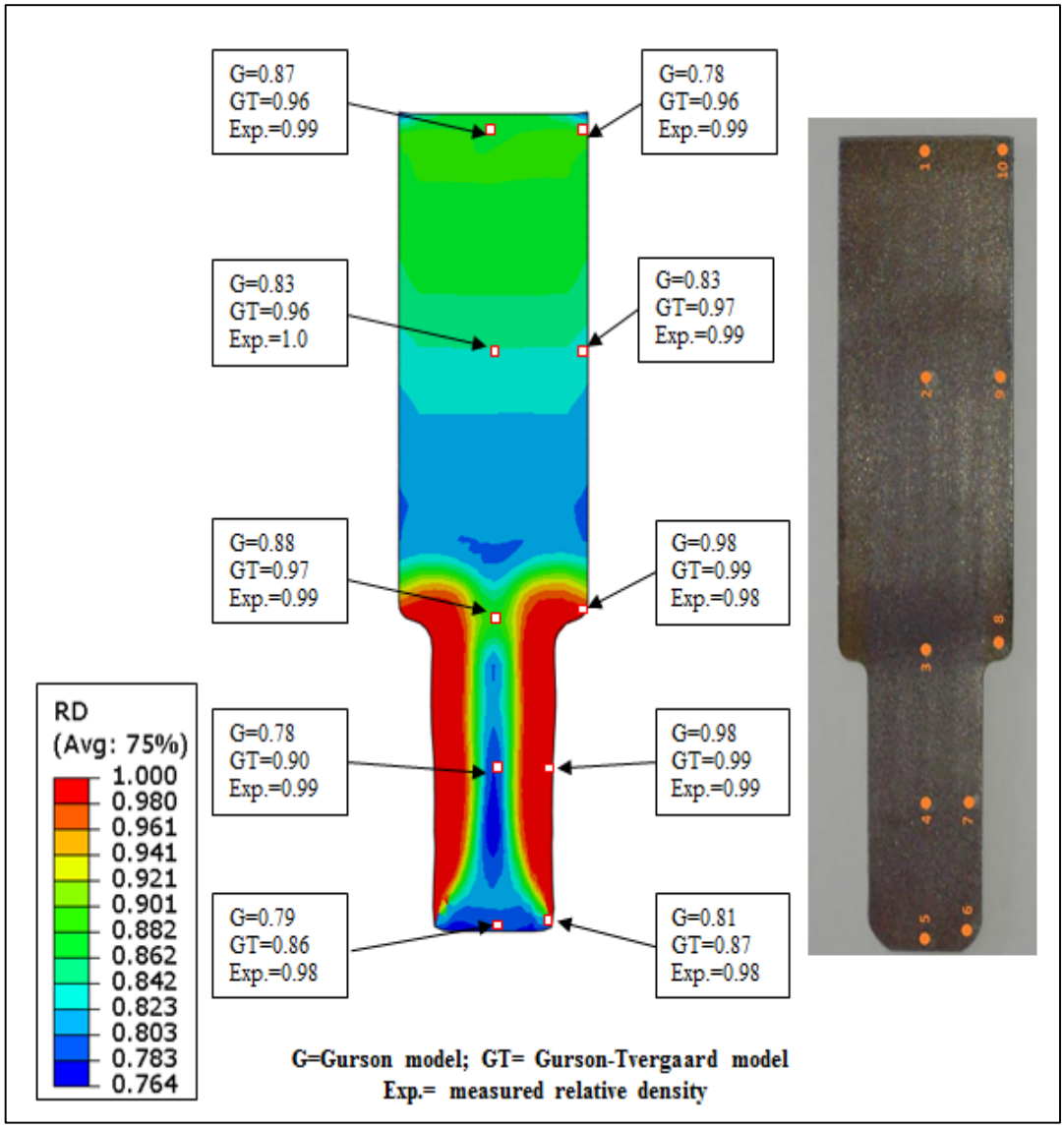

Figure 7.12: Comparison of relative density results calculated using Gurson, Gurson-Tvergaard and measured values

When comparing the results from both models, it can be seen that the overall density predictions using the Gurson-Tvergaard model are in better agreement with the measured relative density results. However, the measured relative densities at regions 4 and 5 were higher than the predicted values.

7.1.4 Conclusion

In the present study, a hot-pressing technique to produce a titanium cylindrical component was investigated though finite element simulations. A billet with an initial relative density of 0.75 percent was hot pressed and extruded through a streamlined

die. During extrusion and hot-pressing, the stresses, plastic strains, hydrostatic pressure and relative density patterns are seen within the powder compact.

A computational model was implemented in Abaqus/Explicit using the original Gurson and Gurson-Tvergaard models. Numerical simulation results for the density distribution have been compared against experimental data to validate the computational model. The prediction by the Gurson-Tvergaard model shows higher densification compared with the original Gurson model. The results showed that the densification in hot-repressing is governed to a larger extent by the hydrostatic pressure. The numerical results from the Gurson-Tvergaard model are in closer agreement with the experimental results.

One of the major problems encountered during the simulations was that of re-meshing in the areas of the powder compact that was undergoing extrusion. At times, the simulation during extrusion of the front end of the billet often stopped, due to excessive distortion. An adaptive re-meshing technique, available in Abaqus/explicit, was used to correct this. It is also interesting to note that measured relative densities at the selected locations were higher than those predicted by both the Gurson and Gurson-Tvergaard models.

7.2 Case study B: Powder forging of ring shaped component

In this study, the three-dimensional stress, strain and densification of a ring-shaped component, produced by simulated powder compact forging, was analysed using a finite element method. For a complete densification analysis of a given geometry a consideration of die shape in the cross-sectional area of deformation is necessary in the 3D process modelling. Additionally in order to investigate the accuracy of the model the simulation results were compared with density measurements obtained experimentally.

7.3 Experimental details

Figure 7.13 shows solid models and a schematic of the ring shaped component. The material used for the product is HDH titanium powder.

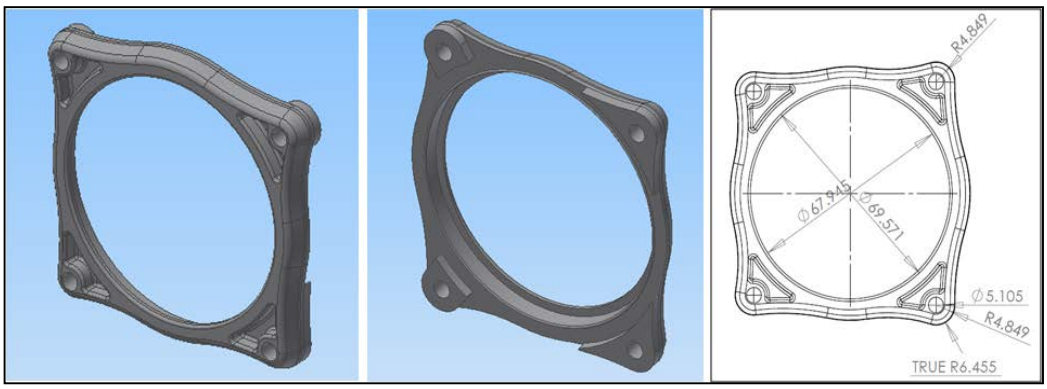

Figure 7.13: (a) 3D models of the components showing features (b) schematic diagram

For producing the powder compact 150 grams of HDH titanium powder was poured into the compaction die which is shown in figure 7.14. The powder compaction die consisted of a top punch and an inner core for producing the powder compact geometry as shown in figure 7.14. A graphite based die lubricant was used for the inner die walls to allow easy release of the powder compact after compaction. The compaction was carried out at room temperature and at a predetermined pressure to produce a final powder compact with 75 percent densification. The final thickness, compaction pressure and compact density are important factors in deciding the forging stroke required to fill the die cavity. These factors are mutually dependent thus they are difficult to estimate without a trial and error approach. An accurate depiction of

density vs. compaction pressure curves for the material could solve this problem; however during this experimental work such information was not available.

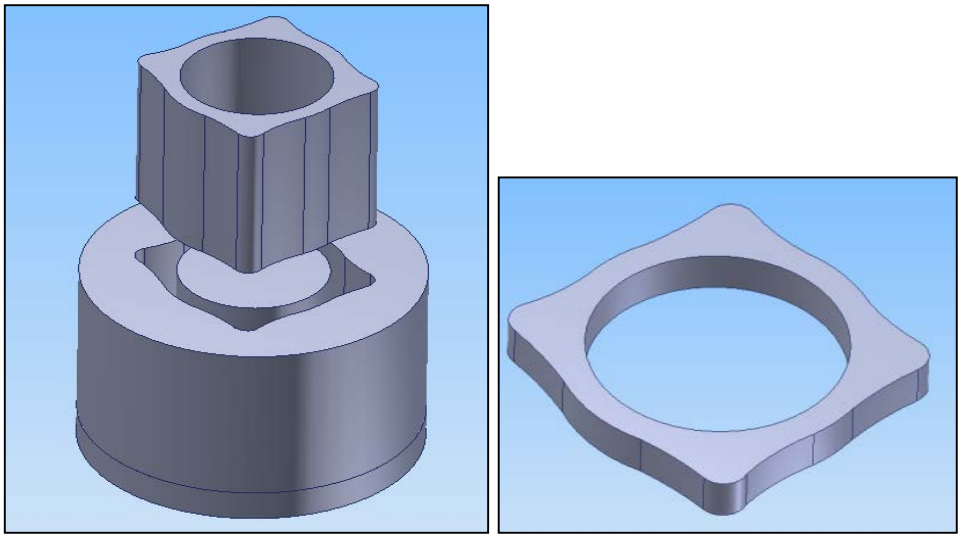

Figure 7.14: Powder compaction die and powder compact shape

Figure 7.15 shows a model of the closed forging dies used in this study. The dies were pre-heated to a temperature of 200 ^{o}C using band heaters. A liquid graphite lubricant was applied to reduce friction. The powder compacts were induction sintered and forged at a temperature of 1250 ^{o}C. Figure 7.16 shows the final shape obtained after powder forging.

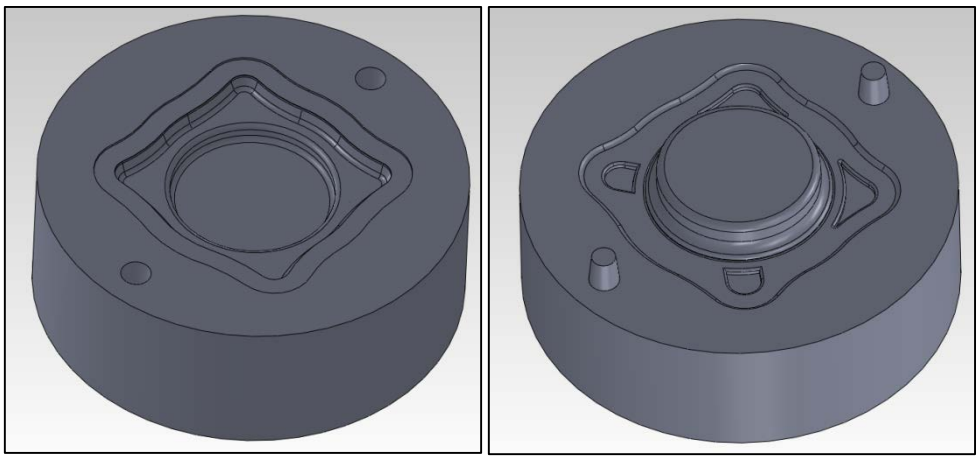

Figure 7.15: Bottom and top die

Figure 7.16: Final geometry after powder forging

7.4 FEA modelling

Abaqus/Explicit finite element simulation code was used to model the process. Abaqus/Explicit is a robust program when dealing with more complex die geometries, metal-tool interactions and it has the required meshing capabilities for use in powder metal forming simulation. In contrast Abaqus/standard has to iterate to solve non-linear problems. Also, Abaqus/Explicit is more efficient in terms of computational time and space requirements for solving large deformation problems.

Models of the die and the powder compacts were imported into Abaqus from CAD software and meshed with their respective elements. In this work the forging dies were meshed with 4-node thermally coupled tetrahedron, linear displacement and temperature elements, whereas the compact was meshed with an 8-node thermally coupled brick elements, with tri-linear displacement and temperature, reduced integration, hourglass control. An ALE adaptive mesh domain was defined for the powder compact with a frequency of 5 sweeps per time increment.

The material for the die was modelled as AISI-H13 steel and the powder compact was modelled as HDH Titanium powder with 75 percent relative density. The compact was radially constrained and a constant velocity of 7 mm/sec was specified for the top die. The surface interaction between the powder compact and the dies was modelled using kinetic contact formulation with finite sliding. A constant coefficient of friction of 0.1 was assumed.

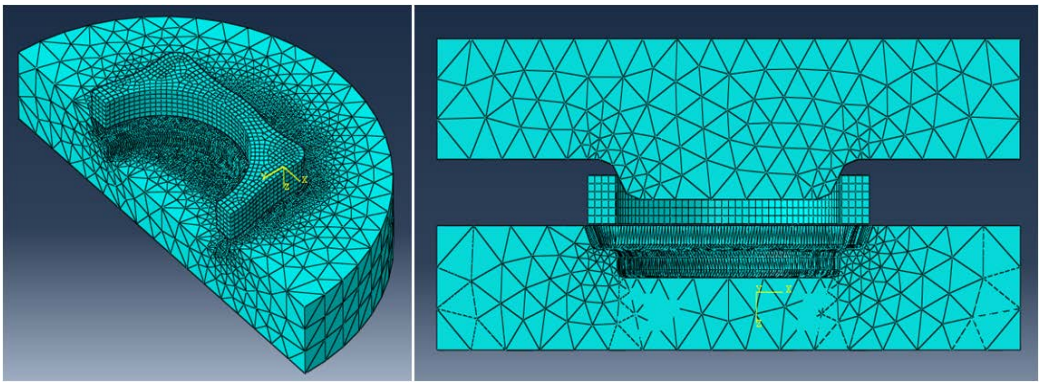

Figure 7.17: Model setup with a finite element mesh

The simulation step was defined as dynamic, temperature-displacement-Explicit. No mass scaling option was used for the simulations as this study involved a material whose density was changing with time. The initial powder compact and the dies were assigned an initial temperature of 1250 ^{o}C and 200 ^{o}C respectively. Interfacial heat transfer coefficients were defined to allow heat flow from the powder compact to the dies during forging.

7.5 Simulation results

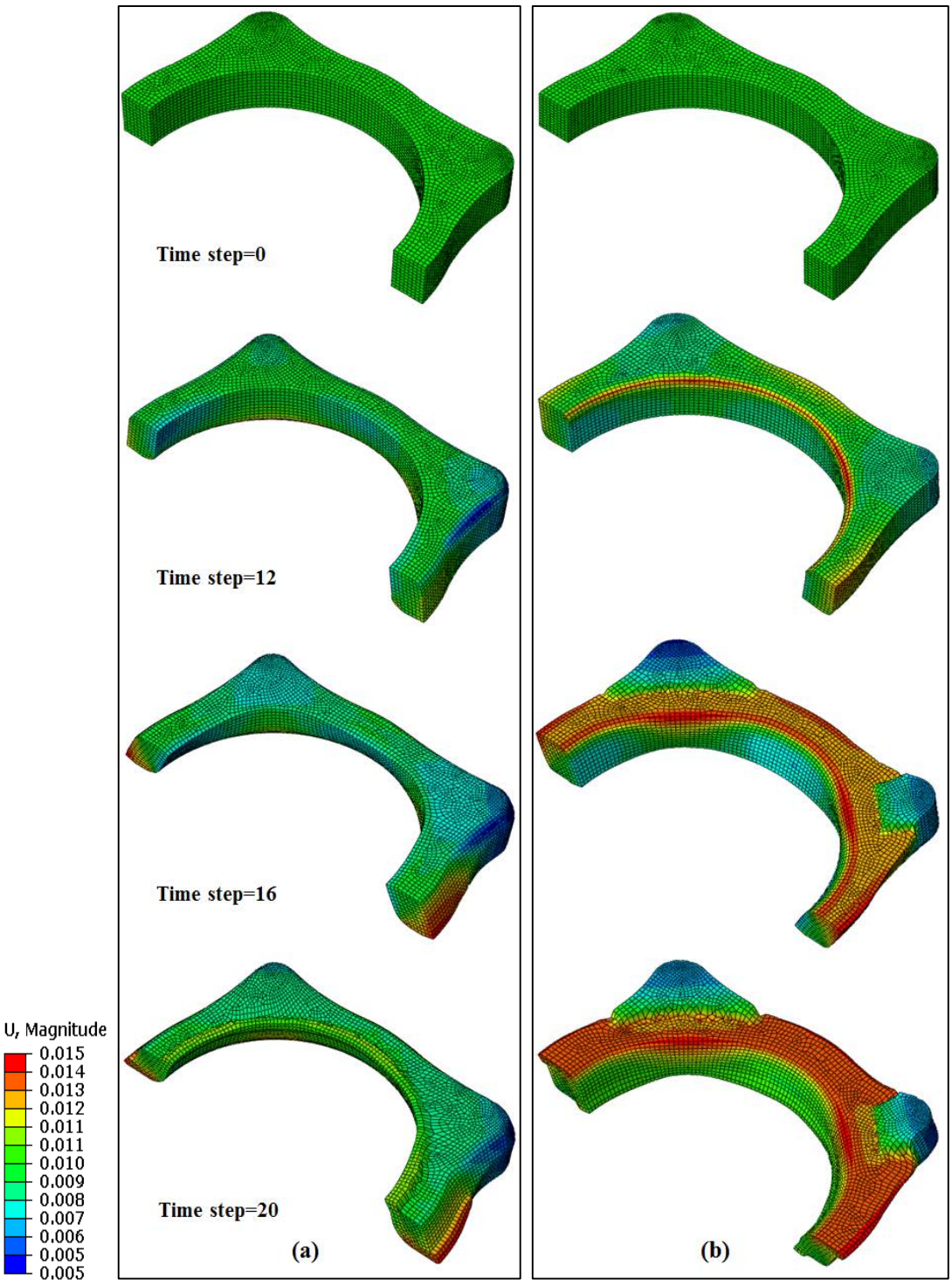

Figure 7.18: Deformation magnitude and sequence at different time steps; (a) Top side, (b) bottom side

Figure 7.18 shows the deformation sequence of the powder compact during closed die forging. A coupled thermo-mechanical simulation was carried out using the Gurson model for a simulation time period of 10 seconds. From the deformation sequence it

can be seen that the material flowed away from the centre during forging. Also notice that in figure 7.19, the regions E and F were formed by back filling.

Figure 7.19 shows the temperature distribution and relative density obtained after forging using the original Gurson model. It can be seen that there is significant heat loss to the die during powder forging. The temperature of the forged part decreased with time; however the temperature at the region E and F remained the same. It must be pointed out that the top surface of the back filled regions E and F are not in contact with the top die until the end of the simulation time step. Regions A and B remained at a higher temperature compared to the rest of the component. This is due to the fact that as regions E and F were being filled, regions A and B lost contact with the bottom die. Also higher temperatures were seen at the middle of the component, but the temperature decreased with time.

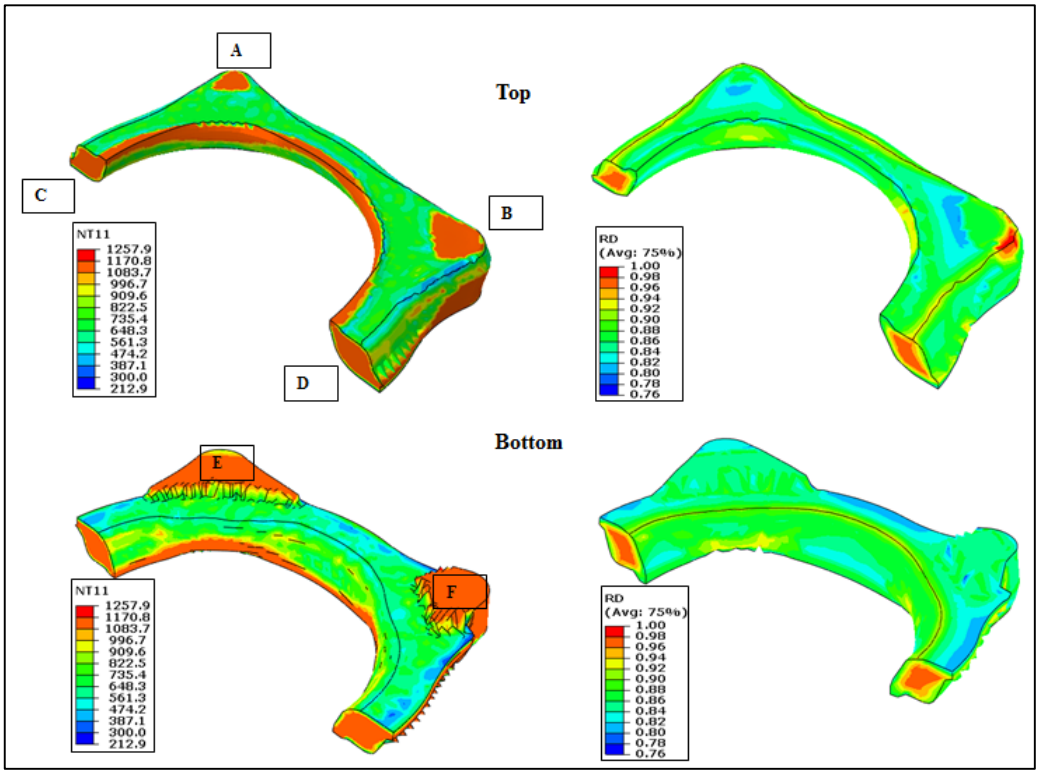

Figure 7.19: Temperature and relative density distribution using the Gurson model

The 96-98% relative density at the centre was higher than that at the outside surface regions, where the maximum density was about 90%. The lowest relative density was seen at A, B and near the flash regions. Simulation was carried out using both the

Gurson and the Gurson-Tvergaard model using the estimated parameters for an HDH titanium powder compact.

The relative density distributions given by both models are shown in figure 7.20. From the simulated data it can be seen that both models predicted full densification near the inner part of the component. The Gurson model predicted the lowest relative density near the flash region and the highest densification at the edge near to region B. According to the Gurson model, the density distribution in the part ranges from 0.76 to 1.0 (full density). The Gurson model also showed a low relative density at the regions A and B. Low densification at this region is due to the backward flow of material occurring due to back filling. In contrast to this, the Gurson-Tvergaard model showed a higher densification throughout the component for the same conditions. The density distribution ranges from 0.82 to 1.0 in the component except at the region E and F where low densifications were seen. In contrast to the Gurson model, the inner corners of the component showed higher densification with the Gurson-Tvergaard model. In both models, it can be seen that the bottom regions (E and F) and top regions (A and B) do not fully consolidate.

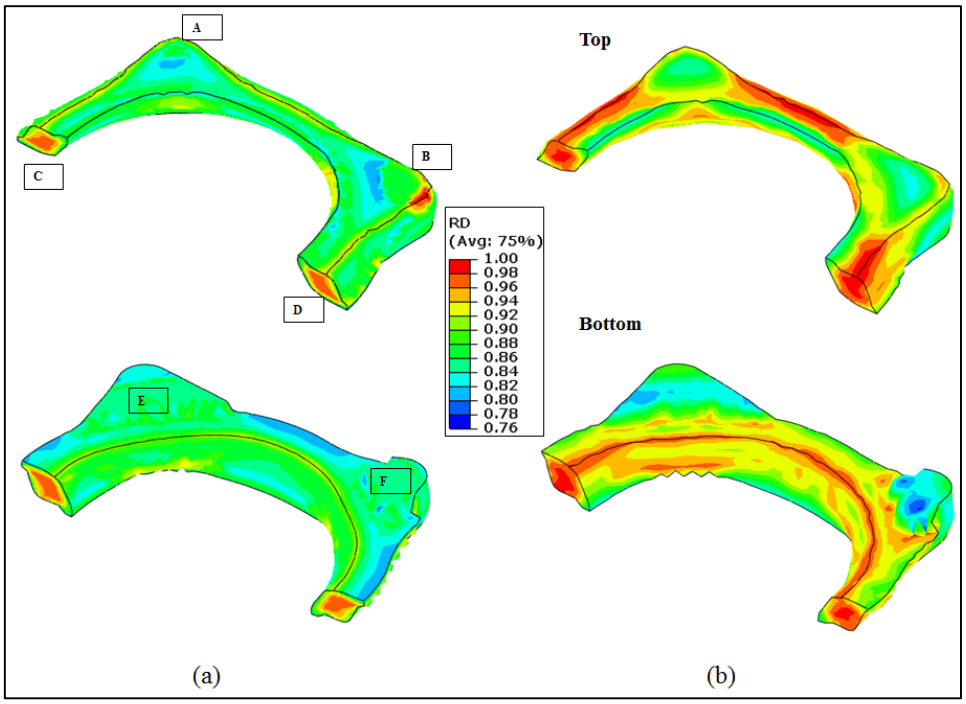

Figure 7.20: Relative density distribution (a) Gurson model; (b) Gurson-Tvergaard model

7.5.1 Density measurements

For density analysis the ring shaped titanium component was cut to a thickness of 4 mm at the locations shown in Figure 7.21. The relative densities at the selected points were measured radio graphically and the values were plotted with the simulated values obtained from the Gurson and Gurson-Tvergaard models. The measured relative densities were highest at the centre which was consistent with the simulated results. The measured values were in closer agreement with the Gurson-Tvergaard model at locations where the simulated densities were above 0.9. At lower relative densities, below 0.9, the Gurson-Tvergaard underestimated the degree of densification. From the radiography results it was clear that full density (RD=1.0) was achieved at several regions in the component. However, the density gradient seen in the forged part was largest where the density decreases from the centre to the edge of the component at sections A-A and D-D. At sections B-B and C-C, the relative density was seen to be low due to die back filling at regions E and F.

It should be noted that the densification results presented here are based on the assumption that in the simulations the initial powder compact density was uniform and that no densification took place during induction sintering. In reality, the powder compacts produced through uniaxial pressing are known to have a non-homogeneous density and the density increases during induction sintering. Nevertheless, the density gradient predicted by the simulation allows for the detection of possible low density regions so that corrective actions can be taken in the early stages of die design.

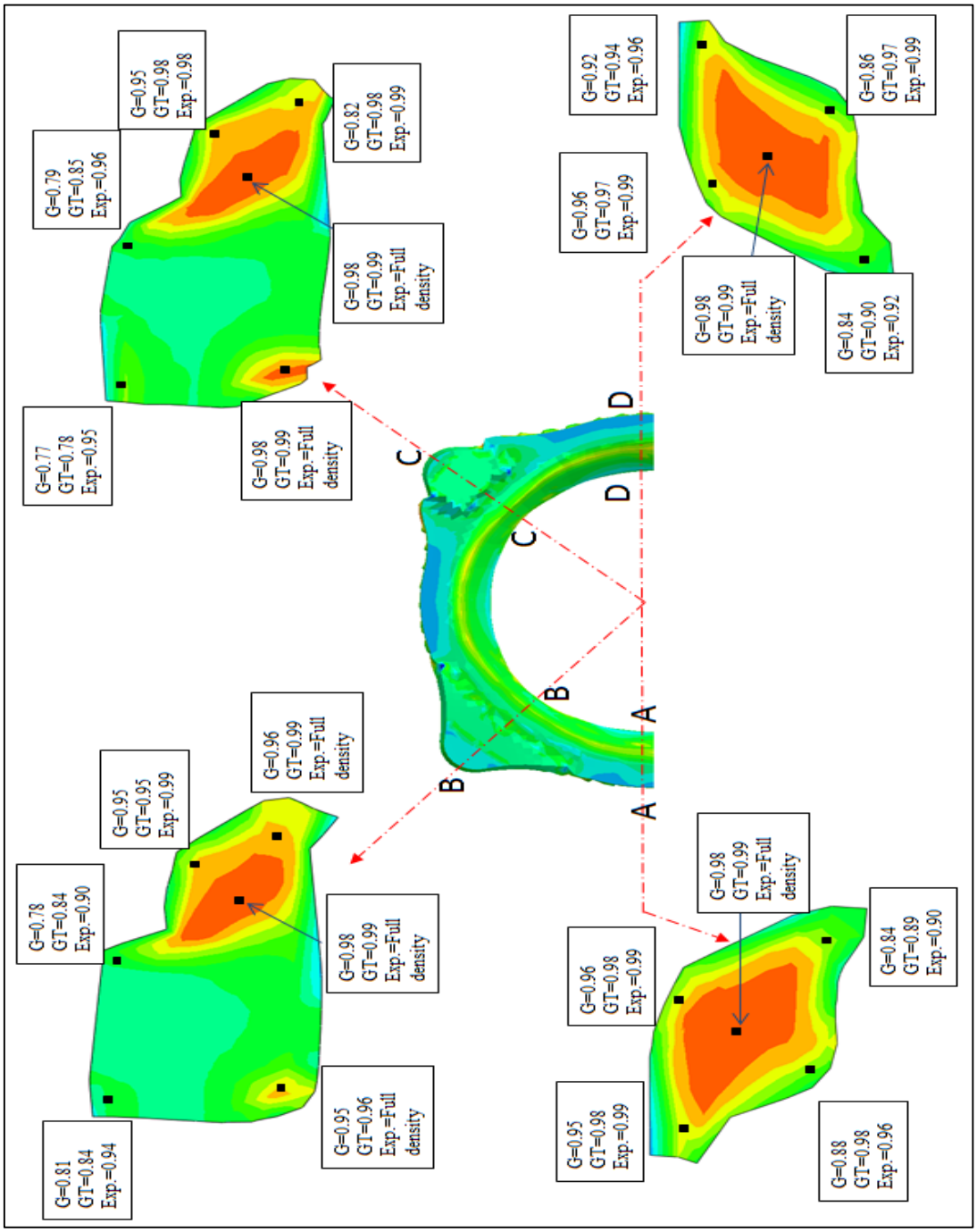

Figure 7.21: A comparison of the relative density results calculated using the Gurson, Gurson-Tvergaard and measured values

8 Discussion and conclusions

A Finite element simulation of powder compact forging for a circular disc, and a hot-pressed extruded cylindrical shape were performed. A material model was identified that could simulate the densification process during powder compact forging at low initial densities. Model correction parameters proposed by Tvergaard were determined and analysed. The densification predictions obtained from the original Gurson model and the Gurson-Tvergaard model were compared with the experimental results. The relative density of the produced titanium components were tested using a radiography technique.

8.1 Comment on processing

8.1.1 Disc forging

Powder compact forging of HDH titanium and HDH Ti-6Al-4V with an initial relative density of 0.75 was carried out. The density of a powder compact increased during forging and the final relative density increased with increases in the initial forging temperature. High density HDH titanium powder compacts could be produced by a single action cold powder compaction, whereas HDH Ti-6Al-4V powder compacts required the maximum capacity of the 100 ton press to achieve the required density for the experiments. During the experimental work surface cracks were visible on HDH Ti-6Al-4V powder compacts forged at a temperature of 1250 ^{o}C. The cracks further widened when forged at a lower initial temperature of 1000 ^{o}C. In practice, as the powder forging operation progresses a powder compact will lose heat to the die and cracks might occur at regions where the temperature is below 1000 ^{o}C; thus powder forging HDH Ti-6Al-4V powders at the investigated relative density is not recommended. On the other hand, no cracks were seen in HDH titanium powder compacts even when forged at a lower temperature. The measured densities of HDH titanium were much higher than those for HDH Ti-6Al-4V parts.

8.1.2 Cylindrical component

Hot-repressing and extrusion of HDH titanium powder compacts were carried out to produce a cylindrical titanium component. A hot-repressing method of powder

consolidation is of interest in the production of high performance titanium fastener products. The experimental results showed that cylindrical components with a high and uniform density can be produced by this method. The higher density is achieved because of the hydrostatic pressure generated in the powder compact when forged in a confined die. This can be explained by the fact that the yielding behaviour of any porous material is sensitive to the applied hydrostatic stresses. With the application of compressive hydrostatic stresses, the pores within the material will collapse resulting in higher densification. Due to the design of the process which includes combined hot-repressing and extrusion, the density increases at the extrusion die radii during the initial stages of the process. After the forward leg region is filled, the hydrostatic pressure increases in the rest of the component. A uniform density was seen throughout the component, except at the bottom leg, where the lowest measured relative density was 0.98.

Despite success in producing cylindrical titanium fastener grade components in the laboratory scale experiments, manufacturing to industrial trials did not move forward for the following reasons (1) The high hydrostatic pressure and temperature involved in the process exerts high stresses beyond the yield stress of the die material. Also, the original design for this product had a hole at the top end as shown in figure 7.1. The tooling material failed on several occasions during backward extrusion of the product. (2) Critical structural components such as fasteners rely on standardisation and material traceability for safety and reliability. At the time the experiments were being carried out there was no standardisation for non-melt P/M titanium structural materials available for a specialised process such as the hot-pressing. This situation has since changed with the introduction of a new ASTM B988-13 specification for P/M titanium for structural components, published in July 2013 [130]. The release of these new standards is expected to facilitate wider industrial application of titanium P/M products with reduced cost and lead time. However, only a few HDH titanium powder manufacturers are currently able to meet these new standards.

8.1.3 Ring shaped titanium component

A closed die powder forging route was used to produce an HDH titanium ring shaped part. The material flowed outwards during the powder forging operation. The highest relative density was seen at the centre of the component and this reduced towards the edge. A lack of uniformity in density in the HDH titanium powder compact was a major concern. The non-uniform density distribution was due to the varying horizontal cross section of the powder compact and problems in uniform die filling in the experimental compaction die setup. The die filling problem can be solved by re-designing the die such that the filling depth is equal to the depth of the compaction die cavity. During the experimental trials, radial cracks were seen in the final powder compact forged part. The reason for the occurrence of these cracks was due to improper bottom die design which led to high radial stresses applied to the powder compact (revealed by the simulation) during the early stages of powder forging.

Powder compact forging trials were not successful in producing sound ring shaped titanium forgings. This was because of cracking during forging and a requirement for a specialised argon or vacuum chamber for industrial production trials. As an alternative approach a sinter-powder forging route was used for this the HDH titanium powder compacts were sintered in a vacuum furnace and powder forged in air. No cracks were seen in sinter-forged titanium powder compacts; this might have been because of higher densification of the powder compacts after vacuum sintering. It is interesting to point out that an increase in densification through vacuum sintering increases the fracture strain limits of the powder compacts during forging [131].

8.2 Material model

The Gurson porous metal plasticity model was evaluated in this study with Abaqus/standard and Abaqus/Explicit. Although there is a lot of available literature on the densification modelling of powder metals using the Gurson model, only a few address the implications of the Tvergaard material parameters on the modelling of processes such as powder forging. An initial case study was performed to test the accuracy of the material model in predicating the relative density at two different deformation percentages. From the study, it was found that the actual density obtained

after forging was higher than the predicted density, especially at the peripheral region. To improve the accuracy of the model prediction, parameters suggested by Tvergaard were studied. The parameters for HDH titanium and Ti-6Al-4V titanium powder were obtained by a computational procedure suggested by Cheng et. al. [13]. The essential objective of this research was to establish a simulation procedure for prediction of relative density during powder forging. The present work has simulated the densification behaviour of three different powder forged titanium component using Gurson and Gurson-Tvergaard models. Three different modes of densification regimes were studied i.e. upset forging, Hot-repressing and closed die forging. The actual density was measured by gamma-particle density measuring technique. The results were then compared with the simulated densities given by the Gurson and Gurson-Tvergaard models. The simulated density predictions with the Gurson-Tvergaard model were similar to the measured densities.

8.3 Gurson-Tvergaard model parameters

The parameter q_1 influences the yield behaviour of the material by modifying the initial void volume fraction. A higher value of q_1 lowers the stress carrying ability of the porous material matrix. If q_1 is greater than 1.0 during upsetting, the material experiences a reduced stress condition. A typical range of values for q_1 taken from the literature was between 1.0 and 2.0 [4, 12, 13, 78], which differ from the value (q_1 =1.5) suggested by Tvergaard [77]. Several reports in the literature predict instability problems with q_1 greater than 1.5 because this induces stronger softening behaviour of the porous material. No such issues were encountered in this study. Such instabilities have been reported during void nucleation and may not affect void collapse during forging, as in this study [78]. The parameter q_2 acts as a correcting factor for the hydrostatic pressure component of the porous material. A higher value of q_2 affects the deformation behaviour of the material by reducing its yield strength and influencing the evolution of voids. In contrast to q_1 and q_2, the values for the parameter q_3 had no significant effect on deformation and densification behaviour. However, a higher value of q_3 above 2.5 for induced convergence problems and caused the program to exit without fully solving.

For the circular disc, the density prediction given by the Gurson-Tvergaard model agreed closely with the measured results at the centre, but underestimated the densification taking place at the circumference. The density predictions from the Gurson-Tvergaard model, when compared with the calculated parameters for hot-repressed cylindrical and ring shaped components, showed better agreement than those given by the Gurson model. However, the measured densities were slightly higher than the simulated ones.

8.4 Discussion on model accuracy

The accuracy of results obtained by numerical modelling are limited by the assumptions made in this work.

8.4.1 Initial relative density of the powder compacts

In the simulation, the initial relative density was assumed to be uniform though out the powder compact, however in actual powder compacts the porosity distribution was non-uniform as can be seen from figure 5.8. Similar assumptions were made in the initial densities of the samples used in the Gleebal tests. In order to reduce this discrepancy, the density distribution can be defined in Abaqus as a “predefined field input” option, if the initial compact densities are known.

8.4.2 Initial compact temperature

In the simulation, the initial powder compact temperature was assumed to be uniform. However, in reality temperature varies depending on the density distribution. For example the regions with higher density heat up faster than the regions with lower density within the powder compact. This assumption can reduce the accuracy of the result as the flow stresses of the material is defined with respect to the temperature.

8.4.3 Induction sintering effect on density

It is known that when the powder compact is induction sintered the density increases due to thermally activated grain growth. This increment in relative density has not been considered in the models used in this study. The densification effect by induction sintering can be modelled by an extension of the original Gurson model such as

Gurson-Fleck model [133] which takes into account of thermally induced densification.

8.4.4 Pore geometry

In both Gurson and Gurson Tvergaard model the porosity is assumed as spherical or cylindrical, however, in reality the pores are irregular in shapes as can be seen in figure 5.10. This does not have any substantial implication on the result that are industrially significant for powder forging process. There are no literature available that illustrates a numerical model that can take into account of the irregular pore geometry.

8.4.5 Computational issues and efficiency

Implementation of the Gurson-Tvergaard model was computationally intensive. The average solution time for a problem using the Gurson-Tvergaard model in Abaqus/standard was 8 to 10 hours using an acceptable mesh quality with a computer with a 12 gigabyte RAM capacity. The solution time was significantly reduced to 4 to 6 hours using Abaqus/explicit for the cylindrical and titanium ring shaped components. An admittedly unfavourable criticism of such inclusive constitutive material modelling is in getting the right balance between accuracy and computational efficiency. For the simulation of an industrial powder forging problem, that supports improved die design and material flow, it would be more convenient to have a model that provides valuable results at a reasonable computational cost.

9 Future work and suggestions

9.1 Forging simulation

The need for fast and reliable simulation is required to aid economical manufacture. Forging simulation is no longer niche in the forging industry and has established itself over the years through quick and accurate results. An effective simulation capability requires a critical balance between accuracy, flexibility, ease of use and speed so that experimenting with different forging scenarios is quick, simple and reliable. From the present research, two barriers were identified that restrict the use of simulations when applied in industrial situations. Firstly the deformation in forging simulation is often large, thus a robust meshing algorithm is required. An ideal mesh should be non-uniform and re-generating to ensure higher accuracy during deformation. The speed of mesh regeneration is a major consideration when temperature elements are involved in a problem solution; if mesh regeneration is too slow it could lead to significant computational time. Secondly, there are material modelling limitations, as the material used in forging simulation requires significant information for predicting accurate results. When material data is not available, it is common practice to calibrate and develop new models. Also it is interesting to point out that, although improved material models may provide better results, they are more computationally intensive.

9.2 Future consideration in material modelling

Although Gurson and Gurson Tvergaard models were successful in predicting relative densities, the results can be further improved. For future work, there are some key recommendations which can be made from this research:

- The development and implementation of a porous metal plasticity model that enables densification predictions considering the effects of initial compact density, temperature and thermally activated densification during induction sintering.
- The present study did not investigate fracture of powder compacts during forging. Gurson-Tvergaard-Needleman model which considers localised ductile damage needs to be further investigated further.

9.3 Future considerations for densification modelling in powder forging

In this research, although the Gurson and the Gurson-Tvergaard models were successfully used in Abaqus standard and explicit to predict densification for a selected geometry, a more complex powder forging scenario would require numerous re-meshings as the material deforms. In Abaqus, once the re-mesh option is selected the software re-meshes the entire component instead of only the region where large deformation occurs. The existing re-meshing capability in Abaqus software leads to higher computational times. Abaqus software is expensive and is a general purpose FEA software which demands a lot of time to learn. Therefore its use in an industrial context might be difficult. Therefore there is a need and therefore interest in custom FEA programs that have a more specific build to solve problems related to forging. However, such a shift is only possible after known general FEA software has been successfully applied in the solution of a problem.

Deform 3D is a custom software to solve problems related to bulk metal forming. The fundamental idea of meshing in Deform 3D is based on the idea of separately creating a mesh on the surface of a deforming body and within its volume. The two standard meshing techniques available in Deform 3D are Eulerian and Lagrangian. Desirable results are obtained by a combination of Arbitary Lagrangian Eulerian and coupled Lagrangian mesh. The iterative solvers that are integrated in Deform have been optimised for problems with a Lagrangian mesh, with faster solution times. The densification model available in Deform 3D is based on a modified Shima and Oyane criterion. The Gurson model has an edge over the Shima and Oyane model available in Deform 3D as the former is able to predict small variation in relative density. Also, the Shima and Oyane model is only accurate for problems with an initial relative density above 0.9, however it overestimates densification. Figure 9.1 shows the implementation of the Gurson model in Deform 3D and Abaqus. The Gurson and Gurson-Tvergaard models can be implemented in Deform 3D using a user-subroutine.

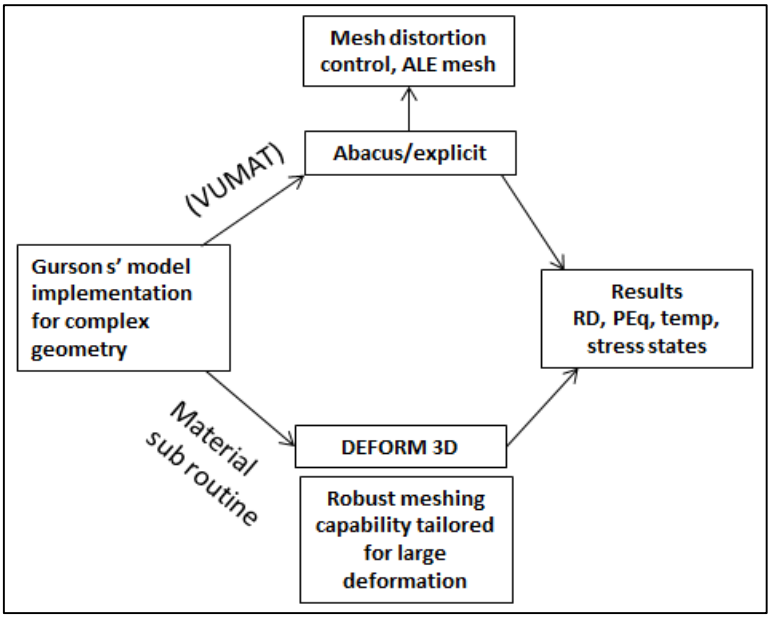

Figure 9.1: Implementation scheme for the Gurson model in Abaqus and Deform 3D

Figure 9.2 shows an example of a deformation problem solved in Deform 3D using an advanced re-meshing technique.

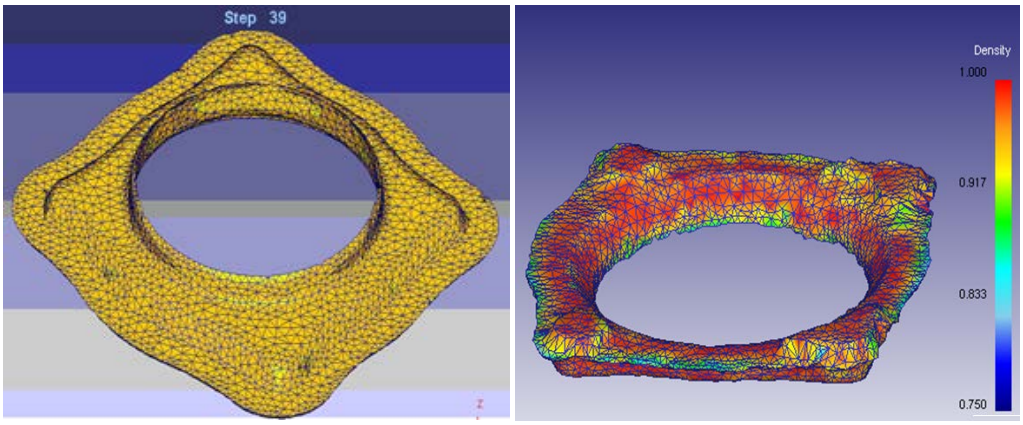

Figure 9.2: Deformation and density prediction in a ring shaped titanium component solved in Deform 3D

9.4 Workability of HDH titanium powder compacts

The workability of porous powder compacts is an important parameter that needs to be considered in the designing of a powder forging process. Historically, workability criteria during a forging operation are usually based on localised strain determined from compressive and tensile tests. The forming limits are determined based on the tensile strains observed during the forging operation. For instance, when the tensile strain during the forging operation exceeds the experimentally determined tensile fracture strain of the material, then the material can no longer be formed into a useful

shape without cracking. However, for a porous material, such as a titanium powder compact, a critical fracture strain is not the only criterion that determines cracking or fracture. It is known from the literature that relative density is also a limiting factor when forming powder compacts [131, 132]. This is because fracture is dependent on the ductility of the material and localised tensile strain. At lower initial relative densities, increasing porosity leads to a decrease in ductility. On the other hand, an increase in porosity will decrease the areas of contact between powder particles, so that the stress will increase.

Thus, it is important to determine the critical fracture strain, as a function of relative density and compressive height reduction to avoid an occurrence of fracture. Also, the critical tensile fracture strain in a uniaxial tensile test is required at different relative densities. As the Gurson model was originally developed to model failure of ductile materials with significant porosity, it is understood that a decrease in relative density (increase in void volume fraction) can be interpreted as void nucleation that would lead to crack formation. However, this is not certain until a critical void volume fraction that leads to failure of the material is determined. Improved workability criteria can be proposed using an extension of the Gurson-Tvergaard model such as the Gurson-Tvergaard-Needleman (GTN) model. In this model a critical void volume fraction and fracture void volume fraction are related. These two nucleation parameters can be determined by performing uniaxial tensile tests.

9.5 Selective densification, sizing and multi-step powder forging operation for improved densification

The mechanical properties of titanium alloys depend on density, microstructure and composition. Obtaining high density is the highest priority in many powder metallurgical manufacturing techniques. However, in many applications it is acceptable to densify just the high stress regions of the part that bear the maximum service stresses. In the powder metallurgy of ferrous alloys, it is well established practice to increase sintered densities by selective surface densification to improve dynamic mechanical properties, such as impact toughness and fatigue. However, not many studies have been carried out to help us to understand the influence of selective densification on P/M titanium alloys.

From the simulation results presented in this work it is clear that obtaining uniform densification is difficult if not impossible to achieve by a single forging operation. The problem arises for several reasons, such as low starting powder compact density, powder morphology, frictional factors, heat losses and complex material flow involved in the die etc. A multi-step forging operation would be a good option for enhancing densification. However, the deformation and densification behaviour during multi-step powder forging needs further study.

10 References

[1] F. H. Froes, S. J. Mashl, J. C. Hebeisen, V. S. Moxson, and V. A. Duz, "The technologies of titanium powder metallurgy," *Journal of the Minerals Metals*, vol. 56, pp. 46-49, 2004.

[2] H. A. Kuhn and B. L. Ferguson, *Powder Forging*. Princeton New Jersey: Metal powder industries federation, 1990.

[3] R R Irving. (1986, 17 March). *Powder forging makes a comeback after a shaky start*.

[4] S. H. Chung, Y. S. Kwon, S. J. Park, and R. M. German, *Modeling and Simulation of Press and Sinter Powder Metallurgy* vol. 22: ASM Handbook, 2010.

[5] A. Kaushik, K. Ibrahim, and A. Srinivasa., "Simulation of powder compaction using equal channel angular extrusion at room temperature: Comparison of two constitutive theories," *International journal of structural changes in solids – mechanics and applications,* vol. 1, pp. 211-226, 2009.

[6] R S Ransing, I Cameron, N P Lavery, A R Khoei, R W Lewis, and D. T. Gethin., "Powder compaction modeling and material characterization," in *Workshop Modeling Metal Powder Forming Processes,* Grenoble, France, 1997, pp. 189-201.

[7] A. L. Gurson and E. S. Bono., "A Modeling System to Simulate the Compaction of Powder Metals," *Advances in Powder Metallurgy & Particulate Materials,* vol. 2, pp. 443-455, 1996.

[8] A. L. Gurson, "Continuum Theory of Ductile Rupture by Void Nucleation and Growth: Part I—Yield Criteria and Flow Rules for Porous Ductile Media," *Journal of Engineering Materials and Technology,* vol. 99, pp. 2-15, 1977.

[9] M. Gologanu, J.-B. Leblond, G. Perrin, and J. Devaux, "Recent extensions of Gurson's model for porous ductile metals," in *Continuum micromechanics*, ed: Springer-Verlag New York, Inc., 1997, pp. 61-130.

[10] V. Tvergaard and A. Needleman., "Analysis of the cup-cone fracture in a round tensile bar," *Acta Metallurgica,* vol. 32, pp. 157-169, 1// 1984.

[11] A. Needleman and V. Tvergaard, "An analysis of ductile rupture in notched bars," *Journal of the Mechanics and Physics of Solids,* vol. 32, pp. 461-490, // 1984.

[12] E. Parteder, H. Riedel, and R. Kopp., "Densification of sintered molybdenum during hot upsetting: experiments and modelling," *Materials Science and Engineering: A,* vol. 264, pp. 17-25, 5/31/ 1999.

[13] C. Huang and J. Cheng, "Forging simulation of sintered powder compacts under various frictional conditions," *International Journal of Mechanical Sciences,* vol. 44, pp. 489-507, 3// 2002.

[14] M.T. Jia, D. L. Zhang, and B. Gabbitas., "Comparison of Blended Elemental (BE) and Mechanical Alloyed (MA) Powder Compact Forging into Ti-6Al-4V Rocker Arms," *Key Engineering Materials,* vol. 520, pp. 82-88, 2012.

[15] M. Yamada, "An overview on the development of titanium alloys for non-aerospace application in Japan," *Journal of Mater Science Engineering,* vol. A, p. 213, 1996.

[16] C. Leyens and M. Peters, "Titanium and Titanium alloys: Fundamentals and Applications," *WILEY-VCH Verlag GmbH and Co KGaA,* vol. 305, pp. 34-43, 2003.

[17] M. Jackson and K. Dring, "A review of advances in processing and metallurgy of titanium alloys," *Journal of Material Science and Technology,* vol. 22, pp. 881-887, 2006.

[18] M. M. Abdallah, "Corrosion of titanium and zinc alloy in Dead Sea water, anti-corrosion methods," *Journal of Materials,* vol. 43, pp. 17–22., 1996.

[19] Z. Han, H. Zhao, X. F. Chen, and H. C. Lin, "Corrosion behaviour of Ti–6Al–4V alloywelded by scanning electron beam," *Journal of Mater. Sci. Eng.,* vol. A277, pp. 38-45, 2000.

[20] F. H. Froes, D. Eylon, and H. B. Bomberger, "Titanium Technology: Current Status and Future Trends," Dayton, OH, 1985.

[21] Z. Zak Fang, "Powder Metallurgy Titanium-Challenges and Opportunities," *International Journal of Powder Metallurgy,* vol. 46, 2010.

[22] S. Abkowitz, A. S. M, M. D, and M. T, "The New Era In Titanium Manufacturing - Powder Metal Components," in *AeroMat,* 2011.

[23] S. Sun, J. Harris, and M. Brandt, "Parametric Investigation of Laser-Assisted Machining of Commercially Pure Titanium," *Advanced Engineering Materials,* vol. 10, pp. 565-572, 2008.

[24] C. Leyens and M. Peters, *Titanium and Titanium Alloys*: Wiley, 2006.

[25] J. E. Barnes, W. Peter, and C. Blue., "Evaluation of Low Cost Titanium Alloy Products," *Materials Science Forum,* vol. 618-619, pp. 165-168, 2009.

[26] F. H. Froes and D. Eylon, "Powder metallurgy of titanium alloys," *International Materials Review,* pp. 162-190, 1990.

[27] H. A. Kuhn and C. L. Downey, "Deformation characteristics and plasticity theory of sintered powder materials," *International Journal of Powder Metallurgy,* vol. 7, pp. 15-25, 1971.

[28] S. L. Semiatin, "ASM Metals Handbook, ASM international," *Forming and Forging,* vol. 14, 1988.

[29] F. T. Lally, I. J. Toth, and J. DiBenedetto, "Forged metal powder products," in *Progress in Powder Metallurgy, MPIF,* New York, 1972, pp. 276-302.

[30] H. Halverson. (2010, 12 October). *Ruthless Pursuit of Power*.

[31] R. M. German, "Powder metallurgy and particulate Materials Processing," in *Metal Powder Industries Federation,* New Jersey USA, 2005.

[32] Z. Zhang, "Simulation of Titanium and Titanium Alloy Powder Compact Forging," Master of Engineering, School of Engineering, University of Waikato, Hamiton, New Zeland, 2011.

[33] B. L. Ferguson and G. I. Friedman, "Forging of prealloyed 9310 steel powder," *TRW TM-4944,* 1986.

[34] K T Kim and H. C. Yang, "Densification behavior of titanium alloy powder during hot pressing," *Materials Science and Engineering: A,* vol. 313, pp. 46-52, 8/31/ 2001.

[35] I. Weiss, D. Eylon, M. W. Toaz, and F. H. Froes., "Effect of isothermal forging on microstructure and fatigue behavior of blended elemental Ti-6Al-4V powder compacts," *Metallurgical Transactions A,* vol. 17, pp. 549-559, 1986/03/01 1986.

[36] Z. Zhao, H. Guo, X. Wang, and Z. Yao., "Deformation behavior of isothermally forged Ti–5Al–2Sn–2Zr–4Mo–4Cr powder compact," *Journal of Materials Processing Technology,* vol. 209, pp. 5509-5513, 8/1/ 2009.

[37] J.W. Qiu, Y. Liu, B. Liu, B. Wang, Earle Ryba, and H. P. Tang., "Optimizing the hot-forging process parameters for connecting rods made of PM titanium alloy," *Journal of Materials Science,* vol. 47, pp. 3837-3848, 2012.

[38] W H. Peter and Y. Yamamoto, "Near Net Shape Manufacturing of New, Low Cost Titanium Powders for Industry," Oak Ridge National Laboratory, Springfield2013.

[39] M. N. Gungor, M. Ashraf Imam, and F. H. Froes, *Innovations in Titanium Technology*. Warrendale, Pa: TMS, 2007.

[40] O. Ivasishin, D. Savvakin, D. Drozdenko, A. Petrunko, V. Moxson, and F. Froes., "Manufacture of near-net shape titanium alloy articles from metal powders by sintering at variable pressure," ed: Google Patents, 2003.

[41] V.A. Duz, O.M. Ivasishin, V.S. Moxson, D.G. Savvakin, and V. V. Telin., "Cost-effective titanium alloy powder compositions and method for manufacturing flat or shaped articles from these powders," ed: Google Patents, 2009.

[42] R. Oberacker, "Powder Compaction by Dry Pressing," in *Ceramics Science and Technology*, ed: Wiley-VCH Verlag GmbH & Co. KGaA, 2011, pp. 1-37.

[43] W. Chen, Y. Yamamoto, W. H. Peter, S. B. Gorti, A. S. Sabau, M. B. Clark, *et al.*, "Cold compaction study of Armstrong Process® Ti–6Al–4V powders," *Powder Technology,* vol. 214, pp. 194-199, 12/10/ 2011.

[44] P. J. James, "Fundamental aspects of the consolidation of Powders," *Powder Met.Int,* vol. 4, pp. 82-85, 1972.

[45] I. Weiss, R. Srinivasan, P.J. Bania, D. Eylon, and S. L. Semiatin., "Advances in the Science and Technology of Titanium Alloy Processing," *The Minerals, Metals & Materials Society,* 1996.

[46] K.H. Huebner, *The Finite Element Method for Engineers*: Wiley, 2001.

[47] P V Marcal and I. P. King, "Elastic-plastic analysis of two-dimensional stress systems by the finite element method," *international Journal of Mechanical Science,* vol. 9, pp. 143-155, 1967.

[48] J de Arizon, E Filippi, J Barboza, and L. D'Alvise, "A Finite Element simulation of the hot forging process," *National Congress on Theoretical and Applied Mechanics* 2006.

[49] G Ngaile and T. Altan, "Computer Aided Engineering in Forging," in *International Seminar on Precision Forging*, Japan, 2004.

[50] V Vasquez and T. Altan, "New concepts in die design – physical and computer modeling applications," *Materials Processing Technology,* vol. 98, pp. 212-223, 2000.

[51] J. E. Jackson and M. S. Ramesh., "The rigid-plastic finite-element method for simulation of deformation processing," in *Numerical modeling of material deformation processes: research, development and applications*, London, 1992.

[52] M. Yongning, "Forging process design for disc reduction," Phd thesis, Industrial and Systems Engineering, The Ohio State University, Ohio, 2009.

[53] W A M Brekelmans, J D Janssen, A A F Van de Ven, and G. de., "An Eulerian approach for die compaction processes," *International Journal for Numerical Methods,* vol. 31, pp. 509-524, 1991.

[54] H A Haggblad and M. Oldenburg, "Modelling and simulation of metal powder die pressing with use of explicit time integration," *Modelling and Simulation in Material Science Engineering,* vol. 2, pp. 893-911, 1994.

[55] J. Oliver, S Oiler, and J. C. Cante, "A plasticity model for simulation of industrial powder compaction processes," *International Journal of Solid Structures,* vol. 33, pp. 3161-3178, 1996.

[56] K. Osakada, J. Nakano, and K. Mori, "Finite element method for rigid-plastic analysis of metal forming-formulation for finite deformation," *International Journal of Mechanical Science,* vol. 24, pp. 459-468, 1982.

[57] K. Mori and K. Osakad, "Analysis of the forming process of sintered powder metals by a rigid-plastic finite-element method," *International Journal of Mechanical Science,* vol. 29, pp. 229-238, 1987.

[58] J. Huang, W. Xu, P. Thomson, and S. Di, "A general rigid-plastic/rigid-viscoplastic FEM for metal-forming processes based on the potential reduction interior point method," *International Journal of Machine Tools and Manufacture,* vol. 43, pp. 379-389, 2003.

[59] S Kobayashi, S Oh, and T. Alatan, "Metal Forming and the Finite Element Method," in *Oxford University Press*, Oxford, UK, 1989.

[60] A. C. F. Cocks, "Inelastic deformation of porous materials," *Journal of the Mechanics and Physics of Solids,* vol. 37, pp. 693-715, // 1989.

[61] P. Sofronis and R. M. Mcmeeking., "Creep of Power-Law Material Containing Spherical Voids," *Journal of Applied Mechanics,* vol. 59, pp. S88-S95, 1992.

[62] J. C. Michel and P. Suquet., "The constitutive law of nonlinear viscous and porous materials," *Journal of the Mechanics and Physics of Solids,* vol. 40, pp. 783-812, 5// 1992.

[63] A R Khoei, *Computational Plasticity in Powder Forming Processes*. London: Elsevier, 2005.

[64] J. L. Chenot, F. Bay, and L. Fourment, "Finite element simulation of metal powder forming," *International Journal for Numerical Methods,* vol. 31, pp. 1649-1674, 1990.

[65] C D Turner, "A micromechanical model of multiaxial powder densification," presented at the Powder Metallurgy World Congress, Paris, 1994.

[66] T. Strouboulis, K. Copps, and I. Babuska, "The generalized finite element method," *Computer Methods in Applied Mechanics and Engineering,* vol. 190, pp. 4081–4193, 2001.

[67] T Pardoen, I Doghri, and F. Delannay., "Experimental and numerical comparison of void growth models and void coalescence criteria for the prediction of ductile fracture in copper bars," *Acta Materialia,* vol. 46, pp. 541–552, 1998.

[68] R. J. Green, "A plasticity theory for porous solids," *international Journal of Mechanical Science,* vol. 14, pp. 215-224, 1972.

[69] S. Shima and M. Oyane, "Plasticity theory for porous metals," *International Journal of Mechanical Science,* vol. 18, pp. 285-291, 1976.

[70] S. M. Doraivelu, H. L. Gegel, J. S. Gunasekera, J. C. Malas, J. T. Morgan, and J. F. Thomas, "A new yield function for compressible P/M materials," *International Journal of Mechanical Science,* vol. 26, pp. 527-535, 1984.

[71] M. Oyane, S. Shima, and Y. Kono, "Theory of plasticity for porous metals," *Bulletin of the Japanese Society of Mechanical Engineers,* vol. 16, pp. 1254-1262, 1973.

[72] J. Svoboda, H. Riedel, and R. Gaebel, "A model for liquid phase sintering," *Acta Materialia,* vol. 44, pp. 3215-3226, 8// 1996.

[73] Y. Wu and G.-Y. Kim, "Compaction behavior of Al6061 powder in the semi-solid state," *Powder Technology,* vol. 214, pp. 252-258, 12/10/ 2011.

[74] H. Honess, "Investigation of plastic deformation characteristics of sintered iron at room temperature," *Powder Met.Int,* vol. 9, pp. 170-173, 1977.

[75] N A Fleck, L T Kuhn, and R. M. Mcmeeking., "Yielding of metal powders bonded by isolated contacts," *Journal of the Mechanics and Physics of Solids,* vol. 40, p. 1139, 1992.

[76] M. Abouaf, J L Chenot, G Raisson, and P. Bauduin, "Finite element simulation of hot isostatic pressing of metal powders," *International Journal for Numerical Methods,* vol. 25, pp. 191-212, 1988.

[77] V. Tvergaard, "On localization in ductile materials containing spherical voids," *International Journal of Fracture,* vol. 18, pp. 237-252, 1982/04/01 1982.

[78] M. Springmann and M. Kuna., "Identification of material parameters of the Gurson–Tvergaard–Needleman model by combined experimental and numerical techniques," *Computational Materials Science,* vol. 33, p. 500, 2005.

[79] G. Perrin and J. B. Leblond., "Analytical study of a hollow sphere made of plastic porous material and subjected to hydrostatic tension-application to some problems in ductile fracture of metals," *International Journal of Plasticity,* vol. 6, pp. 677-699, // 1990.

[80] D. J. Benson, "An analysis of void distribution effects on the dynamic growth and coalescence of voids in ductile metals," *Journal of the Mechanics and Physics of Solids,* vol. 41, pp. 1285-1308, 8// 1993.

[81] C.A. Berg, *Plastic Dilatation and Void Interaction*: MIT, 1969.

[82] J. R. Rice and D. M. Tracey., "On the ductile enlargement of voids in triaxial stress fields∗," *Journal of the Mechanics and Physics of Solids,* vol. 17, pp. 201-217, 6// 1969.

[83] F. A. McClintock, "A Criterion for Ductile Fracture by the Growth of Holes," *Journal of Applied Mechanics,* vol. 35, pp. 363-371, 1968.

[84] W. Rohsenow, J.P. Hartnett, and Y. I. Cho., *Handbook of Heat Transfer*: McGraw-Hill Education, 1998.

[85] F. P. Bowden and D. Tabor., *The friction and lubrication of solids*. Oxford: Clarendon Press, 1950.

[86] N. Bay and T. Wanheim., "Real area of contact and friction stress at high pressure sliding contact," *Wear,* vol. 38, pp. 201-209, 7// 1976.

[87] S. P. Shenoy. (2013) Lubricant Choices and Forging Cost. *Forging magazine*.

[88] E. Orowan, "The Calculation of Toll Pressure in Hot and Cold Flat Rolling," *Proceedings of Institutional Engineers Symposium,* vol. 67, pp. 140–150, 1943.

[89] R.M. McMeeking and L. T. Kuhn., "A diffusional creep law for powder compacts," *Acta metallurgica et materialia,* vol. 40, pp. 961-969, 1992.

[90] R. Weyler, J. Oliver, T. Sain, and J. C. Cante., "On the contact domain method: A comparison of penalty and Lagrange multiplier implementations," *Computer Methods in Applied Mechanics and Engineering,* vol. 205–208, pp. 68-82, 1/15/ 2012.

[91] K. Hibbitt and Sorensen, *ABAQUS/CAE User's Manual*: Hibbitt, Karlsson & Sorensen, Incorporated, 2001.

[92] K. Hibbitt and Sorensen, *Getting started with ABAQUS/Explicit*: Hibbitt, Karlsson & Sorensen, Inc., 1998.

[93] M. Abo-Elkhier, "Elasto-plastic finite element modelling of strip cold rolling using Eulerian fixed mesh technique," *Finite Elements in Analysis and Design,* vol. 27, pp. 323-334, 11/15/ 1997.

[94] S. Wang, B. C. Khoo, G. R. Liu, and G. X. Xu., "An arbitrary Lagrangian–Eulerian gradient smoothing method (GSM/ALE) for interaction of fluid and a moving rigid body," *Computers & Fluids,* vol. 71, pp. 327-347, 1/30/ 2013.

[95] M. S. Gadala, M. R. Movahhedy, and J. Wang., "On the mesh motion for ALE modeling of metal forming processes," *Finite Elements in Analysis and Design,* vol. 38, pp. 435-459, 3// 2002.

[96] J. L. F. Aymone, E. Bittencourt, and G. J. Creus., "Simulation of 3D metal-forming using an arbitrary Lagrangian–Eulerian finite element method," *Journal of Materials Processing Technology,* vol. 110, pp. 218-232, 3/19/ 2001.

[97] R. Zhou, L. Zhang, B. He, and Y. Liu., "Numerical simulation of residual stress field in green power metallurgy compacts by modified Drucker–Prager Cap model," *Transactions of Nonferrous Metals Society of China,* vol. 23, pp. 2374-2382, 8// 2013.

[98] S. Shima and M. Oyane., "Plasticity theory for porous metals," *International Journal of Mechanical Sciences,* vol. 18, pp. 285-291, 6// 1976.

[99] M. Jeong, J. Yoo, S. Rhim, S. Lee, and S. Oh., "A unified model for compaction and sintering behavior of powder processing," *Finite Elements in Analysis and Design,* vol. 53, pp. 56-62, 6// 2012.

[100] J.R. Davis, *ASM Specialty Handbook.* Metals Park, OH.: ASM International, 1996.

[101] Z. Zhang, "Simulation of titanium and titanium alloy powder compact forging," Masters Thesis, School of Engineering, University of Waikato, Hamilton, 2011.

[102] G. S. Wagle, R. S. Engel, R. M. German, and Y. Liu, "Numerical nvestigation of onstitutive models for the powder compaction process," *Advances in Powder Metallurgy & Particulate Materials,* pp. 13-24, 2000.

[103] N. Aravas, "On the numerical integration of a class of pressure-dependent plasticity models," *International Journal for Numerical Methods in Engineering,* vol. 24, pp. 1395-1416, 1987.

[104] W. Wang, "Towards an improved understanding of strength and anisotropy of cold compacted powder," College of Engineering, Drexel University, Philadelphia, Pa., 2007.

[105] Z. Xue, M. G. Pontin, F. W. Zok, and J. W. Hutchinson., "Calibration procedures for a computational model of ductile fracture," *Engineering Fracture Mechanics,* vol. 77, pp. 492-509, 2// 2010.

[106] J. M. Duva and P. D. Crow., "The densification of powders by power-law creep during hot isostatic pressing," *Acta Metallurgica et Materialia,* vol. 40, pp. 31-35, 1// 1992.

[107] S. B. Biner and W. A. Spitzig., "Densification of iron compacts with various initial porosities under hydrostatic pressure," *Acta Metallurgica et Materialia,* vol. 38, pp. 603-610, 4// 1990.

[108] P. T. Wang and M. E. Karabin., "Evolution of porosity during thin plate rolling of powder-based porous aluminum," *Powder Technology,* vol. 78, pp. 67-76, 1// 1994.

[109] E. Parteder, H. Riedel, and D. Sun., "Simulation of hot forming processes of refractory metals using porous metal plasticity models," *International Journal of Refractory Metals and Hard Materials,* vol. 20, pp. 287-293, 7// 2002.

[110] Z. Malinowski, J. G. Lenard, and M. E. Davies., "A study of the heat-transfer coefficient as a function of temperature and pressure," *Journal of Materials Processing Technology,* vol. 41, pp. 125-142, 1994.

[111] F. Yang, D. L. Zhang, B. Gabittas, and H. Y. Lu., "Effect of Powder Compact Holding Time on the Microstructure and Properties of Ti-6Al-4V Alloy Produced by Powder Compact Extrusion of a Powder Mixture of HDH Titanium and Al-V Master Alloy," *Key Engineering Materials: Cost-Affordable Titanium IV,* pp. 67-72, 2013.

[112] B. Buchner, G. Maderthoner, and B. Buchmayr, "Characterisation of different lubricants concerning the friction coefficient in forging of AA2618," *Journal of Materials Processing Technology,* vol. 198, pp. 41-47, 3/3/ 2008.

[113] A. Tomala, S. Hernandez, M. Rodriguez Ripoll, E. Badisch, and B. Prakash, "Tribological performance of some solid lubricants for hot forming through laboratory simulative tests," *Tribology International,* 2014.

[114] V. Tvergaard, "Effect of yield surface curvature and void nucleation on plastic flow localization," *Journal of the Mechanics and Physics of Solids,* vol. 35, pp. 43-60, // 1987.

[115] M. Gologanu, J. B. Leblond, and J. Devaux., "Approximate models for ductile metals containing nonspherical voids—case of axisymmetric oblate ellipsoidal cavities," *Journal of Engineering Materials and Technology,* vol. 116, p. 7, 1994.

[116] B. Budiansky, J. W. Hutchinson, and S. Slutsky., "Void growth and collapse of viscous solids," *The mechanics of solids,* pp. 13-45, 1982.

[117] M. Gologanu, J. B. Leblond, G. Perrin, and J. Devaux., "Recent extensions of Gurson's model for porous ductile metals," in *Continuum micromechanics,* ed: Springer-Verlag New York, Inc., 1997, pp. 61-130.

[118] B. A. Yazici, T. Kraft, and H. Riedel., "Finite element modelling of PM surface densification process," *Powder Metallurgy,* vol. 51, pp. 211-216, 2008.

[119] B. J. Lee and M. E. Mear, "An evaluation of Gurson's theory of dilatational plasticity," *Journal of Engineering Materials and Technology, Transactions of the ASME,* vol. 115, p. 44, 1993.

[120] P. Ponte Castañeda and M. Zaidman, "Constitutive models for porous materials with evolving microstructure," *Journal of Mechanics of physics of solids,* vol. 42, pp. 1459–1497, 1994.

[121] N. D.Karsu, S. Yüksel, and M. Güden, "Foaming behavior of Ti6Al4V particle-added aluminum powder compacts," *Journal of Materials Science,* vol. 44, pp. 1494-1505, 2009/03/01 2009.

[122] R. Chaudhari and R. Bauri., "Microstructure and Mechanical Properties of Titanium Processed by Spark Plasma Sintering (SPS)," *Metallography, Microstructure, and Analysis,* vol. 3, pp. 30-35, 2014/02/01 2014.

[123] M. Yi, H. Yin, J. Wang, X. Yuan, and X. Qu., "Comparative research on high-velocity compaction and conventional rigid die compaction," *Frontiers of Materials Science in China,* vol. 3, pp. 447-451, 2009/12/01 2009.

[124] ASTM, "B328 Standard Test Method for Density, Oil Content, and Interconnected Porosity of Sintered Metal Structural Parts and Oil-Impregnated Bearings," in *American Society for Testing and Materials,* ed, 2003.

[125] MPIF, "Determination of Density of Compacted or Sintered Powder Metallurgy Products," in *Metal Powder Industries Federation,* ed, 2009.

[126] ISO, "Sintered metal materials, excluding hardmetals - Permeable sintered metal materials - Determination of density, oil content and open porosity," in *International Organization for Standardization* vol. 2739, ed, 1999.

[127] G. G. Weber and S. B. Brown, "Simulation of the compaction of powder components," *Advances in Powder Metallurgy and Particulate Materials,* vol. 1, 1989.

[128] M. D. Riera and J. M. Prado, "Uniaxial Compression Tests on Powder Metallurgical Compacts," *Proceedings of the 1998 Powder Metallurgy World Congress & Exhibition,* vol. CD-Document number 615, 1998.

[129] G Schlieper, "Principles of gamma ray densitometry," *Metal Powder Report,* vol. 55, pp. 20-23, 2000.

[130] ASTM International, "Standard Specification for Powder Metallurgy (PM) Titanium and Titanium Alloy Structural Components," in *ASTM B988 - 13*, ed. West Conshohocken, PA, 2013.

[131] C. Huang and J. Cheng, "An investigation into the forming limits of sintered porous materials under different operational conditions," *Journal of Materials Processing Technology,* vol. 148, pp. 382-393, 5/30/ 2004.

[132] X. Q. Zhang, Y. H. Peng, X. Y. Ruan, M. Q.Li, and S. C. Wu., "Study of workability limits of porous materials under different upsetting conditions by compressible rigid plastic finite element method," *Journal of Materials Engineering and Performance,* vol. 9, pp. 164-169, 2000/04/01 2000.